学位論文

A non-invasive and matrix effect-free analysis of chemical compositions: an empirical investigation of dolomite grains on an asteroid Ryugu sample

（非侵襲的かつマトリクス効果フリーな定量法の開発：
リュウグウドロマイトのカチオン組成決定への応用）

2024 年 3 月

森田　麻由 / Mayu MORITA

Abstract

Elemental analysis with imaging functionality is crucial for studies of a variety of natural and artificial samples. In particular, for pristine and rare analytes at a micrometer scale on the surfaces, a non-invasive and quantitative manner without sample pre-treatments is favorable. Furthermore, their chemical or physical heterogeneity may induce undesired effects from the sample matrix on a spectral analysis called "matrix effects." X-ray fluorescence analysis (XRF) is one of the classical techniques which suffer from these challenges. To overcome the challenges, the present thesis proposes a new method sequentially combining micro-energy-dispersive X-ray fluorescence (micro-XRF) and Raman micro-spectroscopy. It forms on unique sample cells developed for quantitative analysis of exceptionally rare samples. To investigate an asteroid Ryugu sample, the author constructed analytical technologies step-by-step. First, the author confirmed that the sensitivity to light elements of micro-XRF was significantly improved, and that light element micro-XRF (LE-M-XRF) allowed us to quantify carbon and heavier elements. Second, the proposed sample cell achieved milligram-scaled quantitative analysis in micro-XRF, providing significant accuracy. Third, a non-invasive and matrix effect-free analysis of cation compositions of carbonates was developed. The shifts of Raman wavenumbers for lattice modes discriminately reflected cation substitutions. Furthermore, the degree of freedom in XRF quantitative analysis and Raman analysis led to the construction of a map, which was one-to-one correspondence. This conversion matrix provided Raman micro-spectroscopy with a quantitative nature without any matrix effects. Samples from the asteroid Ryugu were predicted to consist of organic matter and water (hydrated minerals). The author's mission in Hayabusa2 project was to clarify elemental compositions and minerals contained in Chapter 5. The LE-M-XRF in Chapter 2 contributed to determining that the carbon content was approximately 4.8 wt.% by cross-checking the data by WDXRF. Special sample cells were developed for Ryugu samples based on the original designs in Chapter 3. The conversion matrix was further improved from the one in Chapter 4 and a non-invasive Fe+Mn scale for dolomite grains was established. The cation compositions of Ryugu dolomites were determined, and it turned out that the Fe+Mn abundance was 10-15% on average. This trend agreed with precedented studies about other chondrites and Ryugu samples. Finally, the thesis demonstrates that the proposed approach will be a powerful tool to reveal chemical compositions of rare and micrometer-scaled analytes heterogeneously distributed in a non-invasive manner.

Contents

Chapter 1 Introduction

1.1 Introduction

1.1.1 What is X-ray fluorescence analysis (XRF)?

Elemental analysis is fundamental in the realm of analytical chemistry. X-ray fluorescence (XRF) analysis is well-known among many elemental analysis techniques. When incident X-rays irradiate and interact with a substance of the sample, refractive X-rays, scattered X-rays (Rayleigh or Compton), or photoelectrons occur (Figure 1.1(a)). One or more electrons are expelled from the inner orbitals of the atom. This ejection of an electron makes the atom unstable, and the electrons from the outer orbitals of the atom fall into the empty hole in the inner one. Through this process, the energy gap between the two orbitals involved turns into an electromagnetic wave called fluorescent X-ray, characteristic of the atom (Figure 1.1(b)). Measuring their photons provides comprising elements (qualitative) and their composition (quantitative) of the sample in a non-destructive way (Nakai, 2016).

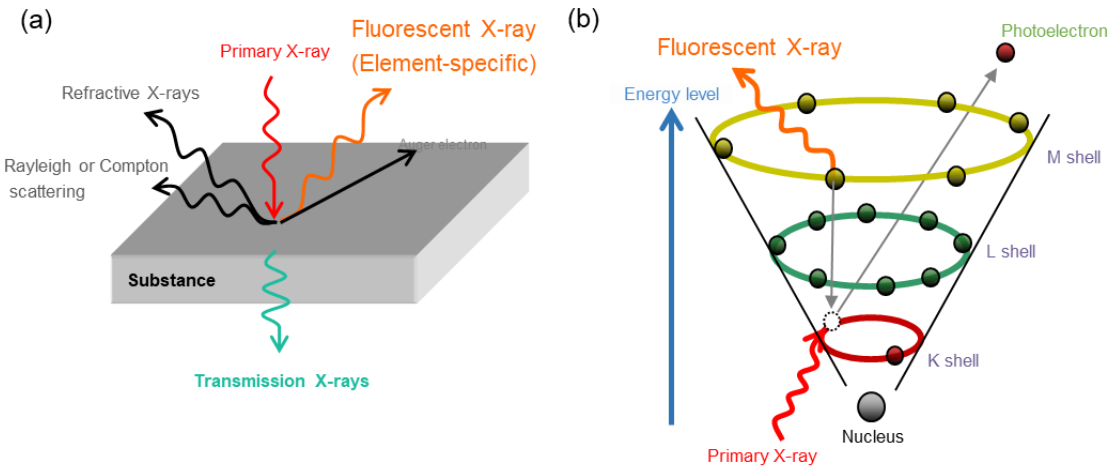

Figure 1.1 Schematic diagrams of the working principle of X-ray fluorescence (XRF) analysis. (a) Interactions of X-ray with a substance. (b) Structure of an atom.

1.1.2 Advances and the history in XRF

A German mechanical engineer, Wilhelm Conrad Röntgen (1985), discovered and named a new ray, which had many properties, as "*X-ray*" for something unknown. The radiograph of his wife's left hand later became a starting point for medical diagnosis. Soon after the discovery, in 1913, experiments by Friedrich et al. (1913) revealed that X-rays were diffracted by crystals and identified as electromagnetic waves. These remarkable findings drove the utilization of X-ray for material science and others as a comparable or overwhelming tool to Scanning Electron Microscope (SEM) due to its penetrating power. Over the century, improvements in three core components, detectors, light sources and optics, have been made to develop X-ray laboratory instruments. For example, several kinds of semiconductor detectors, such as Si (Li) or silicon drift detectors (SDD), reached a high count rate, high transmission of X-rays on a broader region, and superior energy resolution (Homma, 2016). For those who do not have easier access to synchrotron radiation facilities with higher-energy light sources, downsized and power-saving X-ray generating tubes were advanced (Homma, 2016). Because the refraction index of an X-ray is exceptionally close to one and the reflectivity of normal incident light is also highly close to zero, focusing X-rays is not as easy as focusing visible light with optical lenses or mirrors. Thanks to recent advances in optics, the spatial resolution of XRF instruments is reaching tens of microns even with laboratory instrumentation (Ohzawa, 2008; Tsuji et al., 2015). Along with the core components, other improvements, such as fast pulse processing and excellent peak deconvolution, have also been facilitated. Under these circumstances, one of the laboratory-based XRF instruments that offers micro X-ray beams called micro-XRF was developed (Ohzawa & Komatani, 2005; Komatani, 2016).

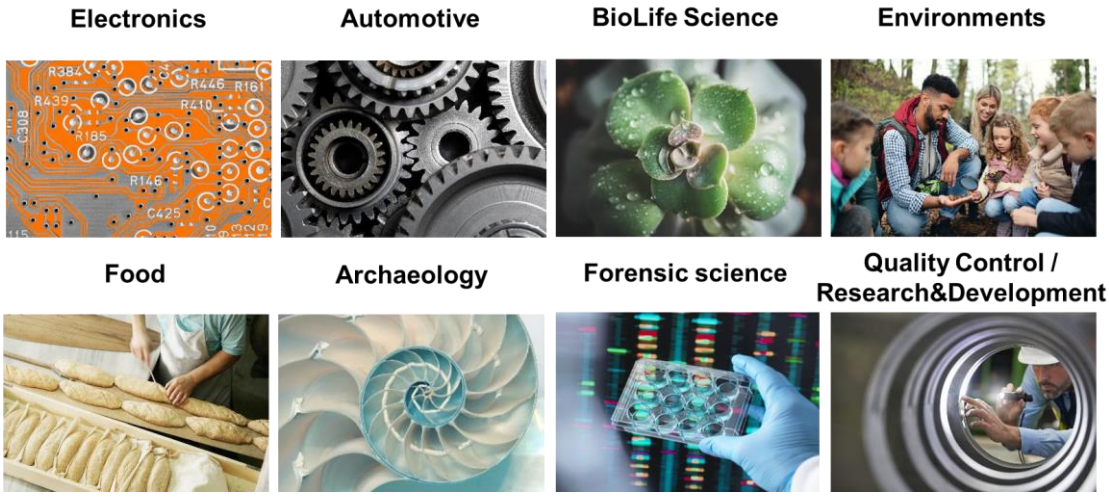

Figure 1.2 Examples of various fields and purposes of XRF applications.

1.1.3 Facing challenges

Thus, the non-destructive, penetrative, and quantitative properties of XRF help us find the locations of analytes – in some cases, even invisible (*i.e.,* buried) – and characterize the samples. Micro-XRF has been widely used in various of fields and purposes (Figure 1.2). In recent years, materials in industrial products have been multi-functionalized. Also, weight saving and miniaturization of electronics and electrical components have advanced. These worldwide trends have accelerated public needs for elemental analysis and structural analysis in the microscopic range.

However, we face the following two challenges in XRF to meet the needs.

1. XRF requires a large quantity of sample. Sample pre-treatments that deliver irreversible alterations through chemical or physical reactions are unfavorable to exceptionally rare samples, because they destroy or damage the sample. In addition, they may lose primitive information which the sample used to have. They frequently give birth to the risks of cross-contamination and sample loss.
2. Effects from the sample matrix are almost inevitable. In this thesis, the term *sample matrix* means a major component of a sample. Characteristics of the sample, such as

surface roughness and heterogeneity of the composition, negatively influence spectral patterns or cause difficulty discriminating signals of an analyte from the sample matrix. Consequently, these reduce the accuracy of quantitative analysis. Hereinafter, these negative effects concerning the sample matrix are called “matrix effects.”

In this thesis paper, the author aims to develop a novel analytical method, overcoming the two challenges. A light element micro-XRF and a unique sample cell for rare samples have made us overcome the first challenge merely through XRF. To solve the second challenge, we have developed a matrix effect-free quantitative method that complements disadvantages of micro-XRF and Raman micro-spectroscopy through sequential combination of techniques. Furthermore, the author aims to practice and evaluate the capability of the developed techniques with different samples.

1.2 Outline

The thesis comprises six chapters. The rest of this thesis is organized as follows. Chapter 2 reviews that we examined the capabilities of a new micro-XRF with a graphite detector window using several samples which had light elements, such as carbon, oxygen, and fluorine. Chapter 3 introduces the development of quantitative analysis with micro-XRF for extremely rare samples, concretely samples weighing 1 mg. Chapter 4 illustrates conversion matrices to roughly quantify major cations of terrestrial carbonates in a matrix effect-free manner. Chapter 5 briefly reviews the improvements of the proposed methods introduced in earlier chapters to study the samples from Asteroid Ryugu. After that, we discuss the results obtained and the value of the proposed approaches by comparing those of conventional methods from an analytical point of view.

1.3 Bibliography

Friedrich, W., Knipping, P., & Laue, M. (1913). Interferenzerscheinungen beiröntgenstrahlen. *Annalen der Physik*, 346(10), 971–988.

Nakai, I. (2016). 蛍光X線分析の基礎 [Basics of X-ray fluorescence analysis]. In I. Nakai (Ed), *蛍光X線分析の実際* [Principles and practices of X-ray fluorescence analysis] (pp. 2-18). Asakura Publishing Co., Ltd.

Homma, H. (2016). 蛍光X線分析装置 [X-ray fluorescence instruments]. In I. Nakai (Ed), *蛍光X線分析の実際* [Principles and practices of X-ray fluorescence analysis] (pp. 32-56). Asakura Publishing Co., Ltd.

Komatani, S. (2016). X線顕微鏡 [X-ray microscopes]. In I. Nakai (Ed), *蛍光X線分析の実際* [Principles and practices of X-ray fluorescence analysis] (pp. 142-151). Asakura Publishing Co., Ltd.

Ohzawa, S. (2008). Development of X-ray Guide Tube. *HORIBA Readout English Edition*, 12, 78–83.

Ohzawa, S. & Komatani, S. (2005). Development of the XGT-5000 X-ray Analytical microscope. *HORIBA Readout English Edition*, 9, 80–83.

Röntgen, W. C. (1895). Uber eine neue art von strahlen. *Sitzung Physikal Medicin Gesellschaft*, 29, 132–141.

Tsuji, K., Matsuno, T., Takimoto, Y., Yamanashi, M., Kometani, N., Sasaki, Y. C., Hasegawa, T., Kato, S., Yamada, T., Shoji, T., & Kawahara, N. (2015). New developments of x-ray fluorescence imaging techniques in laboratory. *Spectrochimica Acta Part B: Atomic Spectroscopy*, 113, 43–53. https://doi.org/10.1016/j.sab.2015.09.001

Chapter 2 Light element micro-XRF

2.1 Introduction

Over the decades, public concerns and awareness about global warming and sustainability have increased. Under the circumstances, top makers of industrial materials worldwide have been developing carbon neutral materials to achieve net-zero carbon dioxide emissions, or reinforced plastics such as carbon/boron fiber reinforced plastics to provide excellent robustness and strength against weight. Today, these materials are popular in aerospace, engineering, automotive motorsports, and others. Hence, a qualitative and quantitative analysis of such compounds or materials containing light elements is strongly preferential.

However, it is challenging to implement such an analysis, particularly without any pre-treatments. Table 2.1 presents several methods frequently used in elemental analysis that allow detection of light elements, including carbon, oxygen, and fluorine. Among these techniques, the highest sensitive is inductively coupled plasma mass spectrometry (ICP-MS) (Thomas, 2013). Under the atmosphere filled with Ar plasma, ICP-MS can measure sprayed liquid samples and it can detect ionized elements by a mass spectrometer. Elements measurable range from Li, and it can provide quantitative analysis with the lower limits of quantification at around several ppm or even ppb levels (Thomas, 2013). A crucial drawback is that it cannot detect volatile elements, such as carbon, nitrogen, and oxygen, and also halogens, like fluorine or chlorine. During destructive pre-treatments, these elements are eliminated from the sample (Thomas, 2013). WDXRF (wavelength dispersive XRF) and Scanning Electron Microscope Energy Dispersive Spectrometer (SEM-EDX) are also well-known alternatives. In WDXRF, primary X-rays collimated irradiate the sample. Then, the element-specific fluorescent X-rays (secondary X-rays)

emanating from the sample are diffracted by analyzing crystals and collected by a detector (usually a scintillation counter or a proportional counter) (Homma, 2016). SEM-EDX has an electron beam as the excitation source, and signals called characteristic X-rays emitted from the sample are detected by a silicon drift detector (SDD) (Takahashi, 2016). Basically, as an element of interest is lighter, the fluorescence yield of that element is worse due to an increasing production of Auger electron. In addition, the photons produced significantly decline. Therefore, in WDXRF, intensified primary X-rays can compensate for the worse yields. In SEM-EDX, the chamber atmosphere under ultra-high vacuumed conditions prevents the photons from attenuating. Although these techniques can accurately measure elements from beryllium (Be) or even heavier, damaging sample pre-treatments or measurement conditions, *e.g.,* intensive excitation (X-ray/electron) beams, fused glass beads, resin-embedding, or metal/carbon coating, often limit their measurable ranges of element to sodium (Na) or even greater atomic mass elements. Hence, a quantitative method for light elements, specifically carbon, without any sample pre-treatments is underdeveloped.

Table 2.1 Comparison of analytical methods for light element analyses.

	EDXRF (micro-XRF)	WDXRF	SEM-EDX	ICP-MS
Excitation	X-ray	X-ray	Electron	Plasma Ar
Lightest element can be measured	$_{11}$Na	$_{4}$Be	$_{4}$Be	$_{6}$Li
Necessity of pre-treatments	✓	✓✓✓	✓✓✓	✓✓✓
Quantitative range	ppm~wt.%	ppm	Ppm	ppm~ppb

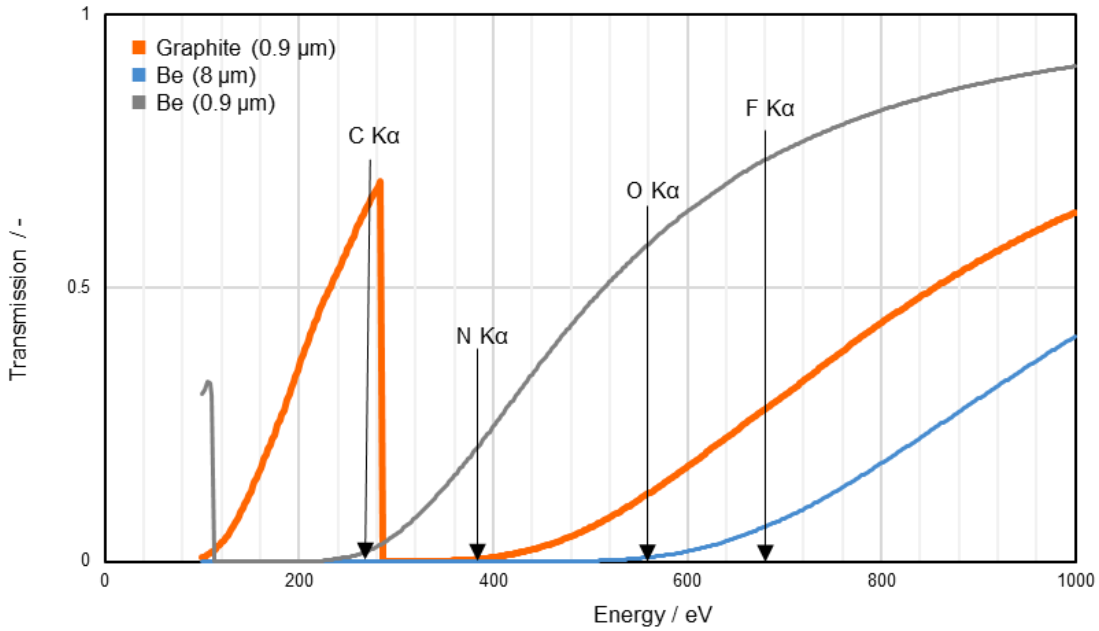

Figure 2.1 Theoretical calculation of X-ray transmission in the soft-X-ray range (Henke et al., 1993).

Compared with these technologies, EDXRF is promising but unfavorable, because it provides a qualitative and quantitative analysis from sodium (Na) at best. This limitation is because a detector window absorbs soft X-ray photons. Figure 2.1 shows transmission rates of soft X-rays when various window materials are used based on the theoretical calculation of Henke et al. (1993). Here, X-rays under 1 keV do not transmit through the 8 µm thick Be window (a usual window material for EDXRF), and the intensity of F Kα declines to approximately five percent. In contrast, the 900 nm thick graphite window can detect C Kα, O Kα, and F Kα except N Kα. This exception is because the absorption edge of C is proximate to the energy of N Kα, and accordingly, N Kα dramatically attenuates. Note that in the 900 nm thick Be window, the transmissions of N Kα, O Kα, and F Kα are higher than those in the graphite window since Be is lighter than C (graphite). Still, the 0.9 mm thick Be window has yet to be applied to the window, concerning its mechanical weakness for vacuuming instrument chambers.

Indeed, it is not easy to apply these window materials to EDXRF due to the following three requirements: high transmission of soft X-rays, robustness to seal the detector unit airtight, and the blocking capability of visible light. Specifically, the detector window must shut off visible light to prevent unwanted signals from deteriorating the signal-to-noise ratio when obtaining an optical image of the sample. In this regard, although several materials, such as polymers (Huebner et al., 2015; Roberts & Anderson, 2004; Scholze & Procop, 2005), diamonds (Ying & Xu, 2000; Reinhard et al., 2004), and silicon nitride (Törmä et al., 2013) have been used for SEM-EDX, they have not been employed for micro-XRF because these materials are mostly transparent.

In recent years, the graphite detector window has been introduced to EDXRF. A thin graphite film deposited on the silicon substrate can achieve superior gas and light tightness and it also can present mechanical strength (Huebner et al., 2015). Lately, a novel Silicon Drift Detector named AXAS-A System (KETEK GmbH) has a 900 nm thickness detector window made of graphite. Installation of this detector to our new light element micro-XRF (LE-M-XRF) enables to measure elements from carbon to heavier, according to the catalog.

In this chapter, we aim to develop a quantitative analysis of light element samples without any sample pre-treatments. Of various analytical methods, we focused on the LE-M-XRF with an energy dispersive spectrometer, and we verified its performance. First, the improvements in sensitivity to carbon and fluorine consisting of a standard sample were evaluated in comparison of measured intensities with the theoretical ones. Second, we performed imaging analyses to study the distributions of light elements, using different samples without pre-treatments.

2.2 Experiments

2.2.1 Instrument

Micro-XRF experiments were performed with a HORIBA XGT-9000 X-ray Analytical Microscope (Ohzawa & Komatani, 2005). Figure 2.2 is a schematic figure that illustrates the optical configuration. Primary X-rays were generated by the Rh target and focused by a glass poly-capillary (Kumakhov, 2000; Thiel et al., 1993) called X-ray Guide Tube (Ohzawa, 2008) into approximately 100 μm in diameter. The focal point is at the working distance of 1 mm. XGT-9000 vertically irradiated samples on the specimen stage with the primary X-ray beam from above. Fluorescent X-rays emitted from the samples were collected by the SDD (AXAS-A System, KETEK GmbH) placed from 45° above. Hereinafter, this thesis describes this detector as "C window detector" and, in contrast, the detector with an 8 μm thick Be window as "Be window detector". The full width at half maximum (FWHM) of C window detector at Mn Kα (5.89 keV) was approximately 128 eV. The difference in sensitivity to light elements between these two detectors is described in the following section. The element images were displayed in gradation based on specimen stage X-Y coordinates and the X-ray intensity of each element of interest with the original software HORIBA X-RAY LAB For XGT-9000 SERIES (ver. 1.5.0.23.).

2.2.2 Samples

The optical images of samples obtained by the CCD camera above the specimen stage will be summarized in Appendix A. For the evaluation of the improved sensitivity, a piece of polytetrafluoroethylene (PTFE) tube was prepared (Figure A.1). An example of failure analysis prepared was a stainless 6-way switch valve as part of sulfur (S) analyzing unit of an instrument (Figure A.2). Another example is a sheet of the separator of an automotive battery contacting the positive electrode (Figure A.3).

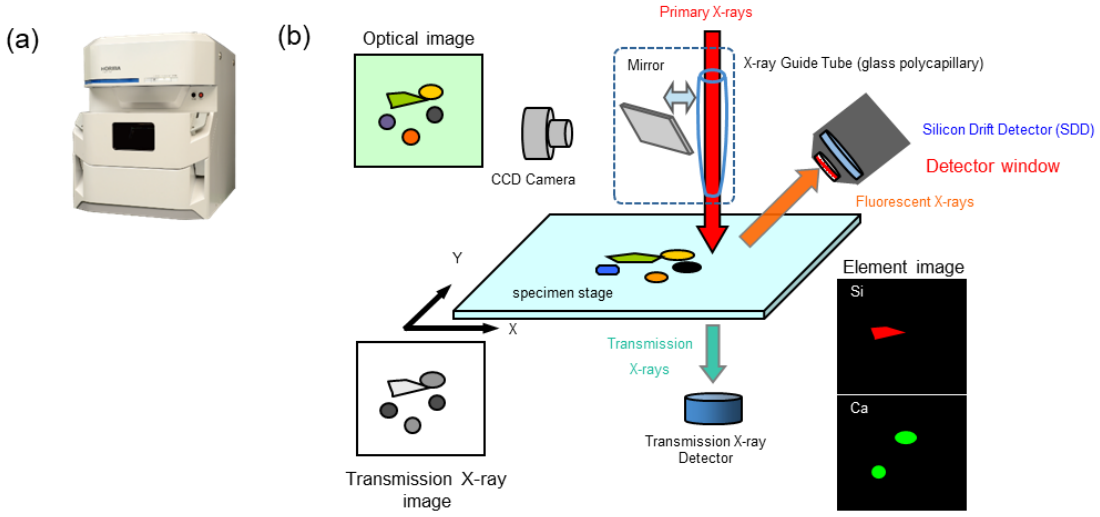

Figure 2.2 Exterior photograph (a) and schematic illustration of the optical configuration (b) of Analytical Microscope XGT-9000. Instrumental settings were the following: 15 kV (X-ray tube voltage), 1000 μA (X-ray tube current), 1 mm (X-ray working distance) and 1.25 μs (peaking time). For the elemental imaging, XGT software automatically defined the step size depending on the number of pixels and the size of imaging area. The X-ray guide tube was a glass poly-capillary optic with 100 μm at the focal point.

2.2.3 Measurement conditions and instrumental settings

We optimized the following instrumental settings to enhance the sensitivity to light elements: the X-ray tube voltage, the peaking time, and the chamber atmosphere. We made the X-ray tube voltage 15 kV because radiation with the lowest tube voltage preferentially excites carbon, oxygen and fluorine. We chose the longest peaking time (1.25 μs) to deconvolute a peak of interest from overlapping ones from L lines of heavier elements. During the experiments, we selected "Whole Vacuum" mode, where the atmosphere inside the entire chambers was kept being vacuumed under tens of Pa to mitigate the attenuation of photons. As for the PTFE tube, one spot shown in the black arrowhead was probed (Figure A.1). Maximized X-ray tube current and the measurement time (1000 μA and 1000 s, respectively) enhanced the count rate and signal-to-noise ratio.

The area squared 16.4 mm on the corroded surface of the valve was scanned. The X-ray tube voltage, the peaking time and the chamber atmosphere were all identical to the settings for the PTFE tube. The tube current, the step size, and the measurement time were 550 μA, 64 μm and 1000 s, respectively.

The measurement area 2.56 mm wide and 0.75 mm high in the separator sheet was analyzed. The X-ray tube voltage, the peaking time, and the chamber atmosphere were all identical to the settings for the PTFE tube. The tube current, the step size, and measurement were 1000 μA, 10 μm, and 24000 s, respectively. This setting indicates a remarkably smaller step size than the beam size, in short, oversampling. It should be noted that an advantage of the oversampling is that it realizes a higher count rate than the condition where the step size is equivalent to the beam size.

2.3 Results and discussions

2.3.1 Evaluation of the improved sensitivity to lighter elements

First and foremost, we evaluated the improvement of sensitivity to light elements of the C window detector using a standard sample, the PTFE tube. The spectra of fluorescent X-rays are shown in Figure 2.3. A peak around 0.67 keV of fluorine (F) Kα in the C window detector spectrum is prominent, while that in the Be window detector is slightly noticeable. The X-ray intensities of F Kα from the C window detector were 13 times higher than those from the Be window detector. According to Figure 2.1, the improvement theoretically calculated is approximately 4.5 times. This over-achievement is unclear, but one possible reason is that the F Kα peak in the Be window detector remarkably smaller than expected due to a higher dead time for higher energy photons, and therefore the Be window detector did not F Kα and other lower-energy photons. Also, a peak around 0.27 keV of carbon Kα is present in the C window detector alone. Thus, we found that the

sensitivity to the two elements was significantly improved. Hereinafter, the spectra were obtained only by the C window detector.

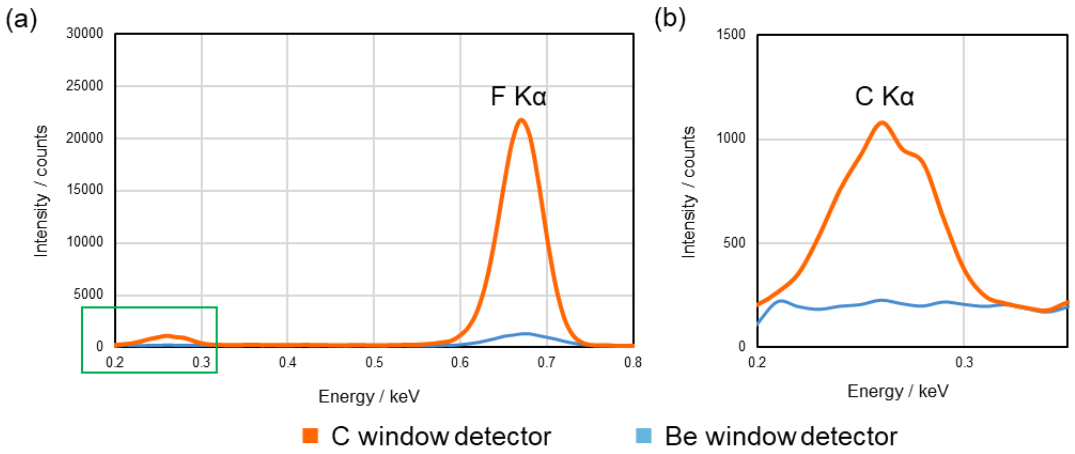

Figure 2.3 Magnified XRF spectra for the PTFE tube in (a) near F Kα region and (b) near C Kα region obtained by the two detectors. The green box in the figure (a) corresponds to the figure (b).

2.3.2 Lower limit of detection (LLD) of carbon

We calculated the lower limit of detection (LLD) of C from the following formula (Nishino, 2016).

$$LLD = 3 \cdot \frac{W}{I_{net}} \cdot \sqrt{\frac{I_{BG}}{t}} \qquad (2.1)$$

W: elemental abundance [wt.%], t: measurement time [s],

I_{net}: Net intensity [cps], I_{BG}: background intensity [cps]

In Eq.(2.1), C and F contents were theoretically determined based on the proposition that the chemical formula of the PTFE tube is C_2F_4. Since conventional EDXRF can measure Na at a percent level, the resulting LLD 1.5 wt.% certainly showed an improvement. Also, the LLD is comparable to the previous study (Shibata, 2016) reporting that the LLD of C was approximately 2.5 wt.% from the analysis of cement ($CaCO_3$).

2.3.3 Elemental image of fluorine in the switch valve

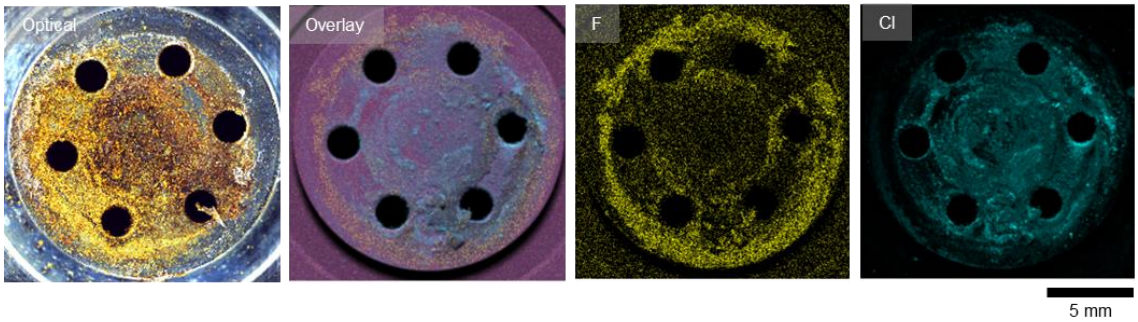

Figure 2.4 Elemental imaging of the 6-way switch valve. In the overlay image, yellow, cyan, and magenta are F, Cl, and Fe, respectively.

Generally speaking, in failure analysis, non-destructive methods without sample pre-treatments are valuable because failed specimens are unaffected by such analyses. Corrosive elements in the gas switching valve are heterogeneously deposited, found around six sample cells (Figure 2.4). However, WDXRF's large collimated primary beams cannot specify a contributing element to the corrosion in such a heterogeneous sample, and a SEM-EDX chamber cannot enclose the sample as-is due to its sample size. Therefore, we utilized LE-M-XRF in this study. Figure A.4 is a summed XRF spectra for the imaging area in a logarithmic scale. The figure shows that the following nine elements are detected: F, Si, S, Cl, Cr, Fe, Ni, Cu, and Mo (Lα). Because Si, Cr, Fe, Ni, Cu, and Mo are primary components of stainless, they are predictably derived from the substrate. Note that S is also present but ruled out because it is the main component of the sample gas. Having detected F and Cl by micro-XRF made us suspect that the two elements were candidates for the corrosive substance. In Figure 2.4, element images display higher X-ray intensity of an element in stronger brightness. Interestingly, elemental imaging revealed that the two elements were not uniformly distributed. Specifically, F existed on an outer edge, while Cl existed in the center of the measurement area. Here, the region of interest for Cl X-ray intensity is 2.52 ~ 2.63 keV to avoid the peak overlap of L lines from

the Rh target.

However, one critical drawback of elemental imaging is that the measurement time per pixel needs longer to assign peaks to elements because of poor S/N ratio and inferior energy resolution. In this regard, we further examined two spectra of areas depicted as Area-1 and Area-2 in Figure 2.5(a) to confirm the presence of the elements. As Figure 2.5(b) shows, a remarkable peak in the Area-1 spectrum can be assigned to F Kα (0.67 keV) because Fe L lines (0.71 keV) derived from the substrate in the Area-2 spectrum are not present. On the other hand, a prominent Cl Kα peak is present, although the Cl Kα peak overlaps the L lines of the Rh target (Figure 2.5(c)). Eventually, the existence and distribution of two elements are proven by spectral analysis and element images, and this result helped us find a new route in which the corrosive substance consisting of F entered.

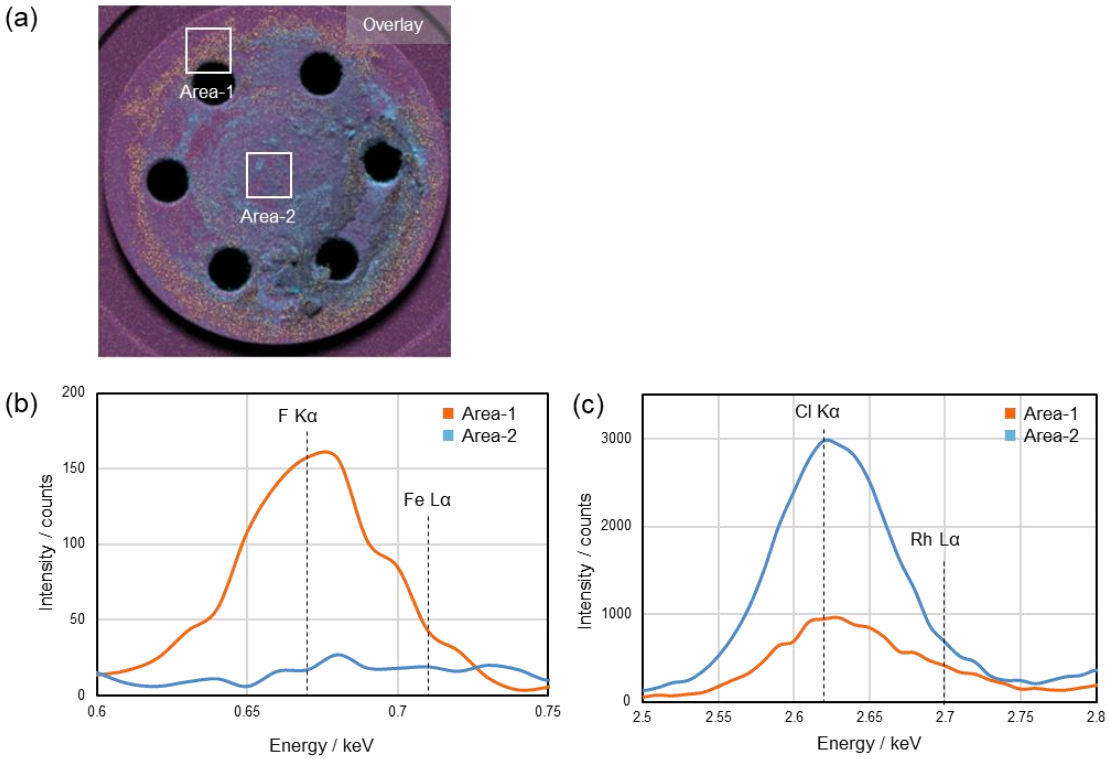

Figure 2.5 XRF spectra of Area-1 and Area-2 for the confirmation of the presence of F and Cl. The overlay image (a) and the XRF spectrum of Area-1 (b) near F Kα region and the XRF spectrum of Area-2 (c) near Cl Kα region.

2.3.4 Elemental imaging for Automotive separator

Detection of foreign matter on a sheet of separator or evaluation of heterogeneity of battery materials applied is a growing demand in industry, but formidable. For example, WDXRF will damage the separator sheet due to intensive primary. X-rays, or SEM-EDX will cause charge-up onto the surface. On the other hand, LE-M-XRF easily detected C, O, F, Al, Co, and Ni and clarified their distributions (Figure 2.6). The upper half of the measured area was polyamide-imide (PAI), and the rest was ceramics. As expected, C derived from PAI was found, and O and Al derived from ceramics were also detected. In addition, F derived from binders for the active material was detected. In the black-colored part of the optical image, O, Co, and Ni are present, whereas Al is not. Therefore, there is not foreign matter but a fragment of active materials for the positive electrode.

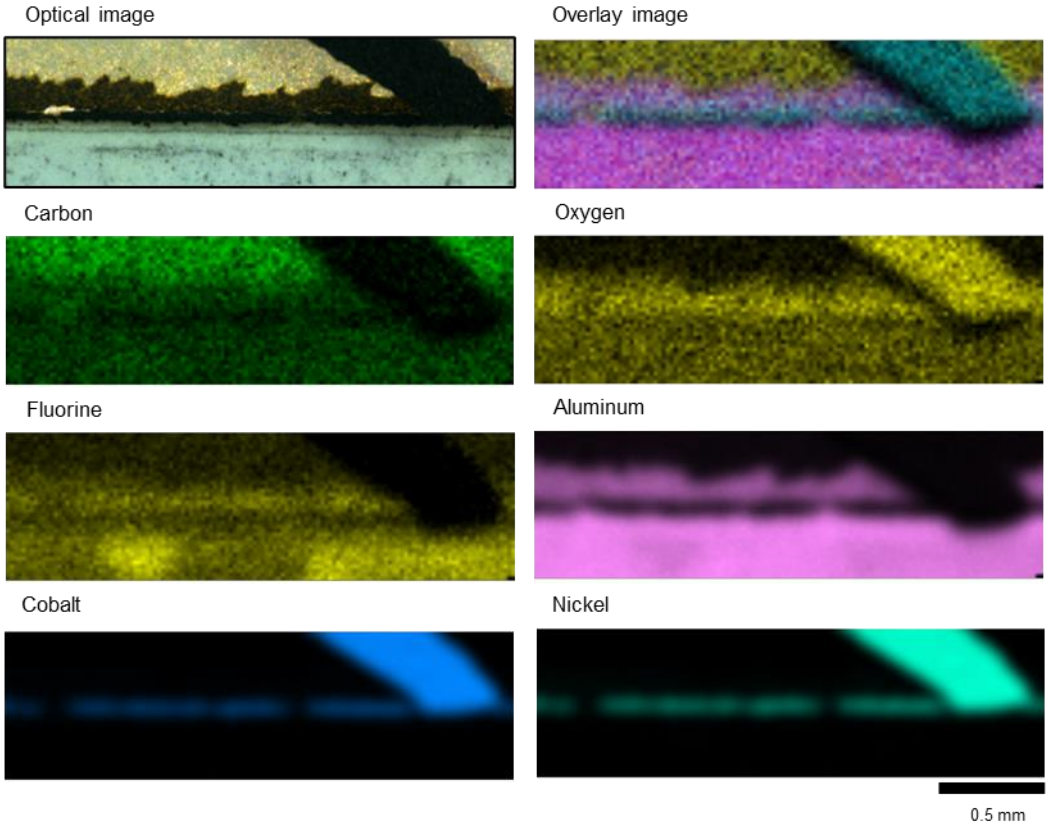

Figure 2.6 Elemental imaging of the separator sheet. Yellow, cyan, and magenta in the overlay image are carbon, oxygen, and aluminum.

2.3.5 Advantages of LE-M-XRF

In summary, the proposed LE-M-XRF achieved to provide qualitative and imaging analysis of light elements without sample pre-treatments. The lower limit of detection of carbon makes us conclude that it will be applicable to analyses not only of carbon matter but also of heterogeneous samples with trace light elements. Examples are fragments of reinforced plastics or resin coatings on surfaces of a product, and microplastics (MPs) washed up on sand beaches. In the future, it will be a supportive, complementary tool for Raman spectroscopy, FT-IR and others.

2.4 Conclusion

We reviewed higher transmission for a softer range of X-rays was achieved thanks to the C window detector. Prominent F Kα and C Kα peaks were observed in the C window detector spectrum when analyzing the surface of the PTFE tube. In addition, the resulting lower limit of detection for carbon was 1.5 wt.% in the present study, which was almost equivalent to the one in the previous study. We examined two examples of samples with this new detector. The detection of fluorine and the spatial distributions of carbon and oxygen in the samples helped us identify the cause of the corrosion and the structure of the composite materials without any pre-treatments.

2.5 Bibliography

Henke, B., Gullikson, E., & Davis, J. (1993). X-ray interactions: Photoabsorption, scattering, transmission, and reflection at e = 50-30,000 ev, z =1-92. *Atomic Data and Nuclear Data Tables*, 54(2), 181–342.

Huebner, S., Miyakawa, N., Kapser, S., Pahlke, A., & Kreupl, F. (2015). High

performance x-ray transmission windows based on graphenic carbon. *IEEE Transactions on Nuclear Science*, 62(2), 588–593.

Homma, H. (2016). 蛍光 X 線分析装置 [X-ray fluorescence instruments]. In I. Nakai (Ed), *蛍光 X 線分析の実際* [Principles and practices of X-ray fluorescence analysis] (pp. 32-56). Asakura Publishing Co., Ltd.

Kumakhov, M. A. (2000). Capillary optics and their use in x-ray analysis. *X-Ray Spectrometry*, 29(5), 343–348.

Morita, M., Aoyama, T., Nakano, H., & Komatani, S. (2022). Practical Application of Elemental Imaging for Light Elements, Including Oxygen and Fluorine in Industrial Materials by Micro-EDXRF. *Advances in X-ray Chemical Analysis, Japan.*, 53, 139–149.

Nishino, M. (2016). 分析結果を論文・報告書に書く時の注意事項 [Remarks when you describe the results of analysis on a paper or report]. In I. Nakai (Ed), *蛍光X線分析の実際* [Principles and practices of X-ray fluorescence analysis] (pp. 238-243). Asakura Publishing Co., Ltd.

Ohzawa, S. (2008). Development of X-ray Guide Tube. *HORIBA Readout English Edition*, 12, 78–83.

Ohzawa, S. & Komatani, S. (2005). Development of the XGT-5000 X-ray Analytical Microscope. *HORIBA Readout English Edition*, 9, 80–83.

Reinhard, D. K., Grotjohn, T. A., Becker, M., Yaran, M. K., Schuelke, T., & Asmussen, J. (2004). Fabrication and properties of ultranano, nano, and microcrystalline diamond membranes and sheets. *Journal of Vacuum Science & Technology B: Microelectronics and Nanometer Structures Processing, Measurement, and Phenomena*, 22(6), 2811–2817.

Roberts, M. C. & Anderson, E. C. (2004). Light rejection evaluation of ultrathin polymer

eds windows. Microscopy and Microanalysis, 10(S02), 924–925.

Scholze, F. & Procop, M. (2005). Detection efficiency of energy-dispersive detectors with low-energy windows. *X-Ray Spectrometry*, 34(6), 473–476.

Scholze, F. & Procop, M. (2005). Detection efficiency of energy-dispersive detectors with low-energy windows. *X-Ray Spectrometry*, 34(6), 473–476.

Shibata, Y. (2016). 卓上型 EDX 装置による炭素～フッ素分析 [Light-element analyses ranging from carbon to fluorine by a benchtop EDXRF instrument]. In I. Nakai (Ed), *蛍光 X 線分析の実際* [Principles and practices of X-ray fluorescence analysis] (pp. 220-221). Asakura Publishing Co., Ltd.

Takahashi, H. (2016). SEM-EDS. In I. Nakai (Ed), *蛍光 X 線分析の実際* [Principles and practices of X-ray fluorescence analysis] (pp. 152-168). Asakura Publishing Co., Ltd.

Thiel, D. J., Bilderback, D. H., & Lewis, A. (1993). Production of intense micrometer-sized x-ray beams with tapered glass monocapillaries. *Review of Scientific Instruments*, 64(10), 2872–2878.

Thomas, R. (2013). *Practical Guide to ICP-MS: A Tutorial for Beginners* (1st ed.). CRC Press, Boca Raton, 3 edition.

Törmä, P. T., Sipilä, H. J., Mattila, M., Kostamo, P., Kostamo, J., Kostamo, E., Lipsanen, H., Nelms, N., Shortt, B., Bavdaz, M., & Laubis, C. (2013). Ultrathin silicon nitride x-ray windows. *IEEE Transactions on Nuclear Science*, 60(2), 1311–1314.

Ying, X. & Xu, X. (2000). CVD diamond thin film for IR optics and X-ray optics. *Thin Solid Films*, 368(2), 297–299.

Chapter 3 Improved accuracy in XRF for rare samples

3.1 Introduction

Samples, including a small piece of artwork, criminal evidence left at crime scenes, and archaeological specimens, only offer limited amounts for chemical analysis. They are unduplicatable and must be free from any risks of damage or loss. Hence, a milligram-scale quantitative analysis in a non-invasive manner is strongly desired.

For analyzing such samples, Scanning Electron Microscope-Energy Dispersive spectroscopy (SEM-EDX) is promising (Table 3.1). This technique can analyze powdery or liquid samples as-is, similar to X-ray fluorescence analysis (XRF), and save required sample amounts to extremely small due to its superior spatial resolution. Improving accuracy requires appropriate sample pre-treatments, such as resin embedding, metal/carbon coating, and surface polishing. (Ito et al., 2019). Hence, this method has been used to provide micrometer-scaled elemental compositions at local positions of the entire sample (Ito et al., 2019; Takahashi, 2016).

Table 3.1 Comparison of analytical methods for milligram-scale analysis.

	EDXRF (micro-XRF)	WDXRF	SEM-EDX
Quantification	✓	✓ ✓	✓ ✓ ✓
pre-treatments	glass bead technique, pellet press method, loose-powder method,		Resin embedding, metal/carbon coating, surface polishing
non-invasive	✓	× ×	× × ×
milligram-scale analysis	× × × (100 mg~)	✓ ✓ (10 mg~)	✓ ✓ ✓

Conversely, XRF provides the average information of a bulk sample with a

heterogeneous composition in a non-destructive manner. In recent years, required sample quantities for XRF quantitative analysis have decreased (Table 3.1). Concretely, wavelength dispersive XRF (WDXRF) can analyze samples weighing tens of mg, according to precedented studies (Ichikawa et al., 2012; Ichikawa & Nakamura, 2014). In these cases, a destructive pre-treatment called the glass bead technique that vitrifies a specimen into a disk (Figure 3.1(a)) is strongly recommended to ensure a homogeneous measurement area necessary for enhanced sensitive and accurate analysis (Ichikawa & Nakamura, 2014; Takahashi, 2015). In this regard, WDXRF analysis is no longer non-invasive. Loose-powder and pellet press methods are simpler used for energy-dispersive XRF (EDXRF) than the glass bead technique (Takahashi, 2015). The pellet press method uses a pressing machine and a metal die set to compress powder into a disk (Figure 3.1(b)). The loose powder method is more non-invasive, which encloses the powder in a cell with a plastic film (Figure 3.1(c)). Here, the term "non-invasive" means no permanent procedures are involved. However, one critical disadvantage of these pre-treatments is that they demand considerable quantities of samples, usually at least hundreds or thousands of mg (Homma, 2016; Ichikawa & Nakamura, 2016).

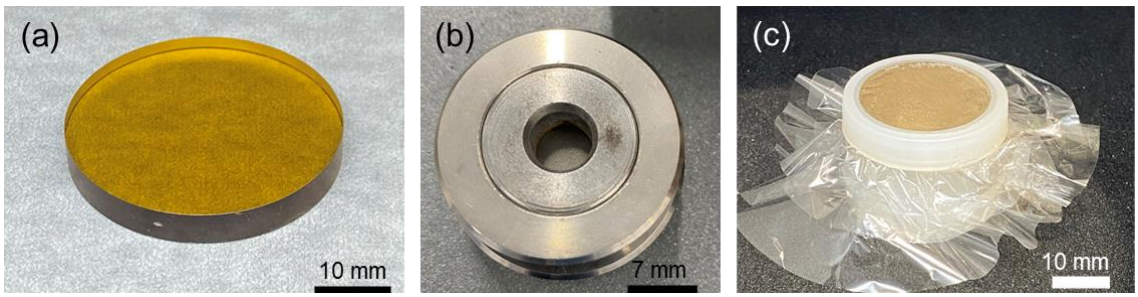

Figure 3.1 Images of sample pre-treatments frequently used in XRF analysis. (a) Glass bead technique, (b) pellet press method, (c) loose-powder method.

The present study aims to establish a quantitative analysis of EDXRF for milligram-scaled samples. To achieve the aim, the author attempted to develop a novel sample cell

for small-volume samples. However, the author faced to Challenge 1. Figure 3.2 illustrates this problem. No sample cell for 1 mg sample has been designed. When the sample volume (1 mg) is fixed, the cell depth and the probe diameter are trade-off under a millimeter scale. For example, maximizing the probe diameter and reducing the cell depth will cause difficulty in analyzing certain elements (Homma, 2016; Ichikawa & Nakamura, 2016), thus consequently reducing quantitative accuracy. Conversely, maximizing the cell depth and reducing the probe diameter will obtain the local composition, not global (bulk) composition of the sample with chemical heterogeneity.

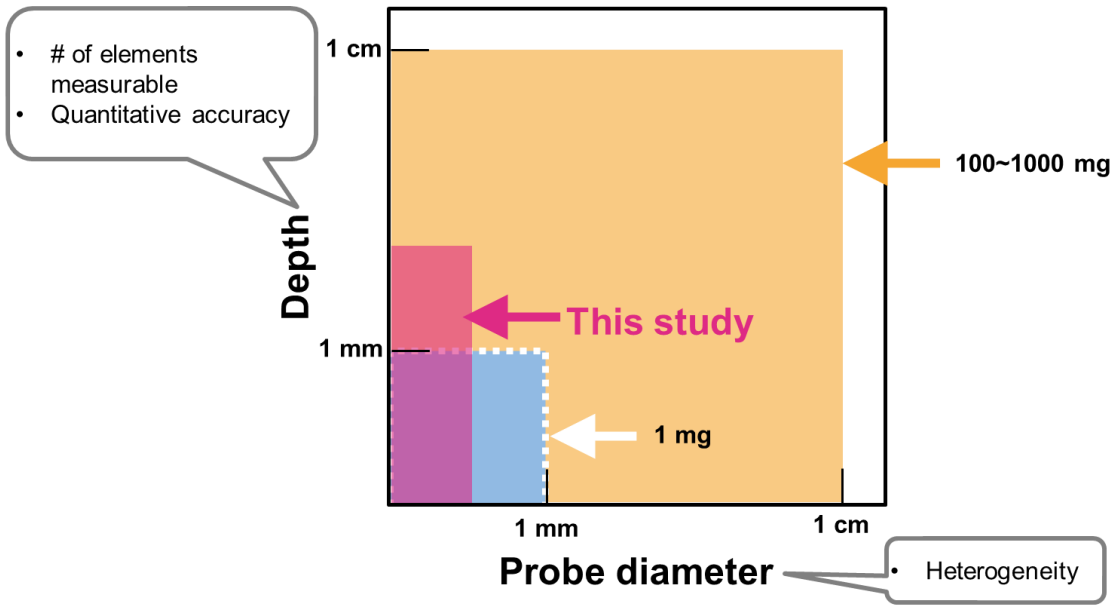

Figure 3.2 Schematic drawing of Challenge #1 for developing the sample cell.

Taking advantage of imaging modality of micro-XRF with an energy-dispersive spectrometer, the author solved this challenge. Specifically, elemental imaging with parallel micro-beams minimized the cell diameter probed and compensated with chemical heterogeneity. Conversely, the cell depth was maximized. Thus, the author made both incompatible factors of the sample cell work. The design in detail will be discussed.

In the present study, “a milligram-scaled quantitative analysis” is defined to quantify geo-standards weighing 1 mg with 0.99 or above correlation coefficients between reference values and quantitative ones. The studied samples consisted of elements ranging from sodium (Na) to lead (Pb), and the lowest concentrations were around 100 ppm. The proposed sample cell helped us measure such light or trace elements and achieve the benchmark efficiently and cost-savingly without any changes in the hardware of the measuring apparatus.

3.2 Experiments

3.2.1 Design of sample cell

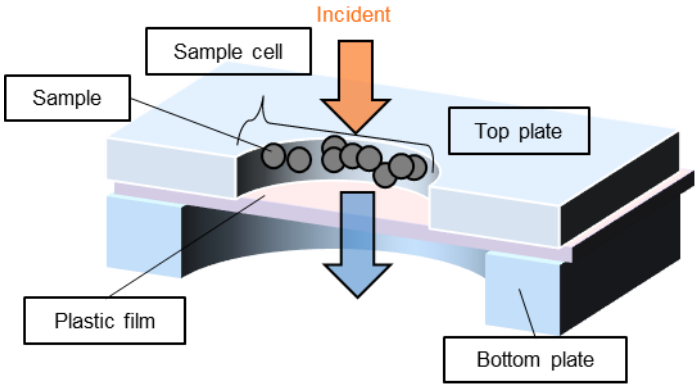

Figure 3.3 Schematic illustration of the sample cell.

The design of the sample cell is shown in Figure 3.3. The sample cell is a hole drilled into an acrylic resin plate whose size depends on individual sample masses, summarized in Table 3.2. For instance, the cell diameter is 1 mm, and the depth is 0.5 mm for 1 mg samples. Notably, no plastic film is applied at the top. A thin PET film backing helps to hold the sample in place. We gently compacted the sample with a plate made of acrylic resin by hand. Note that the hole diameter on the bottom plate is always larger than that of the sample cell. This design reduces unwanted peaks, specifically scattering X-rays,

from the bottom acrylic resin irradiated with the primary X-ray. In other words, the sample cell is container-like with an open top.

Table 3.2 Designs of the sample cell.

sample mass [mg]	cell diameter [mm]	cell depth [mm]
100	4.0	3.0
10	1.5	2.0
1	1.0	0.5

3.2.2 Micro-XRF

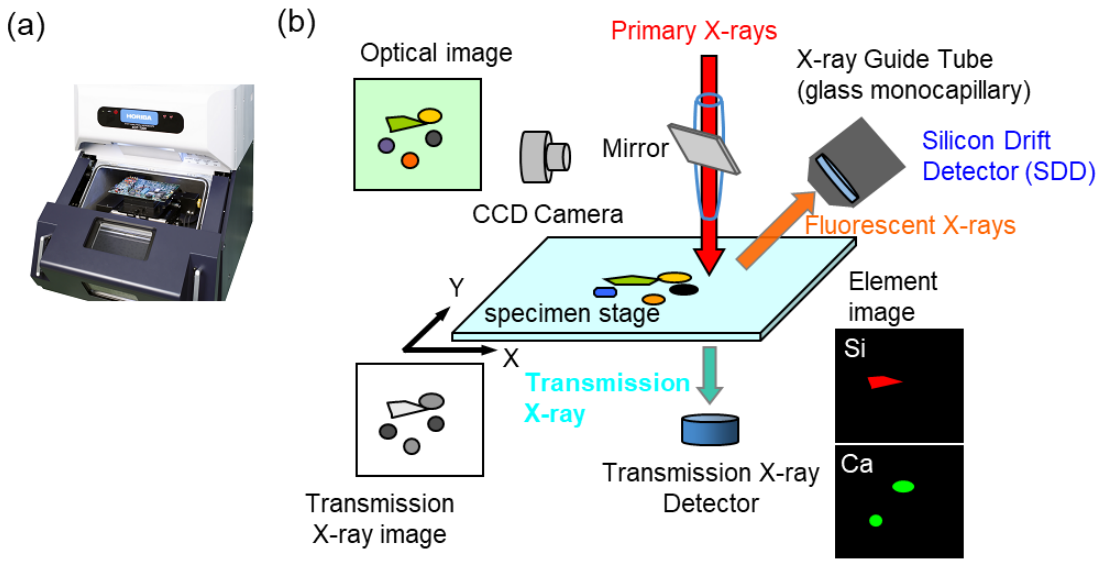

Figure 3.4 Exterior photograph (a) and schematic illustration (b) of the optical configuration of X-ray Analytical Microscope XGT-7200. Instrumental settings were the following: 30 kV (X-ray tube voltage), 1000 μA (X-ray tube current), 1 mm (X-ray working distance) and 1.25 μs (peaking time). For the elemental imaging, the step size was 24 μm. The X-ray guide tube was a glass mono-capillary optic with 100 μm at the focal point.

The micro-XRF measurements were carried out with HORIBA Analytical Microscope XGT-7200 (Figure 3.4). The optical configuration of XGT-7200, nearly equivalent to that of XGT-9000, is described elsewhere (Morita et al., 2022). One remarkable difference is

that XGT-7200 equips a glass X-ray Guide Tube called a mono-capillary optic; the critical feature is vigorous intensity and superior spatial resolution of 100 μm even at deeper working distances (Ohzawa, 2008).

3.2.3 Measurement conditions

The sample surfaces squared 0.5 mm of 1 mg samples surface were probed. The sample surfaces squared approximately 3 mm for the 10 mg or 100 mg samples were also studied for comparison. Elemental imaging can compensate for sample characteristics, specifically, the heterogeneity of composition. The measurement conditions are the following. The X-ray tube voltage, the tube current, the working distance, and peaking time were 30 kV, 1000 μA, 1 mm and 1.25 μs, respectively. The step size was 24 μm. The chamber atmosphere was Whole Vacuum mode (Morita et al., 2022). The standard Fundamental Parameter Method (FPM) was applied to analyze elements in the samples. FPM (Sherman, 1955; Shiraiwa & Fujino, 1966) is a theoretical calculation of element concentration based on the fitting of the measured XRF spectra and theoretical spectra constituted by fundamental parameters (FPs) such as X-ray absorption coefficients, fluorescence yields, and the incident spectrum from the X-ray tube (Nishino, 2016). However, the physic parameters defined and the theoretical spectrum are based on the proposition that the sample is bulk and pure. Therefore, resulting quantitative values can be heavily influenced by so-called matrix effects, such as self-absorption, secondary enhancement, and scattering derived from sample characteristics, including the heterogeneous composition and the density. Here, we calibrated and corrected the calculations with the standard material named JSd-2. All elements were quantified in oxide form, for example, SiO_2, Cr_2O_3, MnO, and Fe_2O_3.

3.2.4 Samples

As earlier described, a standard named JSd-2 was prepared to calibrate the FPs. To evaluate quantitative accuracy, we prepared three more standards named JSd-1, JSd-3, and JSl-1. The JSd series are sediment, and JSl-1 is slate, provided by The National Institute of Advanced Industrial Science and Technology, Japan. All the samples were weighed to 1 mg, 10 mg, and 100 mg, respectively. The complete information is available from the reference (Imai et al., 1996).

3.2.5 Evaluation of quantitative results

For discussions in the next section, we defined Pearson correlation coefficients R^2, indicating a correlation between reference values and quantitative values as follows.

$$R^2 = \frac{Cov_{(W_R, W_Q)}}{S_{(W_R)} \times S_{(W_Q)}} \qquad (3.1)$$

Cov: Covariance, *S*: standard deviation,

W_R: reference values [wt.%], W_Q: quantitative values [wt. %]

Also, we determined two groups: “major element” and “minor element.” The former comprises elements whose reference values in oxide form are one wt.% and more, and the latter is the rest. The correlation coefficients were given for each group in all samples.

3.3 Results and discussions

3.3.1 Spectrum comparison

Figure 3.5 shows magnified spectra of samples weighing 1 mg in lower-energy regions. Prominent peaks of three major components, Al, Si, and Fe are observed in all samples. Generally speaking, X-ray fluorescence yield depends on that element, and heavier elements emit stronger fluorescence. On the other hand, the peak intensity for a specific element is proportional to its concentration and can be compared among the samples

because they all primarily consist of SiO_2 (approximately 65 wt.%). For example, the peak intensity of Fe in the JSd-2 spectrum is the highest, JSl-1 follows, and JSd-1 and JSd-3 are nearly equivalent. In the even lighter region, the peak intensity of Mg in the JSd-2 spectrum equals JSl-1, JSd-1 follows, and JSd-3 is the lowest. Na is present in three samples except JSd-3. This absence may be because the Na content (0.411 wt.% in Na_2O) in the JSd-3 was below the lower limit of detection in this experiment. Thus, peak intensities of individual elements in different samples positively correlate with reference values.

Magnified spectra in heavier regions are presented in Figure 3.6. Similarly, peak intensities of individual elements positively correlate with reference values. Notably, we can observe peaks of minor elements, such as Mn (JSd-3), Cu (JSd-2, JSd-3), Zn (JSd-2, JSd-3, JSl-1), and Rb (JSd-3) in respective sample. Elements with high atomic numbers or high energies of fluorescence, such as Pb and Ba, require thicker analytical depths at several millimeter-scaled (Henke et al., 1993). It should be highlighted that Pb Lα is present in the JSd-3 spectrum, although neither Ba Kα nor Ba Kβ is found. Ba L lines are absent in JSd-3. Further, the intensities of Rh (X-ray tube) scattering are almost equivalent in all samples, reflecting the sample's characteristics, including thickness, density, and composition. Therefore, matrix effects can be negligible in the present study. Spectra for 10 mg and 100 mg samples will be found in Appendix B.

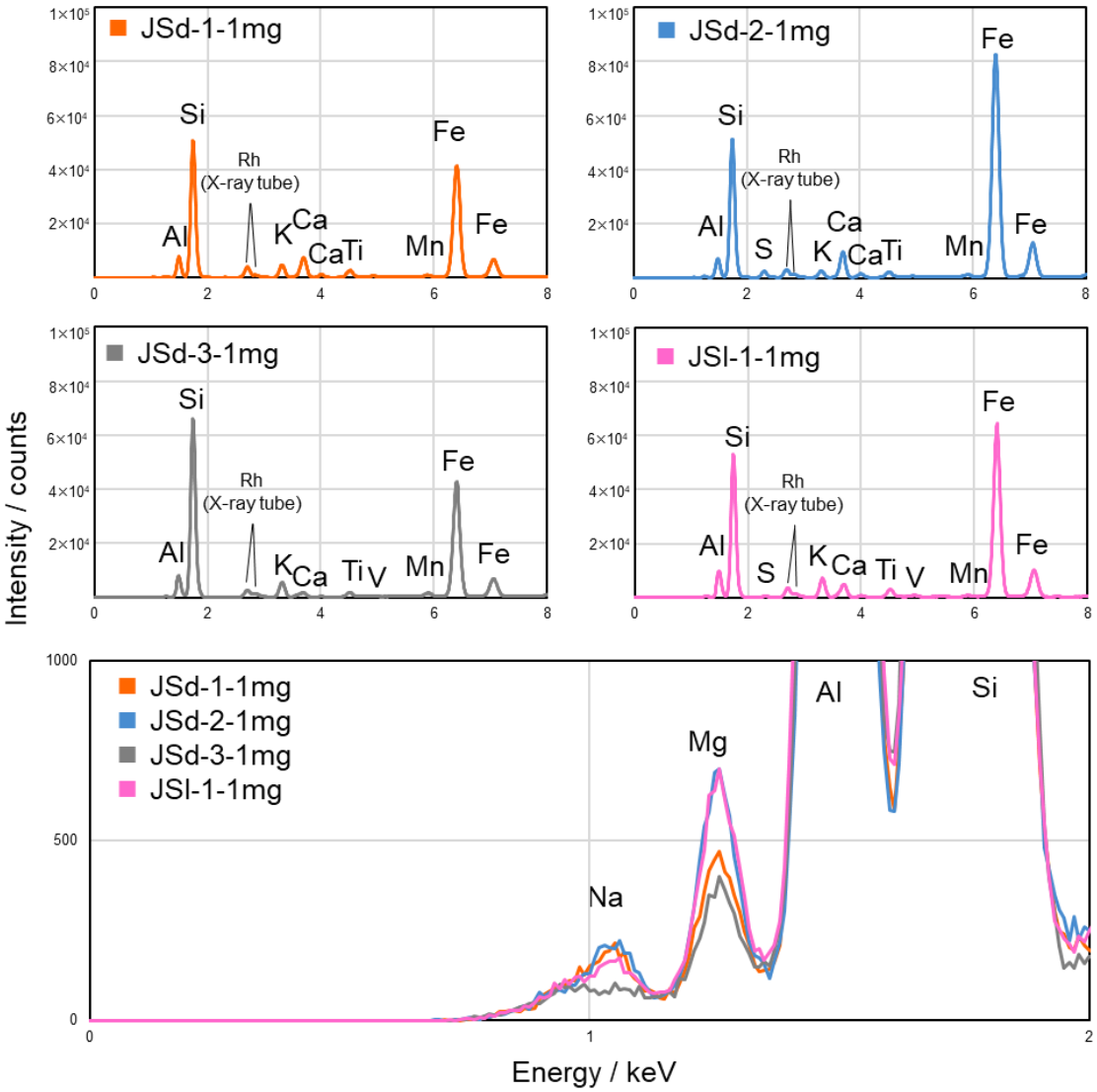

Figure 3.5 Comparison of XRF spectra for samples weighing 1 mg in lower energy regions. Each spectrum indicates a single measurement of the respective sample.

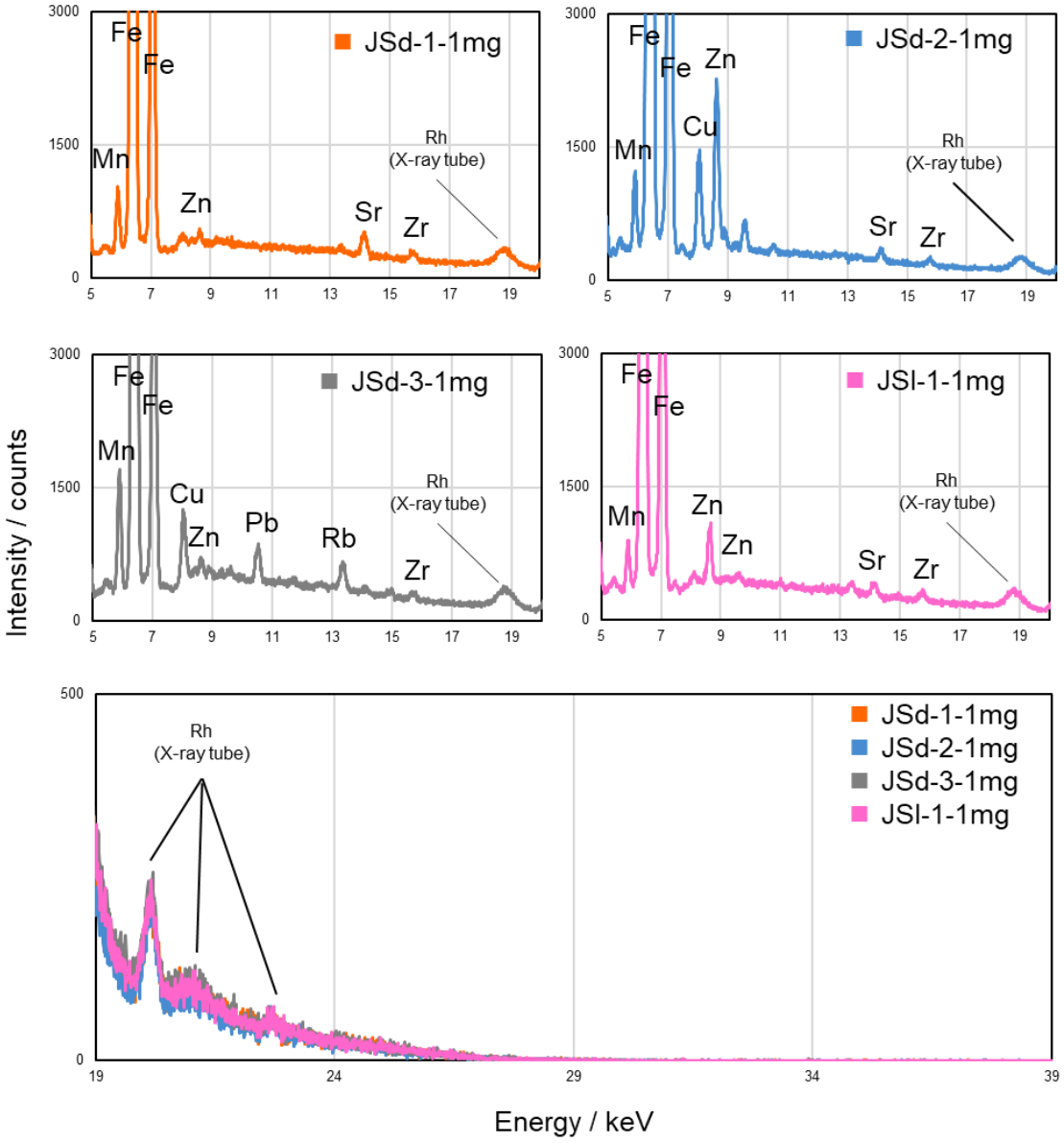

Figure 3.6 Comparison of XRF spectra for samples weighing 1 mg in higher energy regions. Each spectrum indicates a single measurement of the respective sample.

3.3.2 Evaluation of quantitative accuracy

Subsequently, we quantified elements using spectra, and we compared quantitative values with reference values (Figure 3.7). In all samples, the resulting values of major and minor elements are in good agreement with reference ones, which indicates a strong linearity and correlation. The resulting plots for 10 mg and 100 mg with details will be found in Appendix B. Table 3.3 summarizes the correlation coefficients R^2 given for different conditions. As a consequence, we obtained 0.99 or above R^2 in almost all conditions. Notably, Table 3.3 shows no significant difference in the R^2 between sample masses for individual samples. However, it should be noted that the R^2 for minor elements of JSd-3 and JSl-1 are, on average, around 0.9 and 0.7, respectively. One contributing factor to this lowering R^2 is a larger deviation of the quantitative values of Pb from its reference value and non-detection of Ba in JSd-3. The quantification of these elements necessitates deeper cells with an approximately 1.5 mm depth or more based on a theoretical calculation.

Table 3.3 Correlation coefficients R^2 for different samples and sample masses.

	JSd-1		JSd-3		JSl-1	
	major	minor	major	minor	major	minor
100 mg	0.9999	0.9994	0.9953	0.6476	0.9992	0.8725
10 mg	0.9992	0.9981	0.9978	0.6850	0.9979	0.8503
1 mg	0.9998	0.9977	0.9953	0.7654	0.9997	0.9589

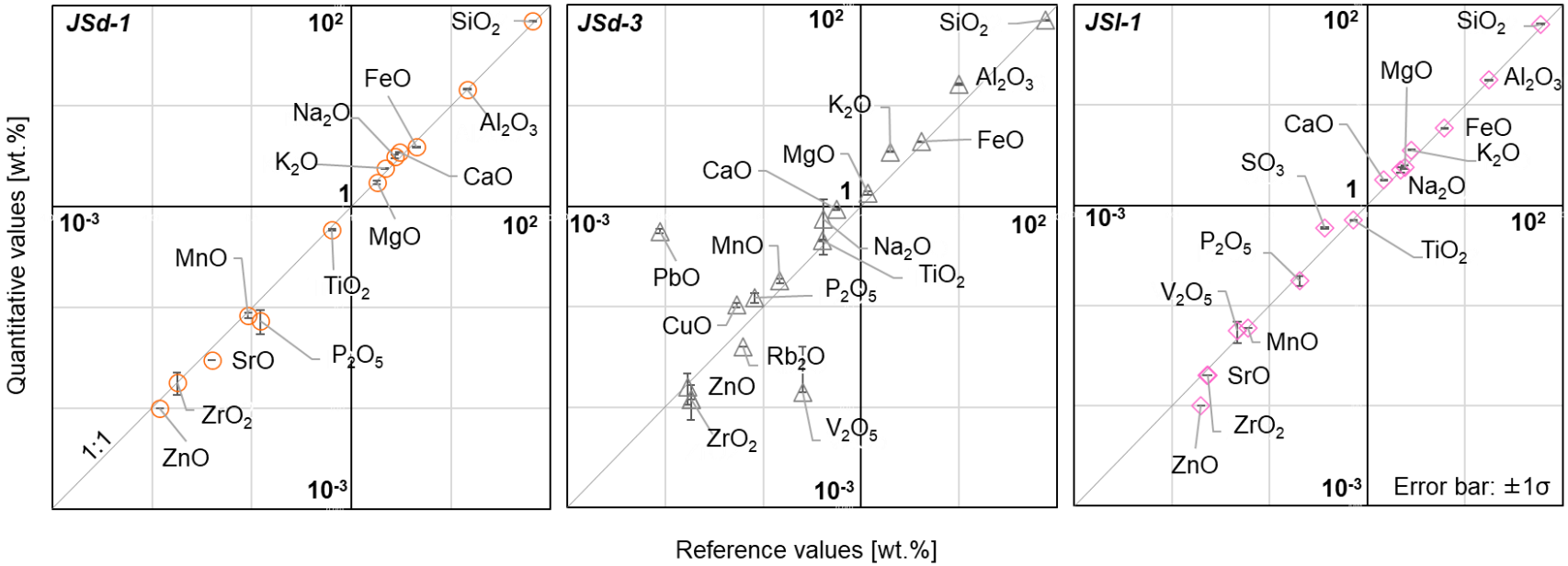

Figure 3.7 The accuracy in quantitative analysis in comparison with reference values. The error bars indicate 1σ of 10 times repeated measurements.

3.3.3 Three contributing factors to the improvement

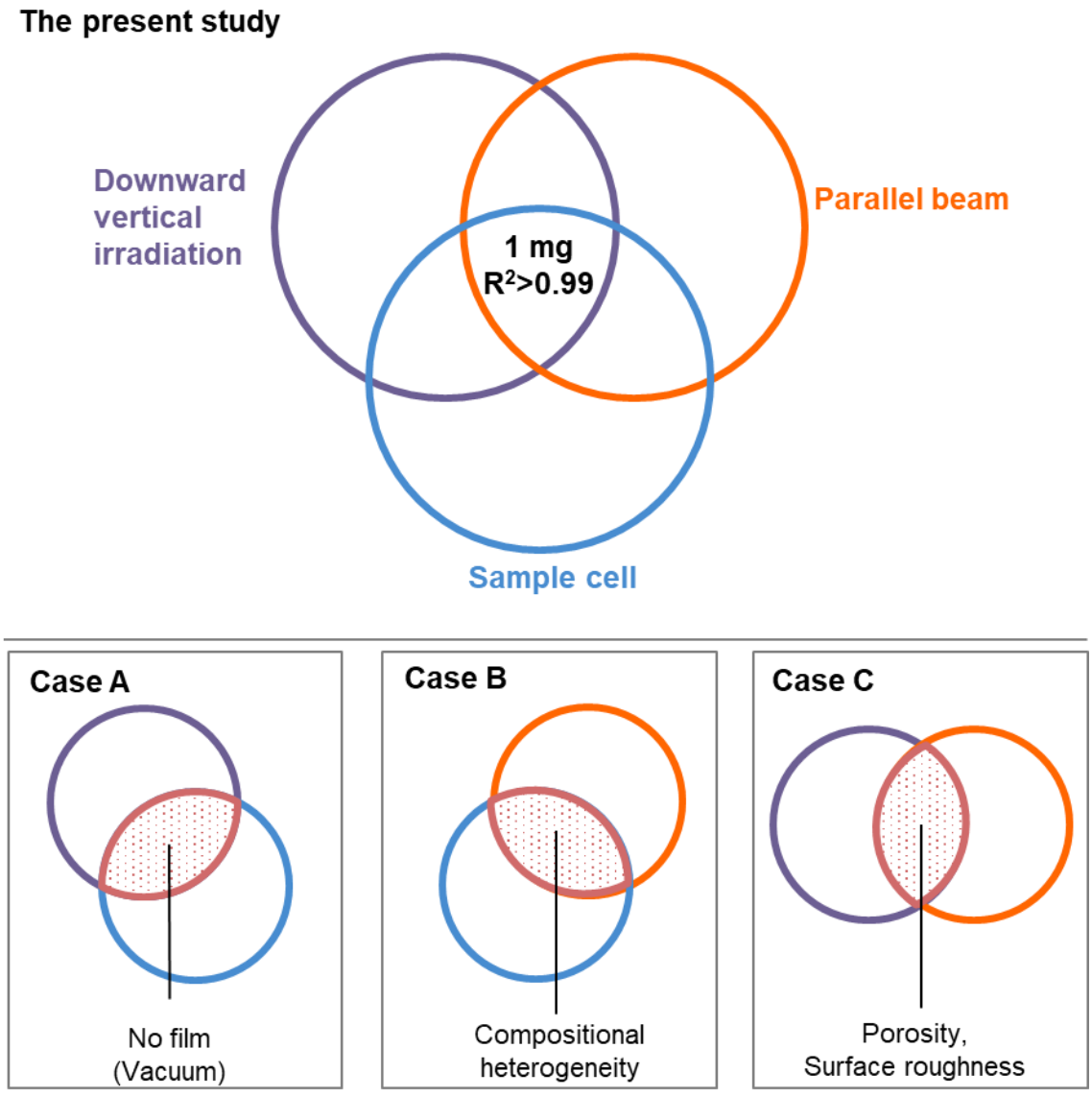

Figure 3.8 Schematic drawing of the three contributing factors to the performance.

The previous subsection demonstrated that we achieved the benchmark. In this subsection, the author discusses how this achievement was made. Figure 3.8 is an explanatory illustration that the three factors are essential for this achievement: downward vertical irradiation, parallel beam, and the design of the sample cell. Let us assume each case where one factor is missing. In Case A, the downward vertical irradiation and the opening top of the sample cell will enable measurements of such powdery specimens under

vacuumed conditions without covers of plastic films. Parallel beams are advantageous to the heterogeneity of sample characteristics, including porosity (density), surface roughness and composition. In Case B or Case C, either of the two others can reinforce this advantage. In short, none of the cases will achieve the benchmark. In this regard, the author further examined whether this synergetic effect contributed to the performance or not by replicating Case B (Figure 3.9). Indeed, the orange spectrum equivalent to the present study realized the highest peak intensities of Na and Mg than the others. Note that the Mg peak is moderate, but Na is barely present in the gray spectrum. This attenuation is because the optics below the specimen under vacuumed conditions may have prevented the sensitivity from decreasing.

3.4 Concluding remarks

The novel sample cell developed here can compact limited quantities of samples in a non-invasive manner. Moreover, it attained the required density and analytical depth for quantifying elements. The results demonstrated that we achieved the goal of quantifying samples weighing 1mg accurately thanks to the combination of the two advantageous aspects of the instrumentation: downward vertical irradiation and parallel beam. In addition, we confirmed from experiments that these three factors produced a synergetic effect on the analyzed results. Although the lack of cell depth led to the failure of quantifying heavier elements, such as Pb and Ba, the results were in good agreement with reference values for a variety of components: Na among light elements, Mn or Rb among minor elements at around 100 ppm, or Si among major elements. The proposed approach will be a powerful solution to analyze a limited quantity of heterogeneous and complex samples, namely, fragments of materials left at the crime scenes, a piece of artwork, or a

chip of archaeological specimens.

(a)

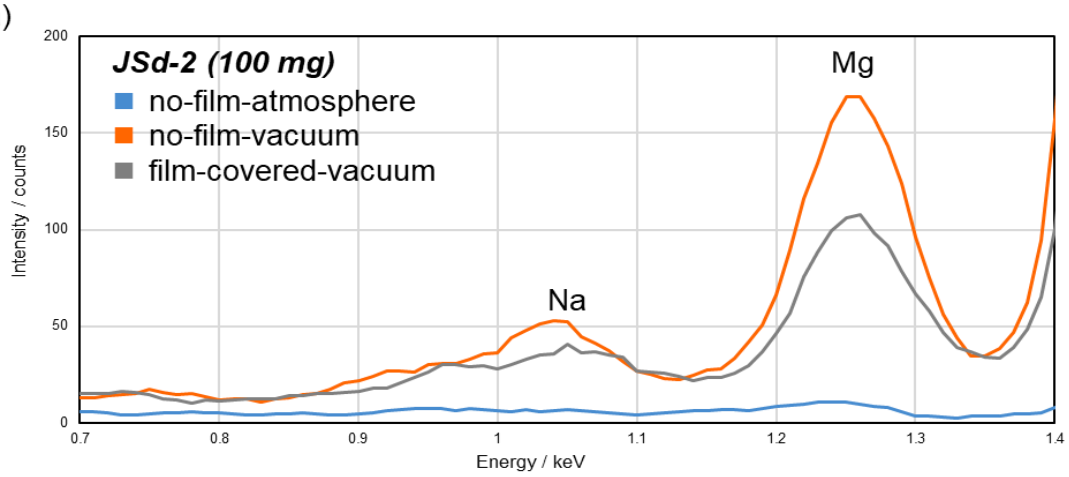

(b)

	Downward vertical irradiation	Sample cell
no-film-atmosphere 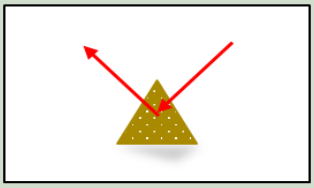	✓	
no-film-vacuum 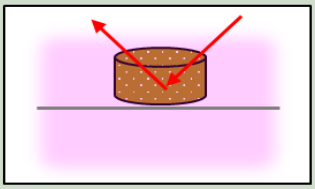	✓	✓
film-covered-vacuum 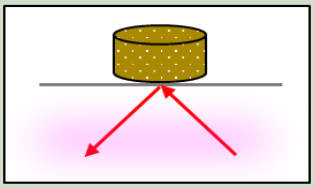		✓

Figure 3.9 (a) XRF spectral comparison of JSd-2 in different conditions (b) explaining the contributing factors. In Figure 3.9(b), red arrows indicate excitation beams, and the shadows in magenta indicate a vacuumed atmosphere.

3.5 Bibliography

Homma, H. (2016). 試料調製法 [Sample pre-treatments]. In I. Nakai (Ed), *蛍光X線分析の実際* [Principles and practices of X-ray fluorescence analysis] (pp. 70-89). Asakura Publishing Co., Ltd

Ichikawa, S., & Nakamura, T. (2014). X-ray fluorescence analysis with micro glass beads using milligram-scale siliceous samples for archeology and geochemistry. *Spectrochimica Acta Part B: Atomic Spectroscopy*, 96, 40–50. https://doi.org/10.1016/j.sab.2014.04.002

Ichikawa, S., & Nakamura, T. (2016). Approaches to solid sample preparation based on analytical depth for reliable X-ray fluorescence analysis. *X-Ray Spectrometry*, 45(6), 302–307. https://doi.org/10.1002/xrs.2700

Ichikawa, S., Nakayama, K., & Nakamura, T. (2012). Loose-powder technique for X-ray fluorescence analysis of ancient pottery using a small (100 mg) powdered sample. *X-Ray Spectrometry*, 41(5), 288–297. https://doi.org/10.1002/xrs.2394

Imai, N., Terashima, S., Itoh, S., & Ando, A. (1996). 1996 COMPILATION OF ANALYTICAL DATA ON NINE GSJ GEOCHEMICAL REFERENCE SAMPLES, "SEDIMENTARY ROCK SERIES". *Geostandards Newsletter*, 20(2), 165–216. https://doi.org/10.1111/j.1751-908X.1996.tb00184.x

Ito, T., Ohbuchi, A., Nakano, K., Sasai, T., & Xue, Z. (2019). Simple Measurement of the Major Elemental Composition with SEM-EDX and Its Application to a Geological Survey. *BUNSEKI KAGAKU*, 68(6), 373–380. https://doi.org/10.2116/bunsekikagaku.68.373

Morita, M., Aoyama, T., Nakano, H., & Komatani, S. (2022). Practical Application of Elemental Imaging for Light Elements, Including Oxygen and Fluorine in Industrial

Materials by Micro-EDXRF. *Advances in X-ray Chemical Analysis, Japan*, 53, 139–149.

Nishino, M. (2016). 定量分析 [Quantitative analysis]. In I. Nakai (Ed), *蛍光 X 線分析の実際* [Principles and practices of X-ray fluorescence analysis] (pp. 90-119). Asakura Publishing Co., Ltd.

Ohzawa, S. (2008). Development of X-ray Guide Tube. *HORIBA Readout English Edition,* 12,78–83.

Onoda, M., Nakano, H., Yamazaki, H., Tanaka, S., & Komatani, S. (2020). Analytical technique for high-accuracy FPM of trace powdered samples. *Advances in X-ray Chemical Analysis, Japan.*, 51, 65–79.

Onoda, M., Tanaka, S., & Komatani, S. (2023). Development of a sample cell for scarce powdery samples and an analytical method using the X-ray fluorescence analyzing instrument (JP Patent No. 7208882). Japan Patent Office.

Sherman, J. (1955). The theoretical derivation of fluorescent X-ray intensities from mixtures. *Spectrochimica Acta*, 7, 283–306. https://doi.org/10.1016/0371-1951(55)80041-0

Shiraiwa, T. & Fujino, N. (1966). Theoretical Calculation of Fluorescent X-ray Intensities in Fluorescent X-ray spectrochemical Analysis. *Japanese Journal of Applied Physics*, 5, 886. https://doi.org/10.1002/xrs.1300130203

Takahashi, H. (2016). SEM-EDS. In I. Nakai (Ed), 蛍光 X 線分析の実際 [Principles and practices of X-ray fluorescence analysis] (pp. 152-168). Asakura Publishing Co., Ltd.

Takahashi, G. (2015). Sample preparation for X-ray fluorescence analysis. *Rigaku J*, 31(1), 26–30.

Chapter 4 Matrix effect-free quantification

4.1 Introduction

4.1.1 Facing to Challenge 2: Matrix effects

Chapter 3 described the development of the quantitative method of micro-energy-dispersive X-ray fluorescence (micro-XRF) through the unique sample cell for exceptionally rare samples (Onoda et al., 2020). Moreover, micro-XRF in Chapter 2 has analyzed even lighter elements like carbon (Morita et al., 2022). However, the so-called matrix effects are formidable even with a combination of the two techniques.

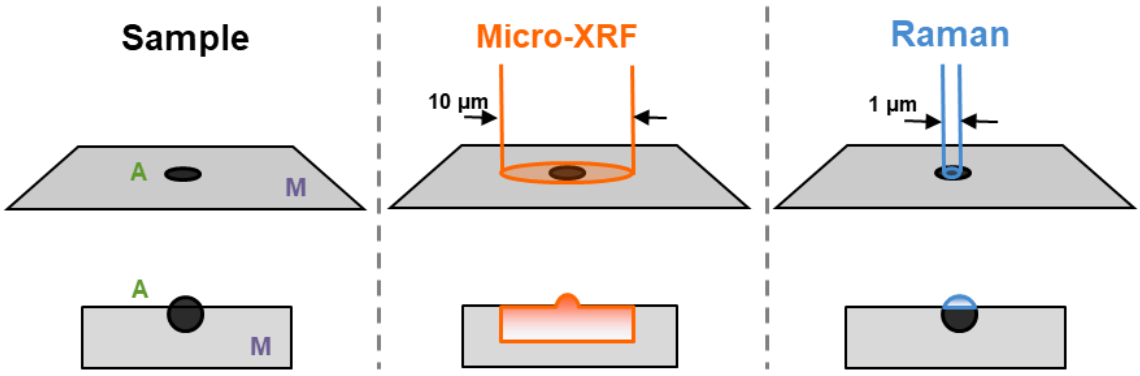

Figure 4.1 Schematic illustration of different excitation volumes between micro-XRF and Raman micro-spectroscopy. A sample with heterogeneous compositions comprises a small analyte depicted by "A" and a sample matrix "M." Micro-XRF three-dimensionally excites A and M, indicated by the orange area. On the other hand, Raman micro-spectroscopy excites the analyte alone (the blue area) thanks to its excellence in both lateral and spatial resolutions.

Figure 4.1 draws a heterogeneous sample with a micrometer-scaled analyte on the sample matrix. Micro-XRF beams excite not only the analyte but also the surrounding matrix, because its spatial resolution is around 10 μm at best. In addition, X-rays easily penetrate through the analyte, and consequently, the resulting signals expand into the three-dimensional volume. In this case, compared with a spectrum of the analyte isolated, the intensities of the background or peaks vary. Further, indistinguishable peaks of the

analyte from the matrix occur. Principally, the fluorescence of an element included both in the analyte and the matrix cannot be separated. In short, the XRF spectrum results in jumbled patterns and peaks of the analyte and the matrix. As a result, the matrix effects reduce quantitative accuracy, which is called “matrix effects.”

Although Raman micro-spectroscopy alone presents the difficulty in providing reference-free quantitative analysis, it can offer information on even slight changes in molecular or crystal structures with superior lateral resolution (typically 1 μm). It also has quite excellent spatial (depth) resolution, approximately several microns, which depends on the wavelength of incident light and the substance. Importantly, since the spectral patterns of Raman scattering derive from molecular or crystal structures, it enables us to distinguish Raman signals of the aimed molecules or crystals selectively from those of the matrix. In other words, this analyte-selective technique is unaffected by any matrix effects.

4.1.2 Carbonate is foreign matter

Over the decades, multi-functionalization of materials and miniaturization of products have advanced. These objects often have surface roughness and a complicated structure. The matrix effects discourage quantitative analyses of such specimens. An example in industry is foreign matter on a sample matrix. Substances of foreign matter are numerous and are classified into two groups: organic and inorganic. The organic group comprises pieces of rubbers and plastic resins. Examples in the inorganic group are metal, stone, and carbonate. Carbonates are, in fact, ubiquitous from an industrial point of view. For example, fillers, pigments, and food additives made of carbonate are mixed into products (Jimoh et al., 2018). Moreover, they have been used as raw materials in glass and steel manufacturing (Jimoh et al., 2018). They are also not originally present in base

materials, but they arise in various reactions with externals on the interface, surface, and inside of buildings, concrete (Ashraf, 2016), or meteorites (Brearley, 2006). They are heterogeneously found in "primitive" meteorites formed during the early stages of the solar system (Brearley, 2006). As the temperature of parental bodies of meteorites rises due to radioactive decay, ice grains thaw, resulting water interacts with rocks, and the interaction generates various carbonates. Therefore, their cation composition is evidence of aqueous alteration, and their variation in species represents the difference in thermo- and hydro- chemical dynamics of the aqueous environments (Rubey, 1951; Morse & Mackenzie, 2003; Tucker & Wright, 2003; Brearley, 2006).

Natural carbonates include diverse variations in cation composition. For example, with the continuous substitutions of Mg^{2+}-Fe^{2+}-Mn^{2+}, dolomite $CaMg(CO_3)^2$, Mn^{2+}-rich dolomite called kutnohorite [$CaMn(CO_3)^2$], Fe^{2+}-rich dolomite called ankerite [$CaFe(CO_3)^2$], form a solid-solution series (Reeder & Dollase, 1989; Chai & Navrotsky, 1996). The end member chemical formulae of ankerite and kutnohorite, described in square brackets, are quite rare, and ideal ankerite nearly exists due to its inherent instability (Davidson et al., 1993). For this reason, it is sometimes referred to as ferroan dolomite (Kim et al., 2021). Similarly, magnesite [$MgCO_3$], breunnerite [$(Mg,Fe)CO_3$], and siderite [$FeCO_3$] form a solid solution series with the continuous substitution of Mg^{2+} and Fe^{2+}. On the other hand, the Ca-Mg substitution indicating between calcite [$CaCO_3$] and magnesite barely occurs, and dolomite having a well-defined structure only arises (Reeder & Dollase, 1989; Chai & Navrotsky, 1996).

4.1.3 Matrix effect-free quantification

Interestingly, Urashima et al. (2022) found nearly linear relations of Raman wavenumbers of CO_3^{2-} vibration modes against cation compositions of these carbonate

species. In this chapter, we constructed the universal conversion matrix that provides the cation composition for a carbonate species, utilizing micro-XRF and Raman micro-spectroscopy. Since the patterns of Raman spectra are highly dependent on the mineral structure of that sample, estimating cation compositions from Raman spectra is essentially carbonate-selective and free from any matrix effects.

4.2 Experiments

4.2.1 Samples

The carbonates analyzed were calcite, siderite, rhodochrosite, magnesite, breunnerite, dolomite, ferroan dolomite, and kutnohorite. Mined locations are listed in Table 4.1. Images of the carbonate samples are shown in Figure 4.2. Among the carbonates used, magnesite, siderite (EP), ferroan dolomite, and kutnohorite (W) were also analyzed in the previous study (Urashima et al., 2022). For standard FPM in XRF spectrometry, a geo standard named JLk-1 sampled from the Biwa-ko Lake, Japan, was used. It is not a carbonate but was necessary because the standards JLs-1 and JDo-1 do not include calibrated elements, Fe^{2+}, Mn^{2+}, or both.

Table 4.1 Summary of the carbonates used in this study. [a]: Evaluated by XRF.

	mined location	cation composition[a]			
		Ca	Mg	Fe	Mn
calcite	Garo, Hokkaido, Japan	0.979 ± 0.002	0.020 ± 0.003	0.002 ± 0.000	0.000 ± 0.000
magnesite	Goat Hill Magnesia Quarries, Pennsylvania, USA	0.016 ± 0.000	0.981 ± 0.001	0.003 ± 0.000	0.000 ± 0.000
siderite (EP)	El Potosí Mine, Chihuahua, Mexico	0.080 ± 0.003	0.019 ± 0.005	0.765 ± 0.011	0.133 ± 0.004
siderite (MV)	Morro Velho Mine, Minas Gerais, Brazil	0.004 ± 0.001	0.438 ± 0.010	0.569 ± 0.112	0.018 ± 0.003
rhodochrosite	Sweethome Mine, Colorado, USA	0.002 ± 0.001	0.012 ± 0.003	0.006 ± 0.001	0.980 ± 0.004
breunnerite	Kyshtym, Chelyabinsk Oblast, Russia	0.005 ± 0.001	0.702 ± 0.012	0.264 ± 0.012	0.029 ± 0.001
dolomite	Kuzuu, Tochigi, Japan	0.567 ± 0.002	0.433 ± 0.002	0.000 ± 0.000	0.000 ± 0.000
ferroan dolomite	Eagle Mine, Colorado, USA	0.521 ± 0.001	0.306 ± 0.003	0.113 ± 0.003	0.060 ± 0.001
kutnohorite (SH)	Sterling Mine, New Jersey, USA	0.661 ± 0.024	0.032 ± 0.023	0.004 ± 0.000	0.303 ± 0.011
kutnohorite (W)	Wissels mine, Northern Cape, South Africa	0.126 ± 0.007	0.038 ± 0.007	0.004 ± 0.001	0.832 ± 0.010

Table 4.1(continued.)

	Raman frequency [cm^{-1}]		notes
	T	L	
calcite	156.1 ± 0.3	281.8 ± 0.5	Geostandard JLs-1
magnesite	212.5 ± 1.0	329.3 ± 1.0	
siderite (EP)	181.9 ± 0.7	283.4 ± 0.5	
siderite (MV)	196.9 ± 0.3	304.6 ± 0.5	
rhodochrosite	184.9 ± 0.7	290.0 ± 0.6	
breunnerite	204.8 ± 0.9	316.4 ± 1.0	
dolomite	176.6 ± 0.3	298.8 ± 0.6	Geostandard JDo-1
ferroan dolomite	172.7 ± 0.7	293.5 ± 1.2	
kutnohorite (SH)	162.4 ± 2.0	286.1 ± 1.1	
kutnohorite (W)	179.7 ± 1.9	286.4 ± 1.4	

Figure 4.2 Images of the carbonates studied. Scale bars correspond to 10 mm.

4.2.2 Raman spectroscopy

Experimental conditions, calibration procedure, and the analytical method for peak determination were the same as our previous report described (Urashima et al., 2022). Concisely, the Raman spectra were obtained by Raman-11i (nanophoton) combined with a microscope Eclipse Ti (Nikon). The objective lens was Nikon Plan Fluor (40x, NA 0.75, WD 0.66). Excitation wavelength, power, and duration were 532 nm, 10 mW, and 120 seconds, respectively. The apparatus was constructed as a slit-confocal optical system. In the present study, the slit width was 50 μm. The grating was 1200 grooves/mm. Under these conditions, the spatial resolution for the measurements was about 1 μm, and the spectra were recorded from about -30 to +1270 cm^{-1} at every ~1.1 cm^{-1}. Each spectrum was averaged of two consecutive measurements, and at least 10 different spots on each sample were measured to examine the homogeneity. Some spectra unable to be assigned

to carbonates were obtained only at a few spots, and therefore, they were excluded from the analysis.

The spectra obtained were then calibrated by Raman bands of sulfur flake (153.8, 219.1, and 473.2 cm^{-1}) or a silicon wafer (520.6 cm^{-1}) (Hutsebaut et al., 2005; Petriglieri et al., 2015). The full-width-of-half-maximum of the silicon peak at 520.6 cm^{-1} was approximately 4-5 cm^{-1}. This indicates that the spectral resolution of the measurements was, at worst 4-5 cm^{-1}.

4.2.3 Micro-XRF

HORIBA XGT-9000 X-ray Analytical Microscope was used for micro-XRF analyses. The instrument configuration is the same as already described in Chapter 2 (Morita et al., 2022). The X-ray tube voltage was 30 kV, and the tube current was 100–1000 μA, and the working distance was 1 mm (the focal point). The diameter of the primary X-rays focused was approximately 100 μm at the focal point. After elemental imaging for the entire area of a respective sample at 10 μm of step size and 200 ms measurement time per pixel, spectra of 16 different spots were further analyzed with an acquired measurement time of approximately 30 s per spot. The standard fundamental parameter method (Sherman, 1955; Shiraiwa & Fujino, 1966) was used to determine the elemental composition. The element abundance for each was calibrated with the geo-standards JLs-1 for calcite, JDo-1 for dolomite and magnesite, and JLk-1 for the other carbonates, respectively.

4.3 Results and Discussions

4.3.1 Typical pattern for carbonates of Raman spectra

Urashima et al. (2022) reported that there were four distinct Raman bands at around 200,

300, 700, and 1100 cm^{-1} (Figure 4.3). Two prominent bands at 200 and 300 cm^{-1} are lattice motions of CO_3^{2-} unit: translational (T) mode and librational (L) mode, respectively (White, 1974; Couture, 1947). The other bands are bending and stretching vibration of CO_3^{2-} unit: ν_4 and ν_1, respectively (Farsang et al., 2018; Rividi et al., 2010; Buzgar & Apopei, 2009; Gillet, 1996; Spivak et al., 2014). Notably, Raman-active modes of carbonates originate in vibrational motions of CO_3^{2-} ion. Hence, these four bands appear in the spectra of any carbonate species. Interestingly, Urashima et al. (2022) and other research groups (Dufresne et al., 2018; Kim et al., 2021; Herman et al., 1987; Farsang et al., 2018; Rutt & Nicola, 1974) indicated a correlation between kinds of carbonate and these Raman frequencies.

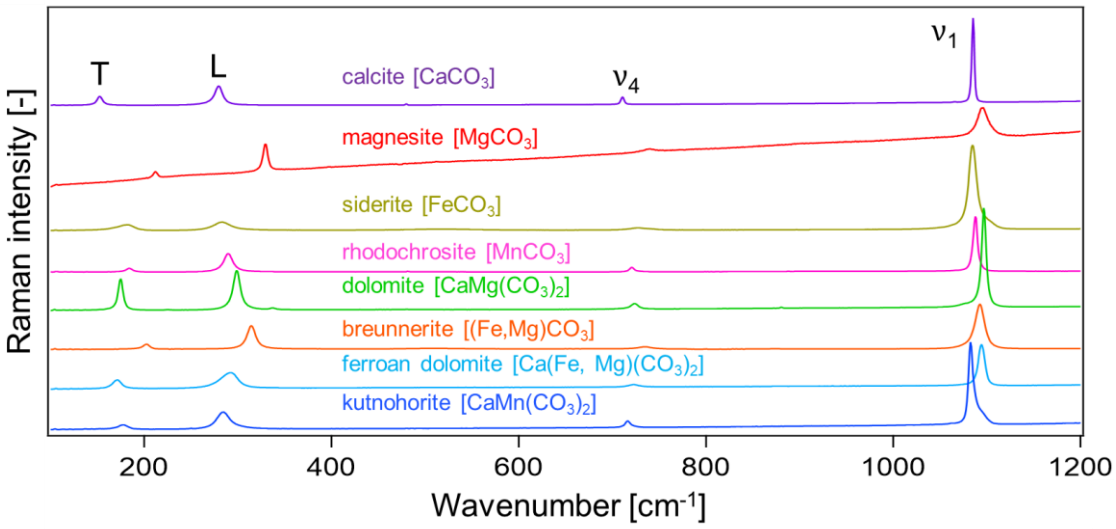

Figure 4.3 Raman spectra of carbonates. T: translational, L: librational. The data are cited from (Urashima et al., 2022) and modified.

These Raman bands significantly correlates with only single cation carbonates (single salts): calcite, magnesite, siderite, and rhodochrosite. In contrast, the correlations with carbonates bearing multiple cations (*e.g.,* double salts), specifically dolomite or breunnerite, are weak. Understanding the relationship between crystal systems of single or multiple cation species and the Raman bands will help us explain these inconsistent

correlations (Figure 4.4). For example, the most prominent band ν_1 out of the four corresponds to in-plane stretching and reflects only "local" motions of CO_3^{2-} ions, which depend on ionic radii and nearest neighbor distances. Natural carbonates bearing different cations randomly substituted should have more complicated vibrational movements of cations and anions than single cation carbonates should do. Therefore, ν_1 limitedly works for single cation species. In contrast, T or L mode are lattice vibrational modes, which can represent "global" movements of vibrations of that entire crystal system. The two modes reflect slight crystal distortions caused by the cation substitution more clearly. In the present research, we hence biaxially plotted two bands of lattice mode to examine a consistent relationship between Raman shifts of lattice modes and cation composition in carbonate species based on the precedented study (Urashima et al., 2022).

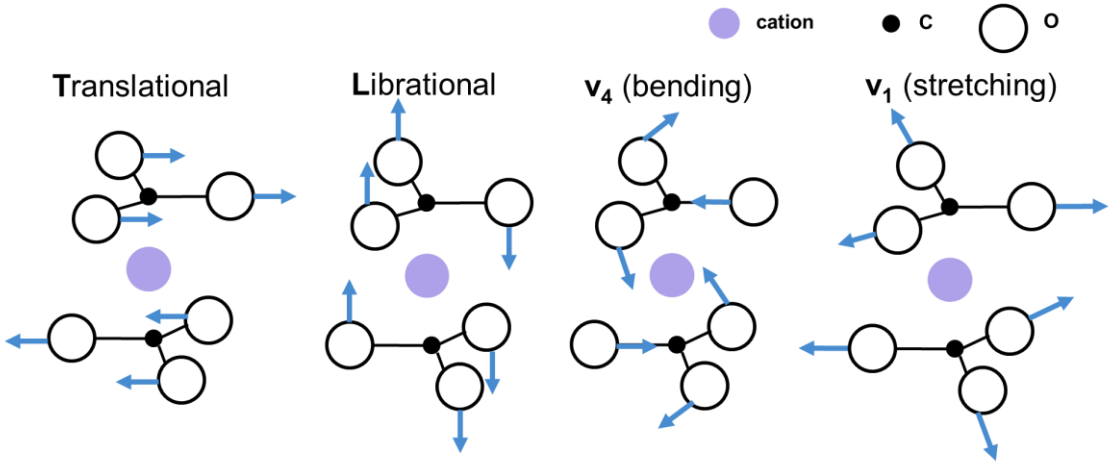

Figure 4.4 Four Raman bands corresponding to vibrations of carbonate ions. The figure is modified from the reference (Morse & Mackenzie, 2003).

4.3.2 Correlation between the cation composition and biaxial plot

The cation compositions for each sample and a ternary diagram are shown in Table 4.1 and Figure 4.5(a), respectively. Expectedly, three plots of siderite and two kutnohorites are entirely different. Remarkably, the cation compositions of magnesite, breunnerite and

siderite (MV) differed only in the Mg: Fe ratio. This result strongly implies that the three samples can comprise a typical magnesite-siderite-solid solution (Morse & Mackenzie, 2003). The cation composition of the siderite (EP) was close to that of pure $FeCO_3$, but the Mn+Ca abundance was not negligible. Since the ternary substitution of Mg-Fe-Mn occurs in the dolomite-ankerite-kutnohorite solid solution series (Morse & Mackenzie, 2003), it should be more complicated than the magnesite-siderite solid solution series. Notably, the ternary diagram shows that JDo-1 and ferroan dolomite contain more than 50% of Ca, which exceeds the expectation. The reason for this overestimated Ca content will be discussed in the next chapter.

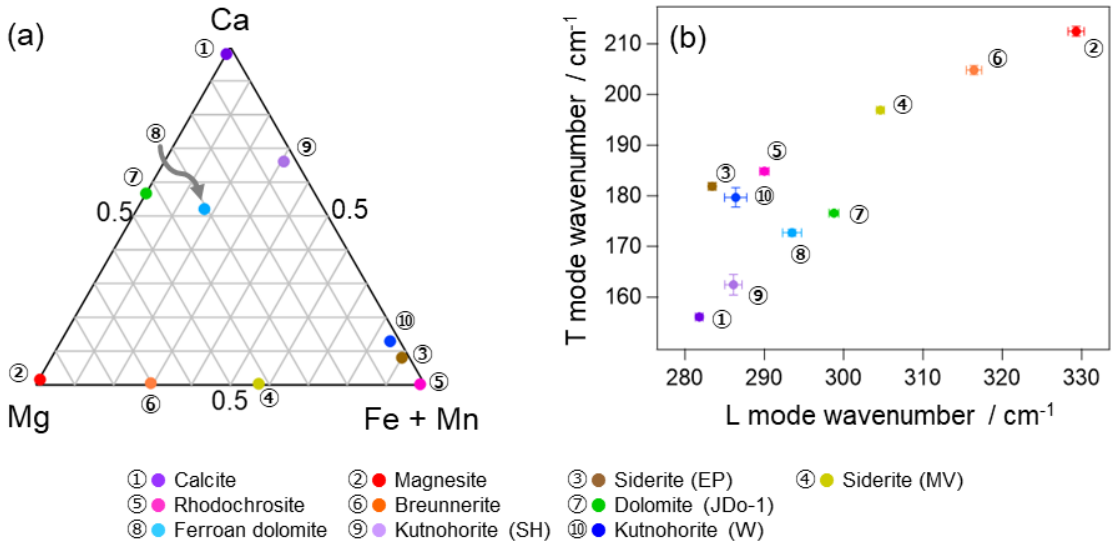

Figure 4.5 (a) Ternary diagram and (b) the T-L biaxial map for the 10 carbonates. Numbers are given to each species for clarification.

The Raman spectra obtained for some samples, such as calcite, magnesite and siderite (EP) did not have significant differences from the ones previously reported (Urashima et al., 2022), and others for kutnohorite (SH) and siderite (MV) did. The peak wavenumbers are summarized in Table 4.1. Figure 4.5(b) is a biaxial plot of T and L modes. Since the cation composition of single-salt carbonates should not depend on the

mined location, the reproductive peak wavenumbers illustrate that our measurements and analyses are sufficiently valid. Also, the peak wavenumbers observed were in good agreement with those reported by other researchers (Dufresne et al., 2018; Herman et al., 1987; Farsang et al., 2018; Rutt & Nicola, 1974; Kim et al., 2021). As previously described, the Raman spectra of kutnohorite (SH) and siderite (MV) differed from those once obtained by our group for kutnohorite (W) and siderite (EP), respectively. This discrepancy can be attributed to the different cation compositions in the samples, as indicated by XRF measurements (Table 4.1 and Figure 4.5(a)). Dolomite [$CaMg(CO_3)_2$] named JDo-1 and ferroan dolomite were located between calcite [$CaCO_3$] and magnesite [$MgCO_3$] in the T-L biaxial map, and breunnerite [$(Fe, Mg)CO_3$] was between siderite [$FeCO_3$] and magnesite [$MgCO_3$]. The linear movement in the biaxial map thus reflects the partial substitution of Ca-Mg (calcite-magnesite) or Mg-Fe (magnesite-siderite). The slopes of the lines are different due to different cations contributing to the substitution. Similarly, both of the two kutnohorites (SH) (W) [$CaMn(CO_3)$] are between calcite [$CaCO_3$] and rhodochrosite [$MnCO_3$] as expected.

4.3.3 Establishment of conversion matrices

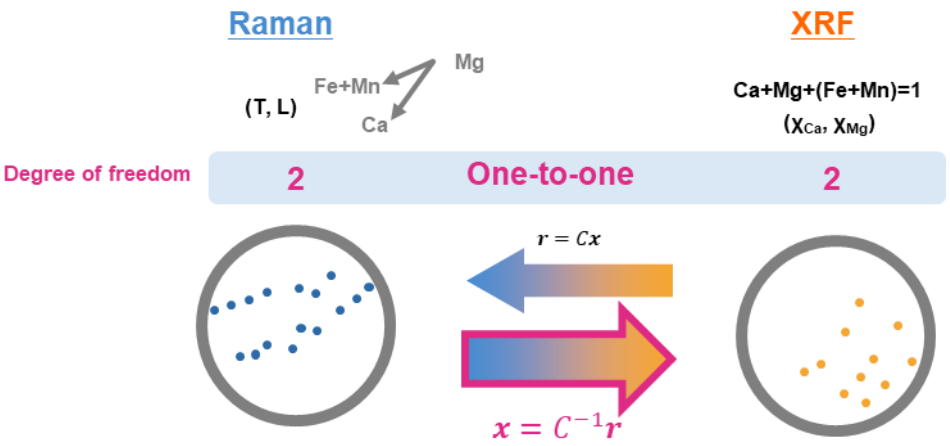

Figure 4.6 Conceptual drawing of the establishment of conversion matrices.

In short, there are two lines (Ca-Mg [calcite-magnesite] and Mg-Fe [magnesite-siderite]) corresponding the ternary diagram to the biaxial plot. This implies a cation-dependent trend in Raman shifts of the lattice modes. As the Mg content increase, the T and L modes become higher wavenumbers. As the Fe+Mn contents increase, the two modes become lower wavenumbers. Furthermore, the author focused on the fact that the degree of freedom for the ternary diagram is equal to that for the biaxial plot. This author's idea is illustrated in Figure 4.6. In other words, the Raman shifts are obtained by only two T and L modes; the cation compositions by XRF are also obtained by two variable cation ratios, namely, Ca and Mg, given that the sum of cation ratios is always 1, and that Fe and Mn are indistinguishable. Averaging Fe and Mn cation ratios will be discussed later. Here, the author hypothesized that we could create conversion matrices that corresponded to each other's sets in a one-to-one manner. From a perspective of analytical chemistry, it is noteworthy that the Raman-to-XRF conversion provides us with a matrix effect-free quantification.

Conversion from XRF data to Raman wavenumbers

First, we tried setting a fixed point vector by establishing a conversion matrix transforming from the cation composition in XRF to the Raman wavenumbers. Assuming that the vibrational wavenumbers of T and L modes shift linearly with the cation substitution based on the T-L biaxial map, we can derive the Raman wavenumbers from the linear combination of "composition vectors" $\boldsymbol{v_{Ca}}$, $\boldsymbol{v_{Mg}}$, $\boldsymbol{v_{Fe}}$, $\boldsymbol{v_{Mn}}$ and the origin vector $\boldsymbol{v_o}$. Hence, the Raman wavenumbers are described by the cation composition as such:

$$\boldsymbol{r} = \boldsymbol{Cx} \quad (4.1),$$

where $\boldsymbol{r} = \begin{pmatrix} \widetilde{\nu_{\mathrm{T}}} \\ \widetilde{\nu_{\mathrm{L}}} \end{pmatrix}$, is the vector of the peak wavenumbers of the T and L modes in cm^{-1}, $C = (\boldsymbol{v_O} \quad \boldsymbol{v_{Ca}} \quad \boldsymbol{v_{Mg}} \quad \boldsymbol{v_{Fe}} \quad \boldsymbol{v_{Mn}}) = \begin{pmatrix} O_{\mathrm{T}} & C_{\mathrm{T,Ca}} & C_{\mathrm{T,Mg}} & C_{\mathrm{T,Fe}} & C_{\mathrm{T,Mn}} \\ O_{\mathrm{L}} & C_{\mathrm{L,Ca}} & C_{\mathrm{L,Mg}} & C_{\mathrm{L,Fe}} & C_{\mathrm{L,Mn}} \end{pmatrix}$ is the conversion matrix, and $\boldsymbol{x} = \begin{pmatrix} 1 \\ x_{\mathrm{Ca}} \\ x_{\mathrm{Mg}} \\ x_{\mathrm{Fe}} \\ x_{\mathrm{Mn}} \end{pmatrix}$ is vector of the cation compositions ($0 \leq x \leq 1$).

The least square fitting was applied to determine the conversion matrix for the ten carbonates studied here. The resulting conversion matrix C was given as

$$C = \begin{pmatrix} 164.57 & -12.95 & 48.01 & 19.32 & 18.86 \\ 222.38 & 57.19 & 106.91 & 59.71 & 65.86 \end{pmatrix}.$$

The calculated Raman wavenumbers are summarized, and the composition vectors are also presented in Figure 4.7. They roughly agreed with the experimental results, which indicates that our analyses based on the linear assumption were plausible at a certain level.

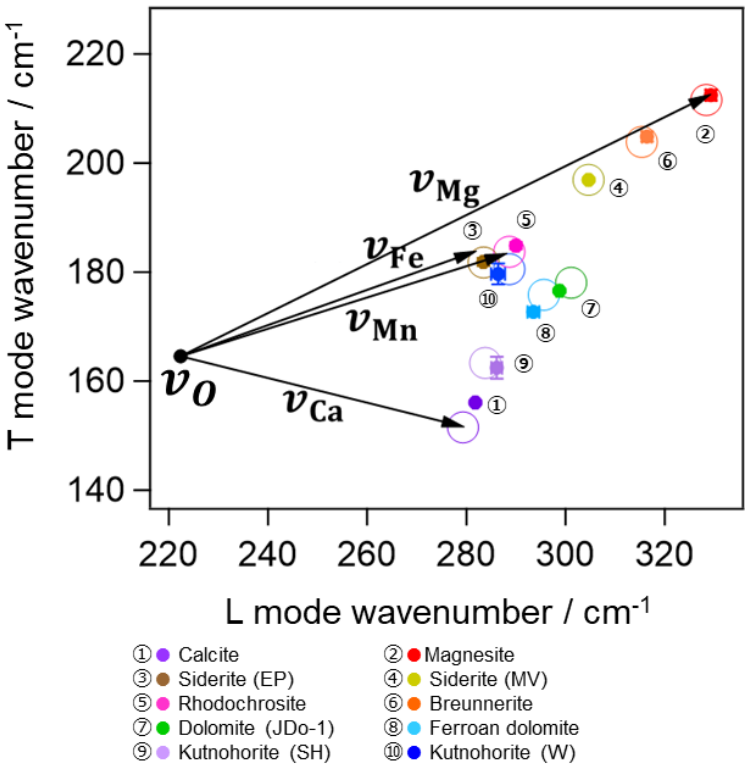

Figure 4.7 Conceptual illustration of the origin vector and composition vectors. Filled circles are experimental data by XRF, and open circles are calculated by Eq. (4.1)

Conversion from Raman wavenumbers to cation compositions

Second, the opposite conversion from the Raman wavenumbers to the cation composition by XRF should be possible with an inverse matrix derived from Eq. (4.1), but the resulting solution will not be unique. Accordingly, we created a new composition vector $\boldsymbol{v_{Fe+Mn}}$ by averaging the two composition vectors $\boldsymbol{v_{Fe}}$ and $\boldsymbol{v_{Mn}}$. This averaging should be reasonable because the similarity in ion size and mass of Fe and Mn among substituting cations leads to negligible Raman shifts. To reduce one more degree of freedom, the condition $x_{\mathrm{Ca}} + x_{\mathrm{Mg}} + x_{\mathrm{Fe}} + x_{\mathrm{Mn}} = 1$ is introduced for the four cations that are the most commonly observed in natural carbonates. Although marine carbonates sometimes include more significant amounts of other elements such as Sr than Fe or Mn (Morse & Mackenzie, 2003), in even these cases, Ca and Mg still dominate the cation composition, and the molar fraction of the other elements is less than 1 % in total. Note that in exceptional cases where the samples of interest contain non-negligible amounts of Sr or other cations, this condition is no longer available. However, the prepared samples with nearly end-member compositions such as calcite, magnesite, rhodochrosite, and siderite (EP) were practically free from cations other than Ca, Mg, Fe, and Mn, specifically, Sr, Co, Cr, Ba, Ni, Zn, Cu, Ti and V. Hence, Eq. (4.1) will be revised as:

$$\boldsymbol{r'} - \boldsymbol{v_0'} = C'\boldsymbol{x'}$$

where:

$$\boldsymbol{r'} - \boldsymbol{v_0'} = \begin{pmatrix} \widetilde{\nu_{\mathrm{T}}} - O_{\mathrm{T}} \\ \widetilde{\nu_{\mathrm{L}}} - O_{\mathrm{L}} \\ 1 \end{pmatrix},$$

$$C' = (\boldsymbol{v_{Ca}} \quad \boldsymbol{v_{Mg}} \quad \boldsymbol{v_{Fe+Mn}}) = \begin{pmatrix} C_{\mathrm{T,Ca}} & C_{\mathrm{T,Mg}} & C_{\mathrm{T,Fe+Mn}} \\ C_{\mathrm{L,Ca}} & C_{\mathrm{L,Mg}} & C_{\mathrm{L,Fe+Mn}} \\ 1 & 1 & 1 \end{pmatrix},$$

and

$$\boldsymbol{x}' = \begin{pmatrix} x_{\mathrm{Ca}} \\ x_{\mathrm{Mg}} \\ x_{\mathrm{Fe}} + x_{\mathrm{Mn}} \end{pmatrix}.$$

In this expression, to make the conversion matrix C' a square matrix, the third row in $\boldsymbol{r}' - \boldsymbol{v}_{\boldsymbol{0}}'$ and C' was introduced from the assumption $x_{\mathrm{Ca}} + x_{\mathrm{Mg}} + x_{\mathrm{Fe}} + x_{\mathrm{Mn}} = 1$, and the first two entr ies, namely, the origin vector in the original C was moved to the left side in the equation. Consequently, the composition vector $\boldsymbol{x}'$ is derived as:

$$x' = C'^{-1}(\boldsymbol{r}' - \boldsymbol{v}_{\boldsymbol{0}}'),$$

specifically,

$$\begin{pmatrix} x_{\mathrm{Ca}} \\ x_{\mathrm{Mg}} \\ x_{\mathrm{Fe}} + x_{\mathrm{Mn}} \end{pmatrix} = \begin{pmatrix} -0.0352 & 0.0231 & -0.7770 \\ -0.0045 & 0.0256 & -1.5212 \\ 0.0397 & -0.0487 & 3.2982 \end{pmatrix} \begin{pmatrix} \widetilde{\nu_{\mathrm{T}}} - 164.57 \\ \widetilde{\nu_{\mathrm{L}}} - 222.38 \\ 1 \end{pmatrix}. \quad (4.2)$$

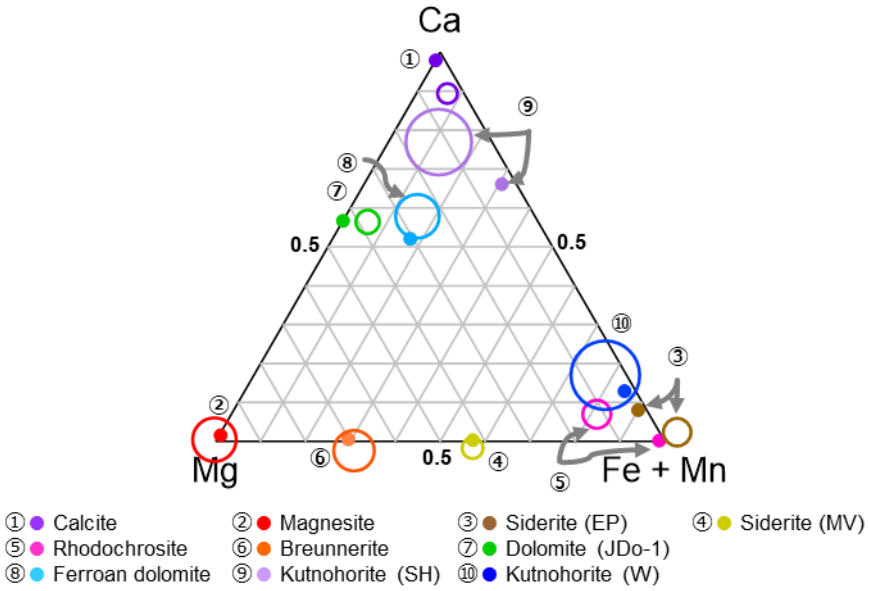

Figure 4.8 Cation compositions of the experimented and calculated plotted in the ternary diagram for comparison. Filled circles are the experimented and blank circles are the calculated values by Eq. (4.2). The radius of the blank circles indicates the root-mean-square of the uncertainties for $\boldsymbol{x}_{\mathbf{Ca}}$, $\boldsymbol{x}_{\mathbf{Mg}}$, and $\boldsymbol{x}_{\mathbf{Fe}} + \boldsymbol{x}_{\mathbf{Mn}}$ derived from the standard deviations of T and L mode wavenumbers.

The resulting cation compositions from Eq. (4.2) are shown in Figure 4.8. As one can

see, the calculated results well reproduced the experiment. The more significant deviations from the experimental results are for Mg-poor species such as kutnohorite (W), kutnohorite (SH), siderite (FP), and rhodochrosite, and they are presumably due to the averaging of the two composition vectors. Notably, the maximum deviation of the calculated compositions (X) from the XRF results was at most 0.2 (20 atom%), even for Fe and Mn. In this regard, this Raman-to-XRF conversion could be more precise but valuable. The validity of the analysis will be found in Appendix C.1.

This result implies that the conversion with Eq. (4.2) is sufficient to roughly estimate the compositions of unknown carbonates with a maximum error of 20% (0.2). One solution for improving in the accuracy of our method is to optimize conversion matrices for each solid solution series. Fine conversion by optimizing the Eq. (4.2) for the dolomite-ankerite-kutnohorite series is discussed in Chapter 5, and the rests are in Appendix C.2. Although accurate determination of the cation composition requires more strict conversion, the universal conversion with Eq. (4.2) is still helpful for discriminating the type of carbonate of interest at the first step of the analysis.

4.4 Summary

Carbonate is one of the inorganic substances of foreign matter predominantly found in artificial objects. However, quantifying foreign matters induces matrix effects. To cope with this challenge, we created conversion matrices from Raman wavenumbers to cation composition of carbonate species or vice versa by combining micro-XRF with Raman micro-spectroscopy in the present study. The conversion matrices developed here were rough but universal and helpful, with a maximum error of 20%. The averaging Fe and Mn cation composition vectors may have accounted for the marked discrepancies between

the experimented and calculated Fe+Mn bearing species of carbonates. For more accurate analysis, the optimization of conversion matrices is strongly desired for each solid solution series in carbonates.

4.5 Bibliography

Ashraf, W. (2016). Carbonation of cement-based materials: Challenges and opportunities. *Construction and Building Materials*, 120, 558–570. https://doi.org/10.1016/j.conbuildmat.2016.05.080

Brearley, A. J. (2006). The Action of Water. In Lauretta, D. S. & McSween, H. Y. (Eds.), *Meteorites and the Early Solar System II* (pp. 587-624). University of Arizona Press, USA.

Buzgar, N., & Apopei, A. I. (2009). The Raman study of certain carbonates. *Geologie Tomul L*, 2(2), 97-112.

Chai, L. & Navrotsky, A. (1996). Synthesis, characterization, and energetics of solid solution along the dolomite-ankerite join, and implications for the stability of ordered $CaFe(CO_3)_2$. *American Mineralogist*, 81(9-10), 1141–1147. https://doi.org/10.2138/am-1996-9-1012

Couture, L. (1947). Étude des spectres de vibrations de monocristaux ioniques. *Annales de Physique*, 12(2), 5–94.

Davidson, P. M., Symmes, G. H., Cohen, B. A., Reeder, R. J., & Lindsley, D. H. (1993). Synthesis of the new compound $CaFe(CO_3)_2$ and experimental constraints on the $(Ca,Fe)CO_3$ join. *Geochimica et Cosmochimica Acta*, 57(23), 5105–5109. https://doi.org/10.1016/0016-7037(93)90612-Z

Dufresne, W. J., Rufledt, C. J., & Marshall, C. P. (2018). Raman spectroscopy of the eight

natural carbonate minerals of calcite structure. *Journal of Raman Spectroscopy*, 49(12), 1999–2007. https://doi.org/10.1002/jrs.5481

Farsang, S., Facq, S., & Redfern, S. A. (2018). Raman modes of carbonate minerals as pressure and temperature gauges up to 6 GPa and 500°C. *American Mineralogist*, 103(12), 1988–1998. https://doi.org/10.2138/am-2018-6442

Gillet, P. (1996). Raman spectroscopy at high pressure and high temperature. Phase transitions and thermodynamic properties of minerals. *Physics and Chemistry of Minerals*, pages 263–275. https://doi.org/10.1007/BF00207767

Herman, R. G., Bogdan, C. E., Sommer, A. J., & Simpson, D. R. (1987). Discrimination among Carbonate Minerals by Raman Spectroscopy Using the Laser Microprobe. *Applied Spectroscopy*, 41(3), 437–440. https://doi.org/10.1366/0003702874448841

Hutsebaut, D., Vandenabeele, P., & Moens, L. (2005). Evaluation of an accurate calibration and spectral standardization procedure for Raman spectroscopy. *Analyst*, 130, 1204–1214. https://doi.org/10.1039/B503624K

Jimoh, O. A., Ariffin, K. S., & Hussin, H. B. (2018). Synthesis of precipitated calcium carbonate: a review. Carbonates and Evaporites, 33, 331–346. https://doi.org/10.1007/s13146-017-0341-x

Kim, Y., Caumon, M.-C., Barres, O., Sall, A., & Cauzid, J. (2021). Identification and composition of carbonate minerals of the calcite structure by Raman and infrared spectroscopies using portable devices. *Spectrochimica Acta Part A: Molecular and Biomolecular Spectroscopy*, 261, 119980. https://doi.org/10.1016/j.saa.2021.119980

Morita, M., Aoyama, T., Nakano, H., & Komatani, S. (2022). Practical Application of Elemental Imaging for Light Elements, Including Oxygen and Fluorine in Industrial Materials by Micro-EDXRF. *Advances in X-ray Chemical Analysis, Japan.*, 53,

139–149.

Morse, J. W. & Mackenzie, F. T. (2003). *Geochemistry of Sedimentary Carbonates* (1st ed.). Elsevier Science Publishers B.V., AE Amsterdam, The Netherlands.

Onoda, M., Nakano, H., Yamazaki, H., Tanaka, S., & Komatani, S. (2020). Analytical technique for high-accuracy FPM of trace powdered samples. *Advances in X-ray Chemical Analysis, Japan.*, 51, 65–79.

Petriglieri, J. R., Salvioli-Mariani, E., Mantovani, L., Tribaudino, M., Lottici, P. P., Laporte-Magoni, C., & Bersani, D. (2015). Micro-Raman mapping of the polymorphs of serpentine. Journal of Raman Spectroscopy, 46(10), 953–958. https://doi.org/10.1002/jrs.4695

Reeder, R. J. & Dollase, W. A. (1989). Structural variation in the dolomite-ankerite solid-solution series; an X-ray, Moessbauer, and TEM study. *American Mineralogist*, 74(9-10), 1159–1167.

Rividi, N., van Zuilen, M., Philippot, P., Ménez, B., Godard, G., & Poidatz, E. (2010). Calibration of Carbonate Composition Using Micro-Raman Analysis: Application to Planetary Surface Exploration. *Astrobiology*, 10(3), 293–309. https://doi.org/10.1089/ast.2009.0388

Rubey, W. W. (1951). GEOLOGIC HISTORY OF SEA WATER: AN ATTEMPT TO STATE THE PROBLEM. GSA Bulletin, 62(9), 1111–1148. https://doi.org/10.1130/0016-7606(1951)62[1111:GHOSW]2.0.CO;2

Rutt, H. N. & Nicola, J. H. (1974). Raman spectra of carbonates of calcite structure. *Journal of Physics C: Solid State Physics*, 7(24), 4522. https://doi.org/10.1088/0022-3719/7/24/015

Sherman, J. (1955). The theoretical derivation of fluorescent X-ray intensities from

mixtures. *Spectrochimica Acta*, 7, 283–306. https://doi.org/10.1016/0371-1951(55)80041-0

Shiraiwa, T. & Fujino, N. (1966). Theoretical Calculation of Fluorescent X-ray Intensities in Fluorescent X-ray spectrochemical Analysis. *Japanese Journal of Applied Physics*, 5, 886. https://doi.org/10.1002/xrs.1300130203

Spivak, A., Solopova, N., Cerantola, V., Bykova, E., Zakharchenko, E., Dubrovinsky, L., & Litvin, Y. (2014). Raman study of $MgCO_3$–$FeCO_3$ carbonate solid solution at high pressures up to 55 GPa. *Physics and Chemistry of Minerals*, 41, 633–638. https://doi.org/10.1007/s00269-014-0676-y

Tucker, M. & Wright, V. (2003). *Carbonate Sedimentology* (1st ed.). Blackwell Scientific Publications, Oxford.

Urashima, S. -H., Nishioka, T., & Yui, H. (2022). Micro-Raman spectroscopic analysis on natural carbonates: linear relations found via biaxial plotting of peak frequencies for cation substituted species. *Analytical Sciences*., 38, 921–929. https://doi.org/10.1007/s44211-022-00119-1

Warren, J. (2000). Dolomite: occurrence, evolution and economically important associations. *Earth-Science Reviews*, 52(1), 1–81. https://doi.org/10.1016/S0012-8252(00)00022-2

White, W. B. (1974). The Carbonate Minerals. In *The Infrared Spectra of Minerals.* Mineralogical Society of Great Britain and Ireland.

Chapter 5 Sample analysis of Asteroid Ryugu

5.1 Introduction

5.1.1 A mission goal of Hayabusa2 project

Although remote-sensing and laboratory-based technologies have been enriched over the decades, there are significant gaps in our understanding of the origin and evolution of the solar system. Meteorites are rare but valuable samples for researchers to address such scientific questions. They are considered fragments of asteroids, but their origins and parent asteroids are yet to be specified. Hence, state-of-the-art laboratory studies of directly returned samples by spacecraft will also be imperative (Anand et al., 2020). In December 2020, Japan Aerospace Exploration Agency (JAXA) launched the Hayabusa2 asteroid explorer, and it safely brought samples back to the Earth directly collected from the asteroid Ryugu (Wada et al., 2018; Tachibana et al., 2022; Yada et al., 2022). The near-Earth asteroid (162173) Ryugu was classified as a sub-class of C-type (carbonaceous) asteroid based on the studies of remote sensing (Yada et al., 2022), which indicates that there are or used to be the primary components of Life's origin: organic matter (carbon materials) and fluid water. The author belonging to the XRF team (in Chemistry Team, Initial Analysis Team, Hayabusa2 Project) was assigned to clarify abundances of elements and hydrated minerals like carbonates.

5.1.2 The sample and the proposed approach in the present research

In the previous chapters, the author has developed non-invasive and quantitative methods of chemical compositions of samples. "Non-invasive" is a procedure not involving irreversible alternations by physical or chemical processes in pre-treatments, such as surface polishing or metal/carbon coating. Briefly, it is a manner that keeps a sample intact. Yada et al. (2022) reported that samples from the asteroid Ryugu were aggregates

of fragile small particles. They are rough-surfaced, porous. The particles have small analytes (*e.g.,* minerals) sized sub-microns heterogeneously sparse in a millimeter-scaled sample matrix. The present study is an empirical investigation of an asteroid Ryugu sample having such sample characteristics to apply the proposed methods.

5.1.3 Micro-XRF

Micro-energy-dispersive X-ray fluorescence (micro-XRF) also allows us to visualize the heterogeneous spatial distribution of elements at a micro-meter scale without any pre-treatments (Tsuji et al., 2015). Its spatial resolution is typically less than 100 μm or minimally 10 μm in diameter when using glass poly-capillary focusing devices. However, XRF suffers from a critical drawback called the "matrix effect," when the size of analytes of interest is on the micrometer scale. The undesired signals from the matrix surrounding overlap the ones from the micrometer-sized analyte. Besides, relative to an electron or ion beam, X-ray photons penetrate further inside the analyte. Hence, when the analyte is thin, the detection area expands into the depth direction of the sample matrix. As a consequence, signals three-dimensionally overlap, thus declining quantitative accuracy in estimating elemental abundances in the aimed analyte. These problems, originating from both the instrumental limitations of micro-XRF and sample size and morphology, are called "matrix effects."

5.1.4 Raman micro-spectroscopy

Raman micro-spectroscopy is promising to overcome this difficulty. It provides information on even slight changes in molecular or crystal structures with superior lateral spatial resolution (usually 1 μm). Further, since the spectral patterns of Raman scattering derive from molecular or crystal structures, we can discriminate these analytes in the focused area. In other words, we can distinguish Raman signals of the aimed molecules

or crystals specifically from those of the matrix. However, Raman micro-spectroscopy also has disadvantages. One disadvantage is the difficulty of Raman spectroscopy alone in providing quantitative analysis with no references. In addition, it often prolongs measurement duration due to its inherently weak signal. In particular, this disadvantage could be severe when the analyte is rare and is heterogeneously and sparsely scattered on the surface of the specimen at a millimeter or even larger scale.

5.1.5 Special sample cell for the Ryugu samples (Chapter 3)

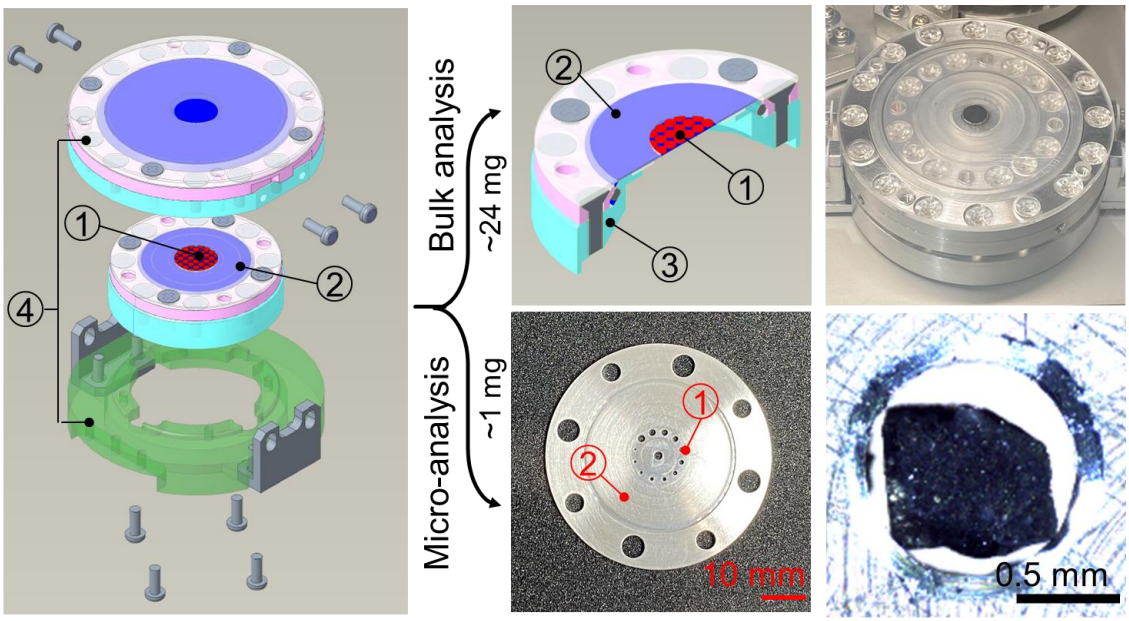

No.	Name	Bulk analysis	Micro-analysis
1	sample cell	single cell (6 mmφ)	multi-cell
2	cell frame	---	alminum
3	cell base	taper cut	
4	sample cell cover	for storage	

Figure 5.1 Special sample cells for the sample analysis of Asteroid Ryugu.

In bulk analysis, particles were pulverized into fine powder. On the other hand, small particles (< 1 mm) were prepared in micro-analysis. The author developed special sample cells for both analyses based on the design of sample cell introduced in Chapter 3 (Onoda

et al., 2020). Figure 5.1 summarizes the modifications. Firstly, the author changed the diameters of the cell. For the bulk analysis, the 6 mmϕ sample cell enabled the subsequent WDXRF to analyze approximately powders compacted 24 mg. In contrast, multiple cell diameters fit Ryugu particles, which is called Arrayed Multi-Chamber Cell (AMCC) for the micro-analysis. Secondly, we carefully chose the materials for the cell frame. For the bulk analysis, a cell frame made of acrylic resin instead of metal prevented undesired peaks. Conversely, a cell frame made of aluminum for micro-analysis ensured that the Ryugu particles were immobilized clear of electrostatic repulsion. Thirdly, the cell base was cut in taper. The tapered hollow below the cell is a space to attach jigs (attachments) during the compaction. The attachments were detached during laboratory-based and synchrotron-based XRF analyses to prevent undesired peaks. Fourthly, sample cell holders were prepared for storage and transport. Further details about the AMCC will be found in the next section.

5.1.6 Elemental abundances for bulk compositions (Chapter 2)

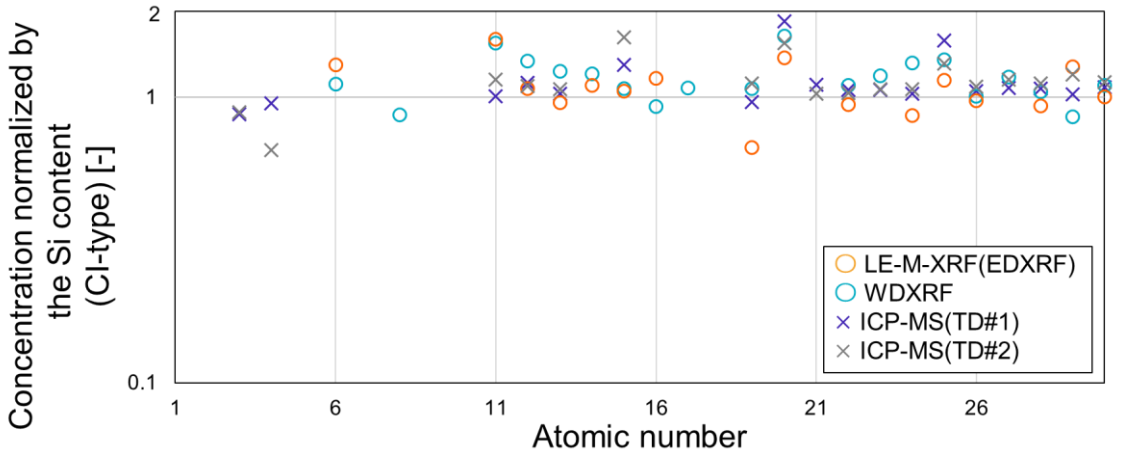

Figure 5.2 Elemental abundances of the Ryugu samples obtained by different analytical methods. TD#1: touchdown site 1, TD#2: touchdown site 2. The values are all normalized by the Si concentration of CI chondrite (carbonaceous chondrite Ivuna), which is a sub-class of C-type. Data are cited from (Yokoyama et al., 2023) and modified.

The classification of the asteroid Ryugu as a sub-class of C-type suggested that the samples consisted of phyllosilicate minerals and 2~3 % carbon. The author tried using light element micro-XRF (LE-M-XRF), described in Chapter 2 (Morita et al., 2022). However, the carbon content in Ryugu samples was nearly close to the lower limit of detection of carbon for LE-M-XRF, indicating difficulty quantifying carbon. Based on the knowledge in Chapter 2, the author created a calibration curve and compensated with matrix effects on the carbon peak in the present study (Yokoyama et al., 2023). Figure 5.2 shows the elemental abundances of the Ryugu samples compared with data by different techniques. The results by LE-M-XRF (EDXRF, HORIBA) were in good agreement with the ones by WDXRF and ICP-MS. The carbon abundance of 4.8 wt.% determined by WDXRF was consistent with the one by EDXRF. Since ICP-MS cannot analyze carbon, LE-M-XRF's carbon quantification enabled us to compare the data by WDXRF, even non-invasively. Consequently, the quantitative data for all elements were strongly supported by multiple methods. Detailed results will be provided in Table D2 (Appendix D).

5.1.7 Carbonates found in meteorites

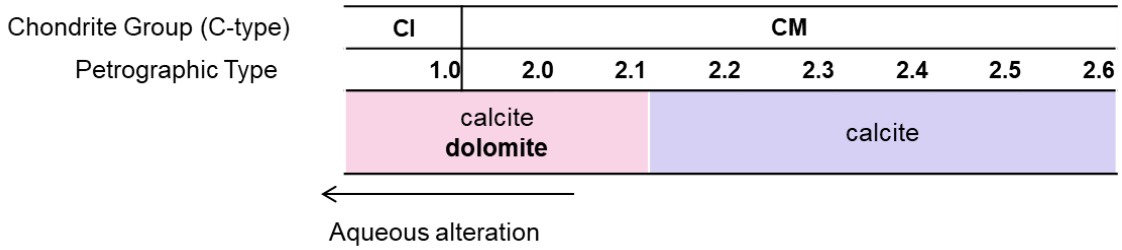

Figure 5.3 Carbonates found in chondrite groups with the scale of aqueous alternation. The figure is referred to (Weisberg et al., 2006; Rubin et al., 2007; Krot et al., 2015; Van Schmus & Wood, 1967) and modified for this thesis. CI: carbonaceous chondrite Ivuna, CM: carbonaceous chondrite Mighei.

The most primitive chondrites, specifically, CI or CM (carbonaceous chondrite Mighei) are rich in water and organic matter (Pizzarello et al., 2006; Alexander et al., 2007; Alexander et al., 2013). They experienced progressive aqueous alteration, and they had secondary minerals. Examples are phyllosilicates, magnetite, pyrrhotite, phosphates, and carbonates. As expected, observation of preliminary studies revealed that the Ryugu samples have various micrometer-scaled grains of minerals sparsely existing on the surface of the phyllosilicate matrix (Tachibana et al., 2022; Yokoyama et al., 2023). Figure 5.3 is a table of carbonates found in chondrite groups with the scale of aqueous alteration (Weisberg et al., 2006; Rubin et al., 2007; Krot et al., 2015; Van Schmus & Wood, 1967). The figure implies as the degree of aqueous alteration gets severer, calcite as well as dolomite dominates. Furthermore, the cation substitution of magnesium of dolomite with manganese or iron frequently occurred in CI or CM group meteorites, according to the previous studies (Endreß & Bischoff, 1996; Johnson & Prinz, 1993; Rubin et al., 2007). Hence, the cation compositions of carbonates provide beneficial information about the aqueous environments where they were created in the early solar system (Brearley, 2006; Fujiya et al., 2023).

However, a question about precedented studies has arisen: Are the cation compositions of dolomites the same before and after the sample pre-treatments and SEM-EDX analyses? The meteorites that underwent resin-embedding and surface-polishing pre-treatments may have slightly altered cation distributions on the surface. Charge-up may have damaged the samples and affected the accuracy of the quantification.

5.1.8 Conversion matrix for dolomite and Fe+Mn scale (Chapter 4)

Here, the author proposes a non-invasive and matrix effect-free analysis of cation compositions to analyze carbonate grains on an asteroid Ryugu sample in a simpler, more

precise way. In Chapter 4, the universal conversion matrix for carbonates was established. We then created a finer conversion for dolomite [$CaMg(CO_3)_2$]-ferroan dolomite [Ca(Mg, Fe)$(CO_3)_2$]-ankerite [$CaFe(CO_3)_2$] solid solution series (Reeder & Dollase, 1989; Chai & Navrotsky, 1996), using only three carbonates: dolomite, kutnohorite (SH) and kutnohorite (W). In these carbonate species, three cation abundances of Mg, Fe and Mn simultaneously vary. As shown in Figure 5.4, ferroan dolomite in the ternary diagram was inside a triangle with vertices of these three carbonates. The solution for this conversion is unique because the number of unknown parameters equals the number of fitting points. Consequently, the cation composition vector $\boldsymbol{x}'$ can be obtained as such:

$$\begin{pmatrix} x_{\mathrm{Ca}} \\ x_{\mathrm{Mg}} \\ x_{\mathrm{Fe}} + x_{\mathrm{Mn}} \end{pmatrix} = \begin{pmatrix} -0.03155 & 0.02768 & -2.13220 \\ -0.00021 & 0.03186 & -9.04692 \\ 0.03176 & -0.05953 & 12.17912 \end{pmatrix} \begin{pmatrix} \widetilde{\nu_{\mathrm{T}}} \\ \widetilde{\nu_{\mathrm{L}}} \\ 1 \end{pmatrix} \tag{5.1}$$

Further discussions will be described in Appendix D.1.

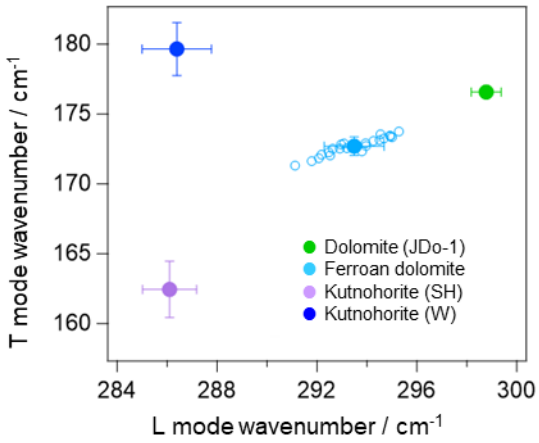

Figure 5.4 T-L biaxial map of the dolomite group.

Moreover, we established a calibration curve of Fe+Mn content for dolomite (Morita et al., 2023). We studied terrestrial dolomites and investigated their Fe+Mn contents from XRF and Raman spectra. Figure 5.5 shows the relation between the Fe+Mn content and

L mode wavenumber. Here, one can easily see that the peak wavenumber and the cation content correlated in a linear manner. In fact, the coefficient of determination (R^2) indicating linearity was 0.961. Besides, the L mode wavenumber shifted more remarkably depending on the Fe+Mn content than the T mode.

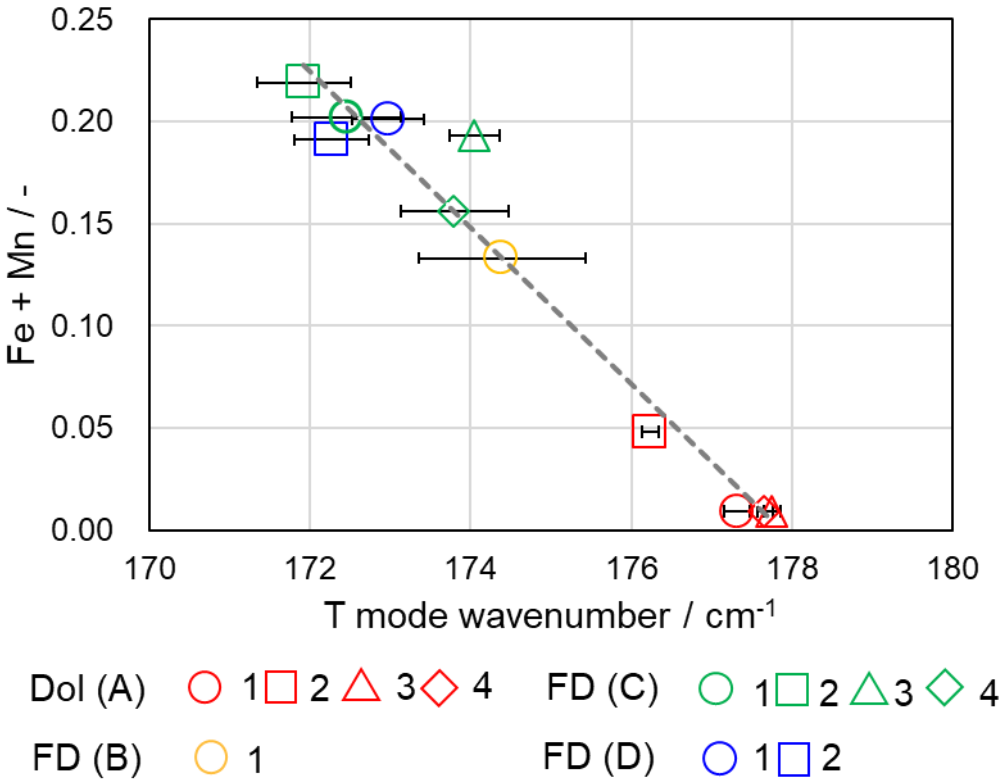

Figure 5.5 Fe+Mn scale for the dolomite group established by using L mode wavenumbers. Dol: dolomite, FD: ferroan dolomite.

Based on the linear fitting, the Fe+Mn content, namely, $\boldsymbol{x_{Fe+Mn}}$ is given as:

$$x_{\mathrm{Fe+Mn}} = -0.02273\widetilde{\nu_{\mathrm{L}}} + 6.836 \qquad (5.2)$$

where $\widetilde{\nu_{\mathrm{L}}}$ is the peak wavenumber of the L mode in cm^{-1}. The root-mean-squared-error of the composition for this equation was 1.7%, indicating a highly accurate estimation. The Fe+Mn content of the samples analyzed ranged from 0.9 and 22 atom%. Hence, this calibration curve is no longer applicable if the analyte extrapolates; in other words, when the analyte is Fe or Mn richer than this range, and the resulting L mode wavenumber is

lower than ~290 cm^{-1}. Experiments and the results of the T mode wavenumber will be described in Appendix D.2-D.3.

5.1.9 The main focus of the current chapter

In the previous subsection, a non-invasive and matrix effect-free analysis of cation compositions was finally proposed. The proposed approach not only identifies carbonate species of that sample but also quantitatively evaluates the degree of Fe+Mn substitution of dolomites using peak shifts of Raman frequencies (Urashima et al., 2022, 2023; Morita et al., 2023). Notably, the quantitative accuracy of the developed method is sufficiently reliable to reveal marginal differences in Fe+Mn abundance at various micrometer-scaled spots measured even within a single chip (Morita et al., 2023). In the current chapter, the author explored the asteroid Ryugu sample taking advantage of the AMCC and the proposed method.

5.2 Experiments

5.2.1 Elemental imaging by micro-XRF

Micro-XRF was performed at HORIBA X-RAY LAB with ver. 1.3.2.19 software (XGT-9000, HORIBA, Ltd.) (Morita et al., 2023). The beam diameter of primary X-rays was 100 μm. Elemental imaging was carried out within the entire area of the Ryugu particle. The measurement conditions of the X-ray tube voltage, the measurement time, and the X-ray working distance were 30 kV, 200 ms per pixel, and 1.0 mm, respectively. The tube current was set to be 300 μA. For elemental imaging, the step size was 14 μm. During the measurements, chambers were kept in "Whole Vacuum" mode under vacuumed conditions.

5.2.2 Raman micro-spectroscopy

Micro Raman measurements were conducted with LabRAM HR Evolution (Figure 5.6) and LabSpec 6 software (HORIBA, Ltd.). Synapse EMCCD camera (HORIBA, Ltd.) was installed for a detector. The confocal optical arrangement of the microscope and auto-focusing stage-driving with the software enabled us to obtain Raman spectra with a superior spatial resolution even from rough-surfaced samples without any pre-treatments such as surface polishing. An objective lens as Olympus LMPlanFN (x100, NA 0.80, WD 3.4 mm) was used for Raman imaging at micro-meter resolution. Excitation wavelength and power were 532 nm and 0.6-1.2 mW, respectively. The spectra were measured for 120 s of exposure and averaged twice. Raman signals from a Si wafer (520.6 cm^{-1}) and a sulfur flake (153.8, 219.1, and 473.2 cm^{-1}) were used to calibrate Raman shifts.

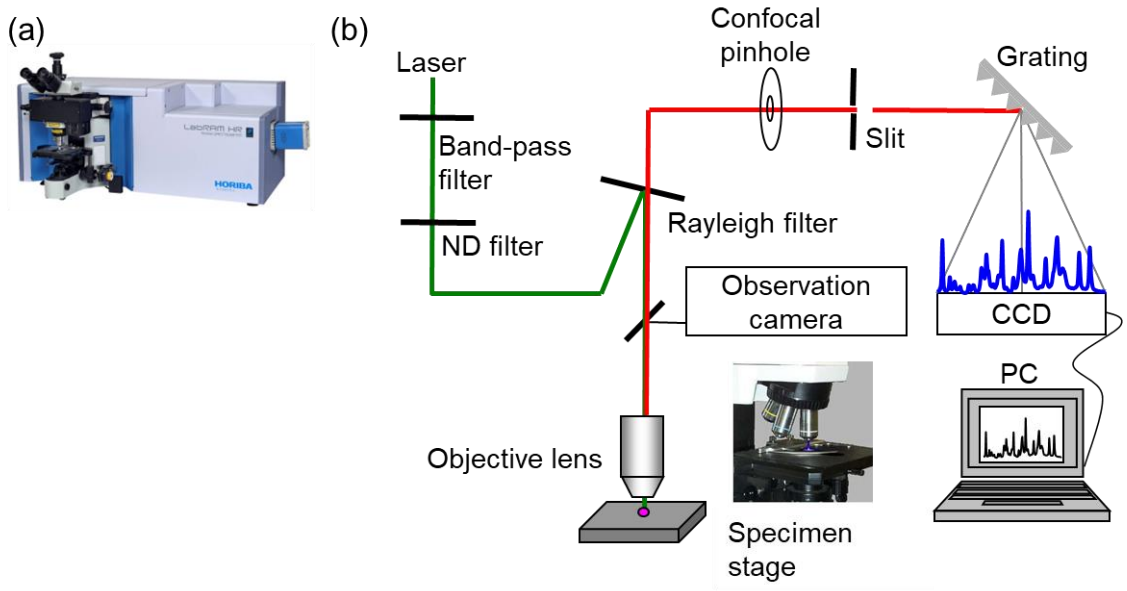

Figure 5.6 Exterior photograph (a) and schematic illustration of the optical configuration (b) of Raman microscope LabRAM HR Evolution. An Olympus objective lens (x100, NA 0.80, WD 3.4 mm) was used. The wavelength of excitation laser and the power were 532 nm and 0.6-1.2 mW. The acquisition time was 120s and the spectra were averaged by two measurements. Raman signals were calibrated by a piece of Si wafer and sulfur at 520.6 cm^{-1}(Si), 153.8, 219.1, and 473.2 cm^{-1} (S).

5.2.3 Estimating cation composition for the ternary diagram

When determining the cation compositions for terrestrial carbonates, we applied the standard Fundamental Parameter (FP) Method (Sherman, 1955; Shiraiwa & Fujino, 1966) to XRF spectra. The cation compositions were calibrated by standard samples named JLk-1 and dolomite (MV) for kutnohorites (Urashima et al., 2022) the dolomite, respectively. This calibration works to calibrate fundamental parameters stored in the instrumentation; for example, coefficients for elemental intensity are firmly subject to matrix effects. JLk-1 is a geo standard of lake sediment from Lake Biwa, Shiga, Japan, provided by The National Institute of Advanced Industrial Science and Technology, Japan. The dolomite (MV) is a dolomite stone mined at Morro Velho, Brazil. For using a single crystal (0.1697 g) of dolomite (MV) as the standard, its cation composition was obtained by inductively coupled plasma atomic emission spectroscopy (ICP-AES). The details of the ICP-AES experiment can be found in Appendix D.3. Finally, each cation content was simply given by the formula (5.3) below.

$$C_{\mathrm{ion}} = \frac{W_{\mathrm{ion}}}{\frac{W_{\mathrm{Mg}}}{M_{Mg}} + \frac{W_{\mathrm{Ca}}}{M_{Ca}} + \frac{W_{\mathrm{Mn}}}{M_{Mn}} + \frac{W_{\mathrm{Fe}}}{M_{Fe}}} \qquad (ion = Mg, Ca, Mn, and\ Fe) \qquad (5.3)$$

C_{ion}: cation content [atom%], W_{ion}: element concentration [wt. %], M_{ion}: atomic weight.

5.2.4 Arrayed Multi-Chamber Sample Cell (AMCC)

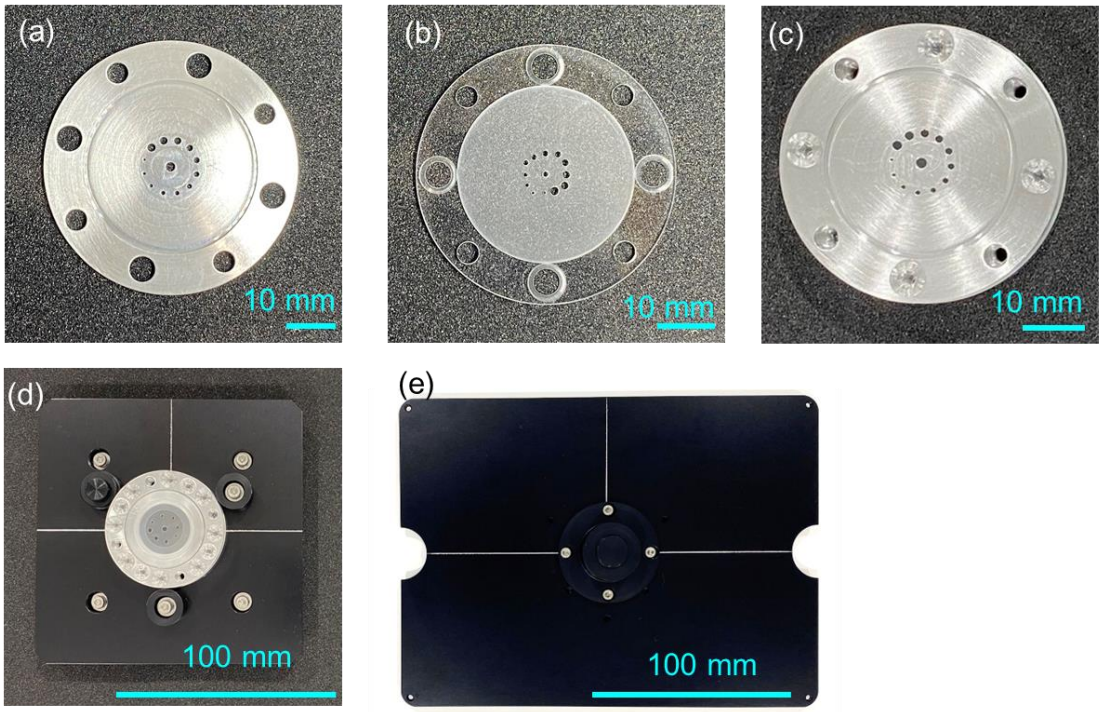

Figure 5.7 Images of Arrayed Multi-Chamber Sample Cell (AMCC). Different cell frames were used for (a) the Ryugu samples and (b) the references. (c) Aluminum cell frame built with an aluminum cell base. AMCC can be attached to jigs for (d) micro-XRF and (e) Raman microscope.

To sequentially implement experiments with two different microscopes, we have developed a sample holder called Arrayed Multi-Chamber Sample Cell (AMCC). We drilled holes 0.5 mm deep with diameters ranging from 0.5 to 1.2 mm at 0.1 mm pitch (Figure 5.7(a), (b), (c)). When loading the sample(s), we carefully chose a hole that would fit the size of Ryugu particles. The Ryugu particles are so small and light that they might quickly sprinkle into the instrument chambers because of static electricity or air flowing upon either vacuuming or atmospheric release. When the AMCC was placed on the specimen stage of the respective microscope, AMCC jigs were used (Figure 5.7(d), (e)). In the micro-XRF measurement, the pressure in the sample chamber was kept below tens

of Pa. When transferring the AMCC from micro-XRF to the Raman microscope, the pressure in the sample chamber was gradually released to atmospheric pressure. When the sample is tiny, as small as or less than 1 mg, it is likely to unfit the holes due to static electricity. Therefore, a 0.5 mm-thick aluminum cell frame was set to load a single Ryugu particle into a hole with an appropriate diameter. On the other hand, acrylic cell frames were used to fix reference minerals, all large enough not to worry about the risk of sample loss.

5.2.5 Samples

A Ryugu particle picked up from A0107 aggregate sample collected at the first touchdown site (TD1) was measured in this study (Yada et al., 2022; Tachibana et al., 2022). For reference, the geo standard and terrestrial carbonates were analyzed, and whose mined locations were summarized as follows. JLk-1 is from Lake Biwa, Shiga, Japan. Calcite is from Garo, Hokkaido, Japan. Magnesite is from Goat Hill Magnesia Quarries, Pennsylvania, USA. Kutnohorite (SH) is from Sterling Mine, New Jersey, USA. Kutnohorite (W) is from Wissels Mine, Northern Cape, South Africa. Dolomite (MV) is from Morro Velho Mine, Minas Gerais, Brazil. Ferroan dolomite (EM) is from Eagle Mine, Colorado, USA. Their optical images are shown in Figure D.8.

5.3 Results and Discussions

5.3.1 Mn-Ca colocalization on the Ryugu particle

Figure 5.8 shows the Ryugu particle (from A0107) analyzed. Mg and Fe are predominantly present; in contrast, Ca and Mn are sparse and heterogeneous. Notably, the bright spots of Mn corresponded with those of Ca. According to previous studies (Endreß & Bischoff, 1996; Johnson & Prinz, 1993; Rubin et al., 2007), this spatial matching of

the two elements strongly suggests that carbonate grains exist at these spots. Hence, elemental imaging for Ca and Mn helps us find the locations of carbonate grains on the sample matrix. Naturally, carbonate species are identified by the four major cations: Ca, Mg, Fe, and Mn. Because Mg and Fe are also abundant in the Ryugu sample matrix of phyllosilicate minerals, it is challenging to specify carbonate species only based on Ca and Mn distribution. In Figure 5.8, it should also be noted that the brightness of the two elements differs depending on the locations. This result implies that it represents the difference in the cation composition of each carbonate grain at the Ca-Mn colocalization sites. However, we must remark on the possibility that this brightness variation derives from matrix effects. The matrix effects make it difficult to estimate their cation compositions in such a heterogeneous sample merely through micro-XRF.

5.3.2 Raman spectra measured at Ca-Mn rich spots

To ensure whether carbonate grains exist, we measured Raman spectra at the Ca-Mn colocalization spots shown in the upper panel of Figure 5.9. It should be noted that AMCC achieved probing identical places between micro-XRF and Raman microscopes. In the figure, three or four sharp peaks were present in the Raman spectra with a broad fluorescence background at all measured colocalization spots. The peak wavenumbers for these bands were around 174, 295, 724, and 1094 cm^{-1}, as summarized in Table 5.1. These bands are specific to carbonates, and each peak is assigned to translational lattice mode (T), librational lattice mode (L), CO_3^{2-} bending mode (ν_4), and CO_3^{2-} stretching mode (ν_1), respectively (White, 1974; Couture, 1947). Here, the appearance of these bands bears out that there are indeed carbonate grains at all of the Ca-Mn colocalization spots. Based on previous works (Urashima et al., 2022, 2023; Morita et al., 2023) reporting that the peak wavenumbers shift depending on the cation compositions in carbonates, we compared

them with those previously obtained, and it turned out that these carbonates were essentially assigned to dolomite [$CaMg(CO_3)_2$]. Remarkably, Mg in dolomite is often partially substituted by Fe or Mn, thus consequently forming dolomite [$CaMg(CO_3)_2$] – ankerite [$CaFe(CO_3)_2$] – kutnohorite [$CaMn(CO_3)_2$] solid solution series (Reeder & Dollase, 1989; Chai & Navrotsky, 1996). Indeed, the peak wavenumbers, as summarized in Table 5.1, slightly deviated from each other, which implies various degrees of cation substitution that occurred at an individual carbonate grain. This point is discussed in detail from a quantitative point of view in the following section.

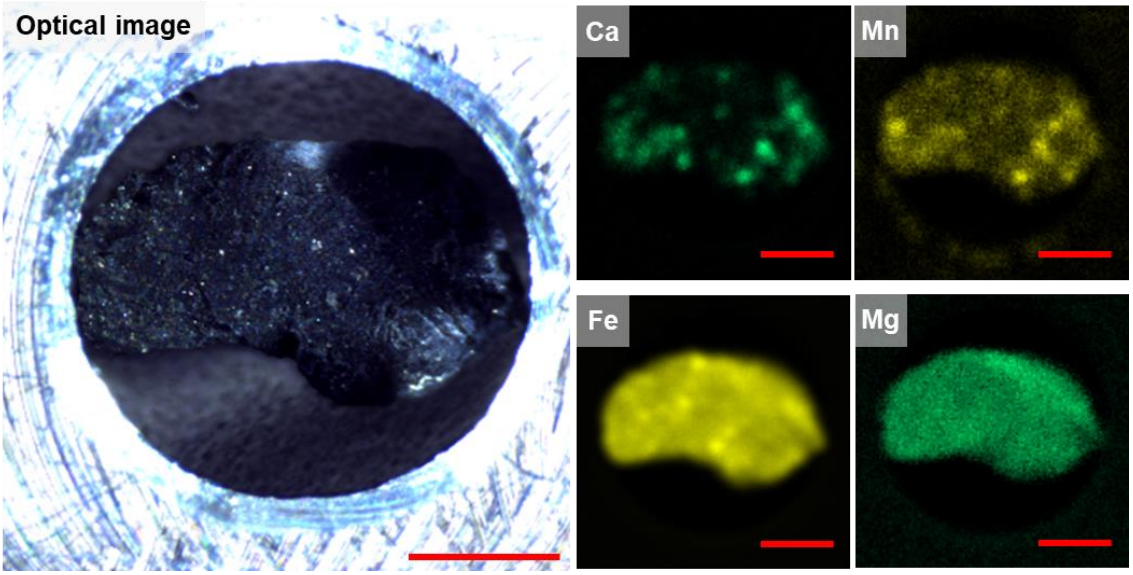

Figure 5.8 The optical image of Ryugu particle in AMCC (left) and the corresponding element images of Ca, Mn, Fe, and Mg (four panels on the right). Scale bars are 0.5 mm.

Table 5.1 List of Raman frequencies for Ryugu carbonate grains and terrestrial references (unit: cm^{-1}).

	T	L	ν_4	ν_1
A(a)	176.4	298.9	724.9	1096.8
A(b)	173.7	296.0	721.7	1094.8
A(c)	171.6	289.7	722.3	1095.0
B	173.8	295.0	-	1095.3
C	175.0	296.1	-	1095.6
D	175.1	296.3	-	1095.0
E	175.0	294.6	-	1094.6
F	174.5	296.1	-	1094.7
Calcite	154.6 ± 0.9	280.9 ± 0.9	711.6 ± 0.8	1086.0 ± 0.8
Magnesite	212.5 ± 1.0	329.3 ± 1.0	738.2 ± 1.1	1094.4 ± 1.0
Dolomite (MV)	174.1 ± 0.2	296.7 ± 0.2	724.3 ± 0.1	1096.8 ± 0.2

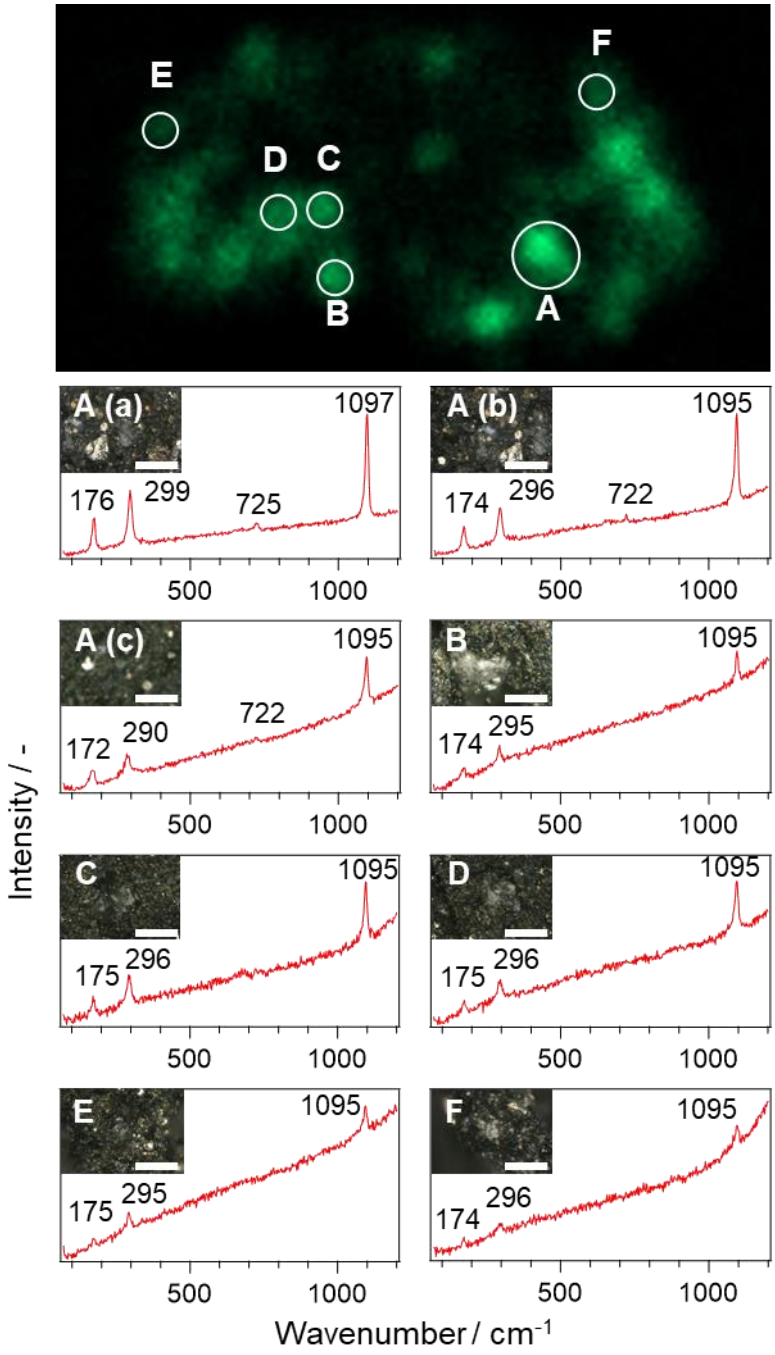

Figure 5.9 Ca bright spots on the surface of the Ryugu particle by micro-XRF imaging and their corresponding Raman spectra. The inset in each spectrum is the corresponding optical image. Scale bars are 20 μm. The grayish grains on the black matrices are carbonates.

5.3.3 Estimation of Fe + Mn content in Ryugu dolomites

Earlier, the results from both micro-XRF and Raman micro-spectroscopy suggested the partial substitution of Mg for Fe or Mn. Yet, the fact that Mg and Fe are present everywhere in the matrix makes it difficult for only micro-XRF to determine the cation compositions of carbonates selectively. However, we found that the cation composition of carbonates can be uniquely determined from their Raman frequencies of T and L modes within an error of 1.7 % (Urashima et al., 2022, 2023). Although a couple of conversion equations were proposed in the previous studies (Urashima et al., 2022, 2023; Morita et al., 2023), the first thing to do is qualitatively specify the type of carbonates, including major cations contained to choose the most suitable one.

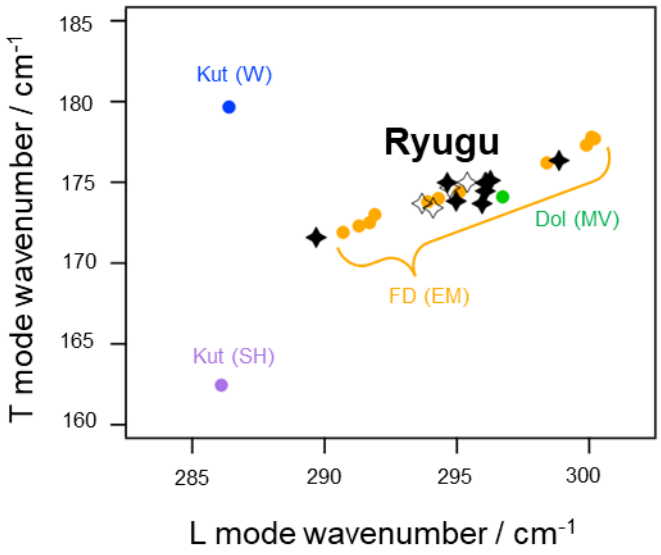

Figure 5.10 Biaxial plotting of Ryugu dolomites in comparison with terrestrial dolomites in T- and L- mode wavenumbers. For Ryugu dolomites, the black filled markers represent those obtained at the grains A(a) to F. In contrast, the open markers represent those obtained at different spots within the grain B. Dol: dolomite, FD: ferroan dolomite, Kut: kutnohorite.

To discuss this regard more, we biaxially plotted the T and L mode frequencies of Ryugu carbonates along with the plots of terrestrial carbonates, which are classified into the dolomite-ankerite-kutnohorite solid solution series (Figure 5.10). Specifically, two

kurnohorites named (SH) and (W) are shown, which were collected at Sterling Hills (USA) and Wissels Mine (South Africa), respectively. Notably, their cation compositions are significantly distinct. Also, plots of terrestrial ferroan dolomite (Eagle Mine (EM), USA; data taken from (Morita et al., 2023) widely spread in the T and L mode frequencies. The reason for the widespread plotting is the heterogeneity of cation composition in a sample. Figure D.9 (Appendix D) presents their XRF spectra, and Table D.3 summarizes the cation compositions of the terrestrial carbonates. Herewith, more precisely, we can assign Ryugu dolomites to ferroan dolomite. Note that their wavenumbers, slightly contingent on the measurement positions, reflect their intra- and inter-crystal heterogeneity.

The cation composition of ferroan dolomites can be obtained by the T and L mode wavenumbers as already reported in our previous studies (Urashima et al., 2022, 2023; Morita et al., 2023). The $C_{\mathrm{Fe+Mn}}$ content is expressed by Eq. (5.2) (Morita et al., 2023). To determine C_{Ca}, we revised the previous equation Eq. (5.1) ($C_{\mathrm{Ca}} = -0.03155\widetilde{\nu_{\mathrm{T}}} + 0.02768\widetilde{\nu_{\mathrm{L}}} - 2.13220$) (Urashima et al., 2023),

$$C_{\mathrm{Ca}} = -0.03139\widetilde{\nu_{\mathrm{T}}} + 0.01867\widetilde{\nu_{\mathrm{L}}} + 0.419 \qquad (5.4)$$

where $\widetilde{\nu_{\mathrm{T}}}$ is the T mode wavenumber in cm^{-1}. This revision is because the Ca content in the standard sample named JDo-1 was overestimated. While the coefficients of Eq. (5.4) were derived in the same way as that in the previous study (Urashima et al., 2023), a more reliable standard than the dolostone JDo-1, a dolomite crystal (Morro Velho Mine, Brazil) was employed here. Further information about the derivation of Eq. (5.4) can be found in Appendix D.4. Note that this revision can solve the overestimation issue by reducing the Ca content by 10 atom% from what was originally calculated. Given C_{Ca} and $C_{\mathrm{Fe+Mn}}$, C_{Mg} can be naturally determined from Eqs. (5.3), namely, $C_{\mathrm{Ca}} + C_{\mathrm{Mg}} +$

$C_{\mathrm{Fe+Mn}} = 1$.

Figure 5.11 is a ternary diagram showing plots of the cation compositions for Ryugu dolomites derived by Eqs. (5.2) – (5.4). The figure indicates that the majority of Ryugu dolomites included about 10-15% of Fe or Mn. Relative to a recent study reporting that a ternary diagram (Ca, Mg, Fe+Mn) of Ryugu dolomites with SEM-EDX measurements showed on average 10~20% of $C_{\mathrm{Fe+Mn}}$ (Nakamura et al., 2023; Nakato et al., 2022), the distribution in this analysis is consistent with the previous one. This consistency has proven that the quantitative data provided by conventional analytical methods and the proposed one are both significantly reliable. Notably, it does not require pre-treatments of samples as surface polishing. Moreover, it does not induce any risks or concerns about charge-up and matrix effects.

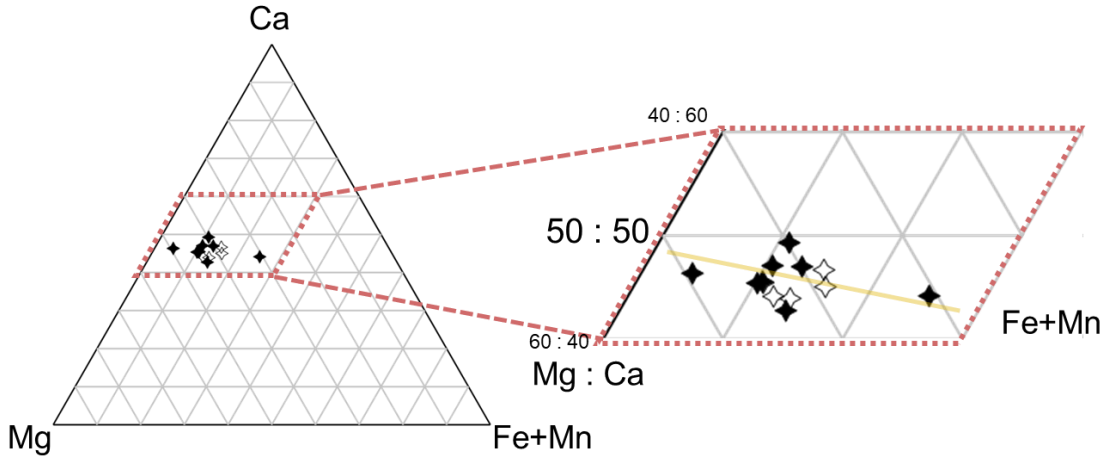

Figure 5.11 Cation compositions for Ryugu dolomites. Cation composition of Ryugu dolomites plotted on a ternary diagram. The black and white markers represent those obtained at the Spot A(a) to F and those within the Spot (B). A yellow line guides the direction of Fe+Mn.

From an analytical point of view, the proposed method has two advantages worth noting. One is that the elemental imaging of micro-XRF facilitates searching sparsely distributed carbonates without pre-treatments. The other is that the analyte-selective

nature and the cation-dependent shifts of wavenumbers in Raman micro-spectroscopy make it possible to quantify individual cation composition and its heterogeneity in the exact carbonate grain. Specifically, we measured Raman spectra at a few different spots within the Spot B (Figure D.11), and we found out the cation compositions were heterogeneous even inside a single dolomite grain (Figure 5.10, Figure 5.11). The proposed method would provide an initial analysis tool for evaluating the micro-heterogeneity of rare and pristine samples with surface roughness but without any pre-treatments.

5.4 Summary

This chapter briefly introduced the mission goal of Hayabusa2 project and the aim of the present research. The author was assigned to this project to clarify the elemental abundances and minerals contained non-invasively. Before analyzing Ryugu samples, we improved the techniques developed in previous chapters. The special sample cells helped us not only load powder and particles of the Ryugu sample but also locate identical carbonate grains, even though we used different microscopes. LE-M-XRF contributed to the non-invasive determination of carbon content in comparison with the data by WDXRF. Because the asteroid Ryugu was assumed to have experienced aqueous alteration severely, cation substitution of Mg to Fe+Mn in dolomite would be predominantly found. The conversion matrix to evaluate cation contents was improved from Chapter 4 and a non-invasive scale of Fe+Mn was prepared.

Micro-XRF elemental imaging rapidly found carbonate grains, and it turned out that they were essentially dolomite from wavenumbers of T and L modes. Their Fe+Mn abundances were quantified by the proposed approach, and they were in good accordance

with the ones reported in the precedented research, with an average of 10~15% Fe+Mn content. For a viewpoint of analytical chemistry, it is a noteworthy achievement that the proposed method can quantitatively characterize the heterogeneity of cation composition both between and inside Ryugu dolomite grains sized several micrometers with the surface morphology intact in a matrix-free manner.

5.5 Bibliography

Alexander, C. M. O'D., Howard, K. T., Bowden, R., & Fogel, M. L. (2013). The classification of CM and CR chondrites using bulk H, C and N abundances and isotopic compositions. *Geochimica et Cosmochimica Acta*, 123, 244–260. https://doi.org/10.1016/j.gca.2013.05.019

Alexander, C. M. O'D., Fogel, M., Yabuta, H., & Cody, G. D. (2007). The origin and evolution of chondrites recorded in the elemental and isotopic compositions of their macromolecular organic matter. *Geochimica et Cosmochimica Acta*, 71(17), 4380–4403. https://ui.adsabs.harvard.edu/link_gateway/2007GeCoA..71.4380A/doi:10.1016/j.gca.2007.06.052

Anand, M., Russell, S., Lin, Y., Wadhwa, M., Marhas, K. K., & Tachibana, S. (2020). Editorial to the topical collection: Role of Sample Return in Addressing Major Questions in Planetary Sciences. *Space Science Reviews*, 216(5). https://doi.org/10.1007/s11214-020-00724-4

Brearley, A. J. (2006). The Action of Water. In Lauretta, D. S. & McSween, H. Y. (Eds.), *Meteorites and the Early Solar System II* (pp. 587-624). University of Arizona Press, USA.

Chai, L. & Navrotsky, A. (1996). Synthesis, characterization, and energetics of solid solution along the dolomite-ankerite join, and implications for the stability of ordered $CaFe(CO_3)_2$. *American Mineralogist*, 81(9-10), 1141–1147. https://doi.org/10.2138/am-1996-9-1012

Couture, L. (1947). Étude des spectres de vibrations de monocristaux ioniques. *Annales de Physique*, 12(2), 5–94.

Endreß, M. & Bischoff, A. (1996). Carbonates in CI chondrites: clues to parent body evolution. *Geochimica et Cosmochimica Acta*, 60(3), 489–507. https://doi.org/10.1016/0016-7037(95)00399-1

Fujiya, W., Kawasaki, N., Nagashima, K., Sakamoto, N., Alexander, C. M. O'D., Kita, N. T., Kitajima, K., Abe, Y., Aléon, J., Amari, S., Amelin, Y., Bajo, K.-I., Bizzarro, M., Bouvier, A., Carlson, R. W., Chaussidon, M., Choi, B.-G., Dauphas, N., Davis, A. M., …Yurimoto, H. (2023). Carbonate record of temporal change in oxygen fugacity and gaseous species in asteroid Ryugu. *Nature Geoscience*, 16, 675-682. https://doi.org/10.1038/s41561-023-01226-y

Johnson, C. A., & Prinz, M. (1993). Carbonate compositions in CM and CI chondrites and implications for aqueous alteration. *Geochimica et Cosmochimica Acta.*, 57(12), 2843–2852. https://doi.org/10.1016/0016-7037(93)90393-B

Krot, A., Nagashima, K., Alexander, C. M. O'D., Ciesla, F., Fujiya, W., & Bonal, L. (2015). Sources of Water and Aqueous Activity on the Chondrite Parent Asteroids. In Patrick Michel, F. E. D. & Bottke, W. F. (Eds.), *Asteroids IV* (pp. 635–660). University of Arizona Press, Tucson.

Morita, M., Aoyama, T., Nakano, H., & Komatani, S. (2022). Practical Application of Elemental Imaging for Light Elements, Including Oxygen and Fluorine in Industrial

Materials by Micro-EDXRF. *Advances in X-ray Chemical Analysis, Japan.*, 53, 139–149.

Morita, M., Urashima, S.-H., Tsuchiya, H., Komatani, S., & Yui, H. (2023). New analytical method for the evaluation of heterogeneity in cation compositions of dolomites by micro-XRF and Raman spectroscopies. *Analytical Sciences*, 39, 1279-1295. https://doi.org/10.1007/s44211-023-00333-5

Morita, M., Yui, H., Urashima, S.-H., Onose, M., Komatani, S., Nakai, I., Abe, Y., Terada, Y., Homma, H., Motomura, K., Ichida, K., Yokoyama, T., Nagashima, K., Aléon, J., Alexander, C. M. O'D., Amari, S., Amelin, Y., Bajo, K.-I., Bizzarro, …Yurimoto, H. (2024). Analysis of Cation Composition in Dolomites on the Intact Particles Sampled from Asteroid Ryugu. *Analytical Chemistry*, 96(1), 170–178. https://doi.org/10.1021/acs.analchem.3c03463

Morse, J. W. & Mackenzie, F. T. (2003). *Geochemistry of Sedimentary Carbonates* (1st ed.). Elsevier Science Publishers B.V., AE Amsterdam, The Netherlands.

Nakamura, T., Matsumoto, M., Amano, K., Enokido, Y., Zolensky, M. E., Mikouchi, T., Genda, H., Tanaka, S., Zolotov, M. Y., Kurosawa, K., Wakita, S., Hyodo, R., Nagano, H., Nakashima, D., Takahashi, Y., Fujioka, Y., Kikuiri, M., Kagawa, E., Matsuoka, M., …Tsuda, Y. (2023). Formation and evolution of carbonaceous asteroid Ryugu: Direct evidence from returned samples. *Science*, 379(6634), eabn8671. https://doi.org/10.1126/science.abn8671

Nakato, A., Inada, S., Furuya, S., Nishimura, M., Yada, T., Abe, M., Usui, T., Yoshida, H., Mikouchi, T., Sakamoto, K., Yano, H., Miura, Y. N., Takano, Y., Yamanouchi, S., Sawada, H., & Tachibana, S. (2022). Ryugu particles found outside the Hayabusa2 sample container. *Geochemical Journal*, 56(6), 197–222. https://doi.org/10.2343/geochemj.GJ22017

Onoda, M., Nakano, H., Yamazaki, H., Tanaka, S., & Komatani, S. (2020). Analytical technique for high-accuracy FPM of trace powdered samples. *Advances in X-ray Chemical Analysis, Japan.*, 51, 65–79.

Pizzarello, S., Cooper, G., & Flynn, G. (2006). The Nature and Distribution of the Organic Material in Carbonaceous Chondrites and Interplanetary Dust Particles. In Lauretta, D. S. and McSween, H. Y. (Eds), *Meteorites and the Early Solar System II*, pages 625–651.

Reeder, R. J. & Dollase, W. A. (1989). Structural variation in the dolomite-ankerite solid-solution series; an X-ray, Moessbauer, and TEM study. *American Mineralogist*, 74(9-10), 1159–1167.

Rubin, A. E., Trigo-Rodríguez, J. M., Huber, H., and Wasson, J. T. (2007). Progressive aqueous alteration of CM carbonaceous chondrites. *Geochimica et Cosmochimica Acta*., 71(9), 2361–2382. https://doi.org/10.1016/j.gca.2007.02.008

Sherman, J. (1955). The theoretical derivation of fluorescent X-ray intensities from mixtures. *Spectrochimica Acta*, 7, 283–306. https://doi.org/10.1016/0371-1951(55)80041-0

Shiraiwa, T. & Fujino, N. (1966). Theoretical Calculation of Fluorescent X-ray Intensities in Fluorescent X-ray spectrochemical Analysis. *Japanese Journal of Applied Physics*, 5, 886. https://doi.org/10.1002/xrs.1300130203

Tachibana, S., Sawada, H., Okazaki, R., Takano, Y., Sakamoto, K., Miura, Y. N., Okamoto, C., Yano, H., Yamanouchi, S., Michel, P., Zhang, Y., Schwartz, S., Thuillet, F., Yurimoto, H., Nakamura, T., Noguchi, T., Yabuta, H., Naraoka, H., Tsuchiyama, A., …Tsuda, Y. (2022). Pebbles and sand on asteroid (162173) Ryugu: In situ observation and particles returned to Earth. *Science*, 375(6584), 1011–1016.

https://doi.org/10.1126/science.abj8624

Tsuji, K., Matsuno, T., Takimoto, Y., Yamanashi, M., Kometani, N., Sasaki, Y. C., Hasegawa, T., Kato, S., Yamada, T., Shoji, T., & Kawahara, N. (2015). New developments of X-ray fluorescence imaging techniques in laboratory. *Spectrochimica Acta Part B: Atomic Spectroscopy*, 113, 43–53. https://doi.org/10.1016/j.sab.2015.09.001

Urashima, S. -H., Nishioka, T., & Yui, H. (2022). Micro-Raman spectroscopic analysis on natural carbonates: linear relations found via biaxial plotting of peak frequencies for cation substituted species. *Analytical Sciences*., 38, 921–929. https://doi.org/10.1007/s44211-022-00119-1

Urashima, S.-H., Morita, M., Komatani, S., & Yui, H. (2023). Non-destructive estimation of the cation composition of natural carbonates by micro-Raman spectroscopy. *Analytica Chimica Acta*, 1242, 340798. https://doi.org/10.1016/j.aca.2023.340798

Van Schmus, W. R. & Wood, J. A. (1967). A chemical-petrologic classification for the chondritic meteorites. *Geochimica et Cosmochimica Acta*, 31(5), 747–765. https://ui.adsabs.harvard.edu/link_gateway/1967GeCoA..31..747V/doi:10.1016/S0016-7037(67)80030-9

Wada, K., Grott, M., Michel, P., Walsh, K. J., Barucci, A. M., Biele, J., Blum, J., Ernst, C. M., Grundmann, J. T., Gundlach, B., Hagermann, A., Hamm, M., Jutzi, M., Kim, M.-J., Kührt, E., Le Corre, L., Libourel, G., Lichtenheldt, R., Maturilli, A., …International Regolith Science Group (IRSG) in Hayabusa2 project (2018). Asteroid Ryugu before the Hayabusa2 encounter. *Progress in Earth and Planetary Science*, 5(1), 82. https://doi.org/10.1186/s40645-018-0237-y

Weisberg, M.K., McCoy, T. & Krot, A. (2006). Systematics and evaluation of meteorite

classification. In Lauretta, D. S. & McSween, H. Y. (Eds.), *Meteorites and the Early Solar System II* (pp. 19–52). University of Arizona Press, USA

White, W. B. (1974). The Carbonate Minerals. In *The Infrared Spectra of Minerals.* Mineralogical Society of Great Britain and Ireland.

Yada, T., Abe, M., Okada, T., Nakato, A., Yogata, K., Miyazaki, A., Hatakeda, K., Kumagai, K., Nishimura, M., Hitomi, Y., Soejima, H., Yoshitake, M., Iwamae, A., Furuya, S., Uesugi, M., Karouji, Y., Usui, T., Hayashi, T., Yamamoto, D., …Tsuda, Y. (2022). Preliminary analysis of the Hayabusa2 samples returned from C-type asteroid Ryugu. *Nature Astronomy*, 6(2), 214–220. https://doi.org/10.1038/s41550-021-01550-6

Yokoyama, T., Nagashima, K., Nakai, I., Young, E. D., Abe, Y., Aléon, J., Alexander, C. M. O'D., Amari, S., Amelin, Y., Bajo, K.-I., Bizzarro, M., Bouvier, A., Carlson, R. W., … Yurimoto, H. (2023). Samples returned from the asteroid Ryugu are similar to Ivuna-type carbonaceous meteorites. *Science*, 379(6634), eabn7850. https://doi.org/10.1126/science.abn7850

Chapter 6 Conclusion

6.1 Overall summary

In Chapter 1, the author presented the two challenges in XRF technique we are faced with. In Chapter 2, we confirmed that LE-M-XRF could analyze fluorine and lighter elements of samples. In Chapter 3, we developed the unique sample cells to achieve 1 mg-scaled quantitative analysis. At this point, matrix effects remained unsolved. In Chapter 4, we overcame this challenge by combining micro-XRF with Raman micro-spectroscopy, and the conversion matrix one-to-one corresponding to the two sets quantified cation compositions of carbonates accurately. In Chapter 5, the author updated the techniques presented before and completed the method to analyze dolomite grains on the asteroid Ryugu sample. Overall, the author has developed the non-invasive and quantitative analysis of chemical compositions of samples. Applicable samples are exceptionally rare to 1 mg, heterogeneous, light element containing, or complicated structured. Further, the proposed approach requires no pre-treatments, such as surface polishing or cutting. It is a completely non-invasive without any risks of sample damage or concerns about data reliability induced by instrumental effects like charge-up.

6.2 Comparison of the proposed method with others

6.2.1 Advantages of the proposed method

Elemental analysis is fundamental. To review advantages of the proposed approach, the author briefly summarizes other methods of elemental analysis from six points (Table 6.1). Here, “non-invasive” includes “sample as-is” and “Non-destructive.” The former means that a sample can be loaded to an instrument without any pre-treatments, and the latter means that method itself provides no risk of sample damage.

For example, wavelength dispersive X-ray fluorescence analysis (WDXRF) can quantify light elements from carbon accurately and non-destructively, whereas pre-treatments called the glass bead technique are essentially necessary. Also, primary beams collimated are not small sufficient to clarify the heterogeneity of a sample. Therefore, kinds of measurable samples or purposes for analyses will be limited.

Aramendia et al. (2018) summarized the advantages and disadvantages of several techniques for the chemical analysis of meteorites. For example, inductively coupled plasma mass spectroscopy (ICP-MS) gives decisive values. Nevertheless, it also has a drawback; the characteristics that the sample possesses will be gone—specifically, complicated morphology on the surface and heterogeneous composition of the sample due to its sample pre-treatments; hence, the data results in averaging the entire volume analyzed. Clarification of spatial distributions of elements with the surface morphology intact is of importance. In this regard, scanning electron microscopy with energy dispersive X-ray spectroscopy (SEM-EDS), electron probe microanalyzer (EPMA), and secondary ion mass spectrometry (SIMS) are also powerful analytical tools (Aramendia et al., 2018). Their elemental imaging at a micrometer-to-nanometer scale of spatial resolution clarifies the sample's physical and chemical heterogeneity. However, one critical point is that they undergo pre-treatments, for instance, sample sectioning, surface polishing, or metal/carbon coating, to avoid charging through electronic or ionic irradiation onto the sample surfaces. These pre-treatments frequently lose primitive information about surface roughness or porosity and negatively influence elements' spatial distribution or quantitative accuracy. In addition, the author points out that EPMA and SIMS require extended duration for a measurement at once. Such prolonged measurement time may induce unwanted alteration to a sample due to moderate

atmospheric oxidation or vacuum dehydration.

Smith (1995) reviewed general information on synchrotron radiation micro-XRF (SR-XRF). SR-XRF has a high-energy source with strong brightness and excellent spatial resolution at a sub-micron scale. Further, X-ray Absorption Fine Structure (XAFS) can be simultaneously obtained with SR-XRF, which enables to reveal the chemical state of that sample. However, SR-XRF suffers from a critical drawback called the "matrix effect" and presents quite limited access to synchrotron light sources. However, SR-XRF suffers from a critical drawback called the "matrix effect," when the size of analytes of interest is on the micrometer scale.

Table 6.1 Comparison of the proposed methods with others in elemental analysis.

	The proposed method	WDXRF	ICP-MS	SEM-EDX	EPMA	SIMS	SR-XRF
Milligram-scaled	✓✓✓	✓✓	✓✓✓	✓✓✓	✓✓✓	✓✓✓	✓✓✓
Sample as-is	✓✓✓	✓✓		✓✓	✓✓	✓	✓
Non-destructive	✓✓✓	✓✓✓		✓✓	✓✓		✓✓✓
Quantification	✓✓✓	✓✓✓	✓✓✓	✓✓✓	✓✓✓	✓✓✓	✓✓✓
Heterogeneity	✓✓✓			✓✓✓	✓✓✓	✓✓✓	✓✓✓
Light element analysis	✓✓✓	✓✓✓	✓✓	✓✓	✓✓✓	✓✓✓	✓✓✓

6.2.2 Disadvantages of the proposed approach

The essence of the present method is to provide elemental quantitative analysis of

elements (or cations) with Raman spectroscopy. Therefore, a crucial disadvantage is, if a sample has strong self-fluorescence or vibrational modes that are Raman-inactive, like pure metal, the Raman scattering will barely or never arise. Moreover, the method is unsuitable for a sample with no variation in elemental compositions, such as isomers, isotopes, or polymorphism of crystals because no correlation between shifts of Raman wavenumbers and compositions will be gained. In this regard, determining the concentration in the form of a molecule or composition is hardly possible.

6.3 Future prospects

The author presents six promising fields to apply the proposed technique: cosmochemistry, art conservation, forensic science, resource exploration, advanced materials, and environmental studies. The investigation of the asteroid Ryugu sample is a representative example of cosmochemistry, and therefore, other five fields will be discussed.

For example, the proposed technique will provide helpful information for the conservation of cultural properties. We are not allowed to damage the works, and therefore, it is difficult to collect large quantities of specimens. On the other hand, oil paintings will deteriorate over time, and colors have faded since their production. Some bricks and murals are unfired and fragile under harsh natural environments. Thus, art conservation and preservation have not been well developed. This is partly because materials used, production ages, restoration histories, and damaging processes are poorly understood, and Bitossi et al. (2005) reviewed there were limited methods available to investigate. Lately, Burgio et al. (2010) analyzed artworks produced in Italian medieval and Renaissance periods to create a database of pigments, using XRF and Raman

spectroscopies. Our proposal will be more favorable because its quantitative nature may allow us to identify mixtures of pigments or art materials and their blending ratios, providing fruitful information for making better care or storage environments.

Another example is a contribution to a criminal investigation. According to Muro et al. (2015), methods should be non-destructive, rapid, quantitative and confirmatory in order to prevent unwanted bias about results from an investigator or expert witness. Also, the methods must analyze specimens that are milligram or microgram scaled, such as drugs, DNA, salts on a fingerprint, or soil from a perpetrator's shoe. The composition of trace evidence left behind at the scenes of an incident or crime will provide beneficial information to solve criminal cases.

Moreover, our technology will be helpful for resource exploration. Rapid excavation of materials, minerals (*e.g.,* carbonates or fluorites), and energy resources (*e.g.,* rare earth elements) is valuable in this field. Secchi et al. (2018) built a combination system coupling several techniques, including infrared, XRF and Raman spectroscopies, and investigated drilled cores. Since our technology is also completely laboratory-based, a remote sensing explorer will have direct access to vast piles of waste, incinerator ash, or the ocean floor, which human beings rarely enter, and will find trace elements at micrometer-scaled spots on-site.

Another example is advanced materials. In recent years, reinforced fiber plastics by light elements, such as carbon or boron, have been popular in aircraft and military craft due to their superior lightness and strength. On-site analysis through our technology will contribute to quality assessment by detecting foreign matter without any sample pre-treatments or charge-up. In addition, quantitative evaluation of high performance light elements can benefit material engineering.

The author expects environmental studies are also interesting. The chemical compositions of environmental pollutants, such as fine particulate matter (PM2.5) or microplastics (MPs) may contribute to identifying their source and diffusion patterns. Traditionally, infrared spectroscopy, Raman spectroscopy, or gas chromatography-mass spectrometry (GCMS) have been available (Pan et al., 2022). Micro-XRF imaging enables quick, wide-range, and quantitative investigation, and the following Raman measurements can specify components of pollutants. In the future, our technology will aid in monitoring pollutant particles in real-time and quantitatively evaluate the degree of pollution in local and global areas.

6.4 Conclusion and future prospects

Lastly, the author briefly reviewed previous chapters and described the advantages and disadvantages of our method in comparison with conventional methods. The author then introduced possible future directions. In conclusion, our method will be a powerful tool applicable to the analysis of diverse samples or purposes.

6.5 Bibliography

Aramendia, J., Gomez-Nubla, L., Castro, K., Fdez-Ortiz de Vallejuelo, S., Arana, G., Maguregui, M., Baonza, V., Medina, J., Rull, F., & Madariaga, J. (2018). Overview of the techniques used for the study of non-terrestrial bodies: Proposition of novel non-destructive methodology. *TrAC Trends in Analytical Chemistry.*, 98:36–46. https://doi.org/10.1016/j.trac.2017.10.018

Bitossi, G., Giorgi, R., Mauro, M., Salvadori, B., & Dei, L. (2005). Spectroscopic Techniques in Cultural Heritage Conservation: A Survey. *Applied Spectroscopy*

Reviews, 40(3), 187–228. https://doi.org/10.1081/ASR-200054370

Burgio, L., Clark, R. J. H., & Hark, R. R. (2010). Raman microscopy and x-ray fluorescence analysis of pigments on medieval and renaissance Italian manuscript cuttings. *Proceedings of the National Academy of Sciences*, 107(13), 5726–5731. https://doi.org/10.1073/pnas.0914797107

Muro, C. K., Doty, K. C., Bueno, J., Halámková, L., & Lednev, I. K. (2015). Vibrational Spectroscopy: Recent Developments to Revolutionize Forensic Science. *Analytical Chemistry*, 87(1), 306–327. https://doi.org/10.1021/ac504068a

Pan, S., Qiu, Y., Li, M., Yang, Z., & Liang, D. (2022). Recent Developments in the Determination of $PM_{2.5}$ Chemical Composition. *Bulletin of Environmental Contamination and Toxicology*, 108, 819–823. https://doi.org/10.1007/s00128-022-03510-w

Secchi, M., Zanatta, M., Borovin, E., Bortolotti, M., Kumar, A., Giarola, M., Sanson, A., Orberger, B., Daldosso, N., Gialanella, S., Mariotto, G., Montagna, M., & Lutterotti, L. (2018). Mineralogical investigations using XRD, XRF, and Raman spectroscopy in a combined approach. *Journal of Raman Spectroscopy*, 49(6), 1023–1030. https://doi.org/10.1002/jrs.5386

Smith, J. V. (1995). Tutorial review. synchrotron x-ray sources: instrumental characteristics. new applications in microanalysis, tomography, absorption spectroscopy and diffraction. *Analyst*, 120, 1231–1245. https://doi.org/10.1039/AN9952001231

Appendix A Supporting information for Chapter 2

A.1 Details information about the samples studied

Samples analyzed in Chapter 2 with detail information are summarized here. A piece of the PTFE tube 15 mm long with a 6 mm/4 mm (outer/inner) diameter was prepared. We dissected to produce a flat surface and probed at the spot indicated by the black arrowhead (Figure A.1). The 6-way switching valve made of stainless was taken out from the sulfur analyzing unit named EMIA-Step (HORIBA, Ltd.) for investigating the cause of failure and the corrosion (Figure A.2). This valve works to trap unwanted gases like the halogens or to purge carrier gases, such as He or Ar by switching the flows. The surface of the valve is frequently damaged by friction heat, corrosive substances from samples, and foreign matter. We carefully dismantled a cylindric battery cell in the glove box and removed a set of separators and electrodes called jelly roll (Figure A.3). Subsequently, we unrolled the jelly roll. The chamber of XGT-9000 can make room for such a large sheet of separator 138 mm high and 80 mm wide contacting the positive electrode. The area of 0.75 mm high and 2.56 mm wide was analyzed. The separator comprised three layers: polyamide-imide (PAI), ceramics, and polyethylene/polypropylene.

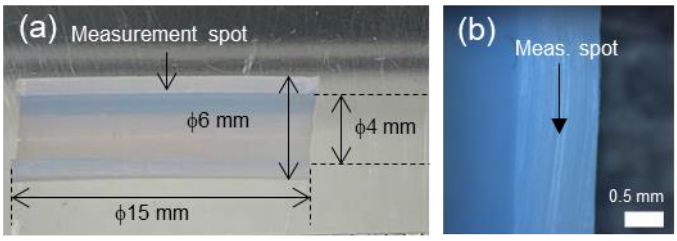

Figure A.1 (a) Whole picture of the PTFE tube and (b) an enlarged picture indicating a measurement spot.

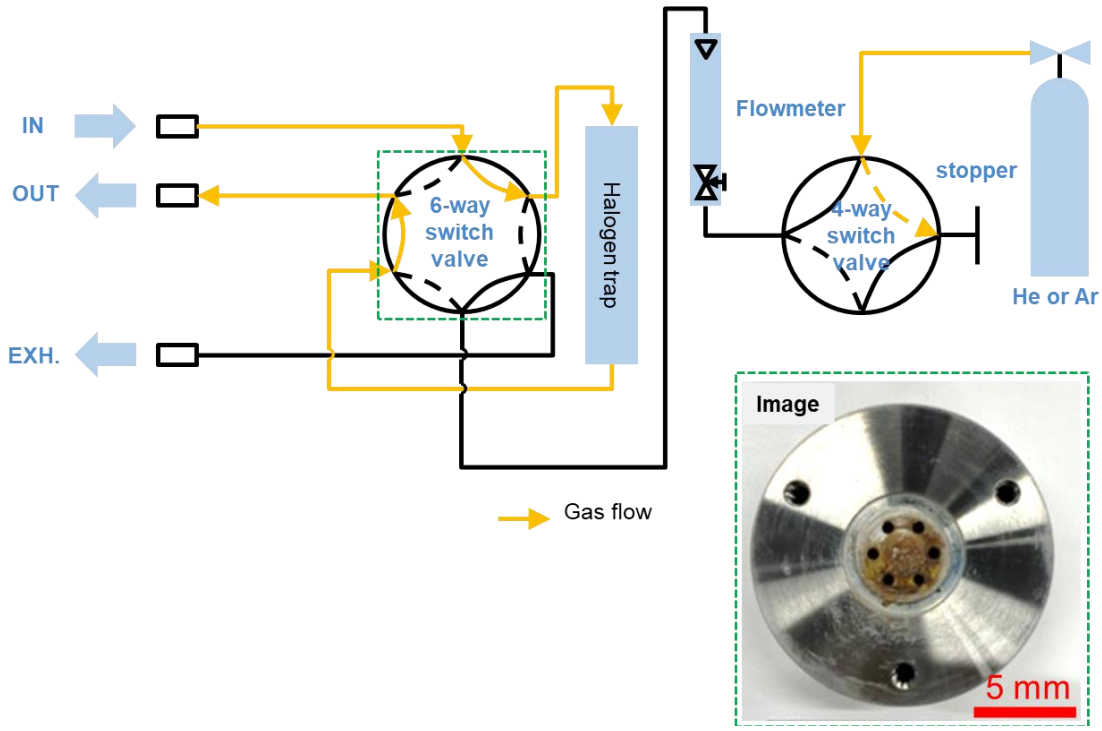

Figure A.2 Block diagram for flows around the 6-way switch valve and its whole picture. IN: influx from the furnace to the analyzing unit, OUT: outflux from the valve to the analyzing unit, EXH: exhaust.

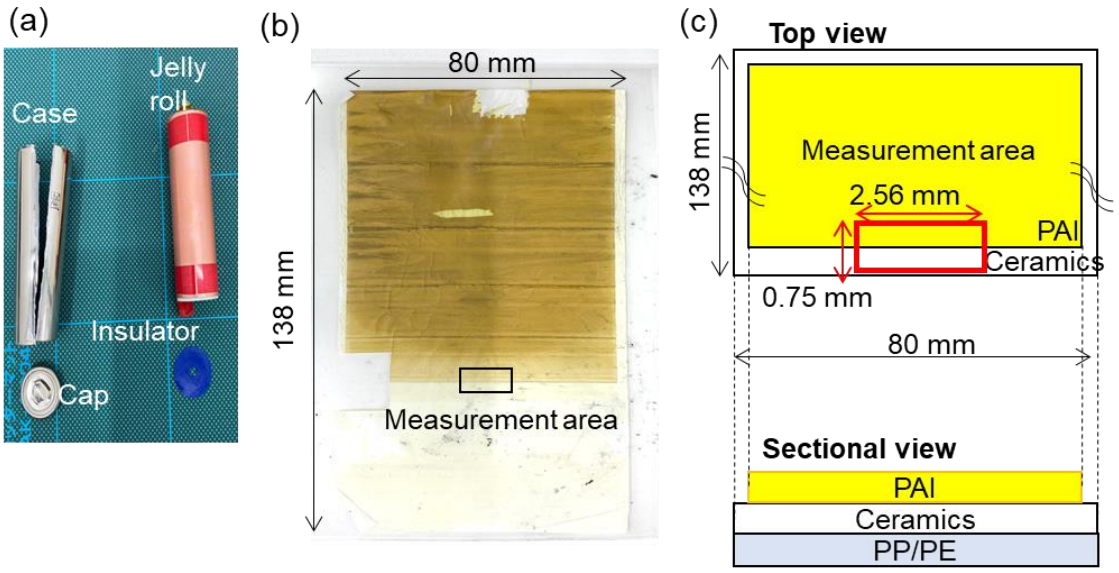

Figure A.3 Details about the separator sheet of automotive battery. A dismantled cylindric cell (a), a whole picture of separator sheet (b), a schematic diagram representing structures (c).

A.2 XRF spectrum for the 6-way switch valve

Figure A.4 shows the summed spectra of the 6-way switch valve, which represented the entire area examined.

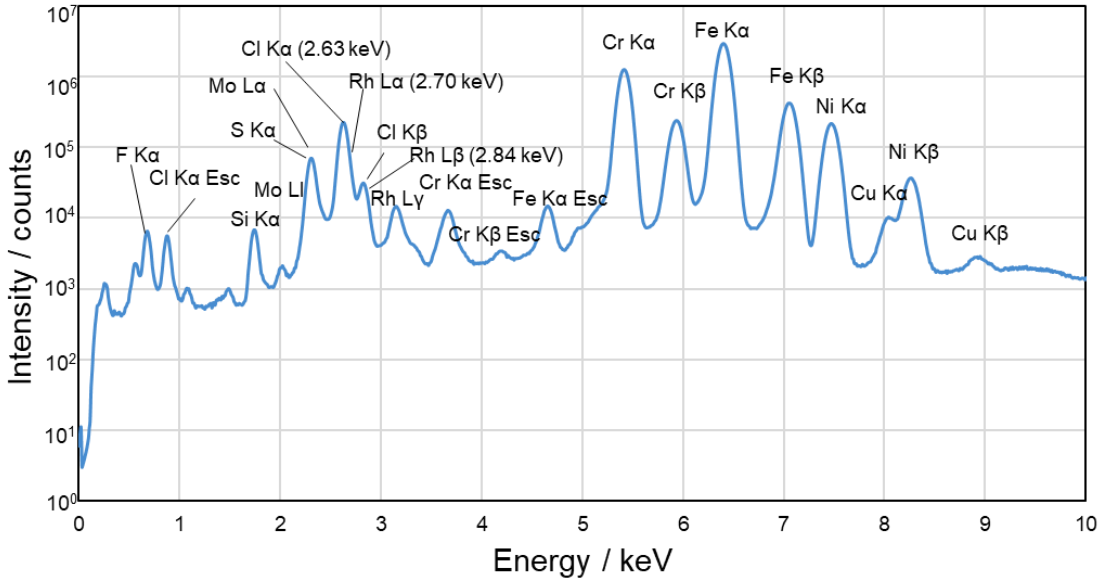

Figure A.4 Summed XRF spectrum for the 6-way switch valve. Esc: Escape peak.

Appendix B Supporting information for Chapter 3

B.1 XRF spectra and quantitative results of 10 mg samples

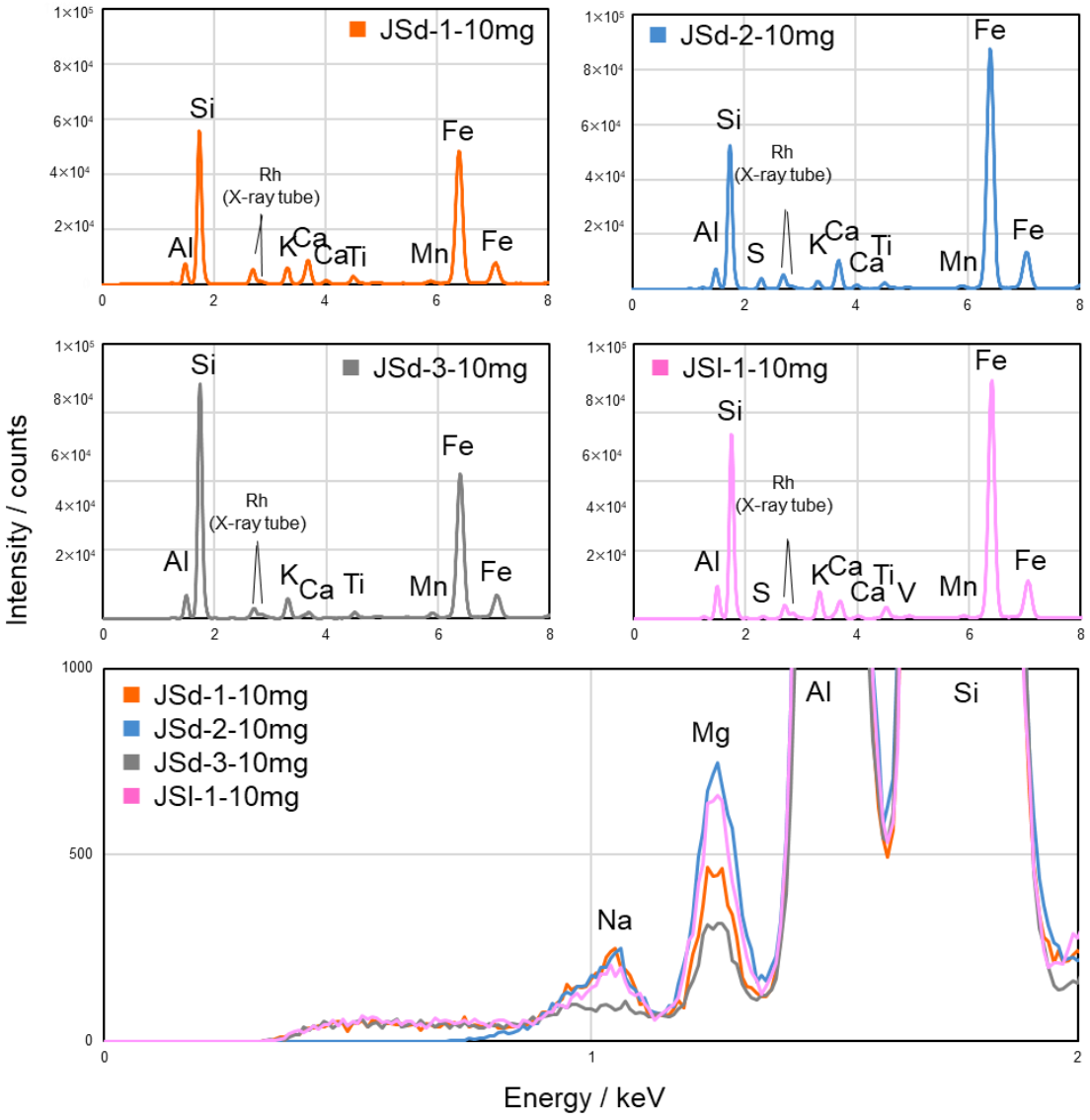

Figure B.1 XRF spectra of samples weighing 10 mg in lower energy regions. Each spectrum indicates a single measurement of the respective sample.

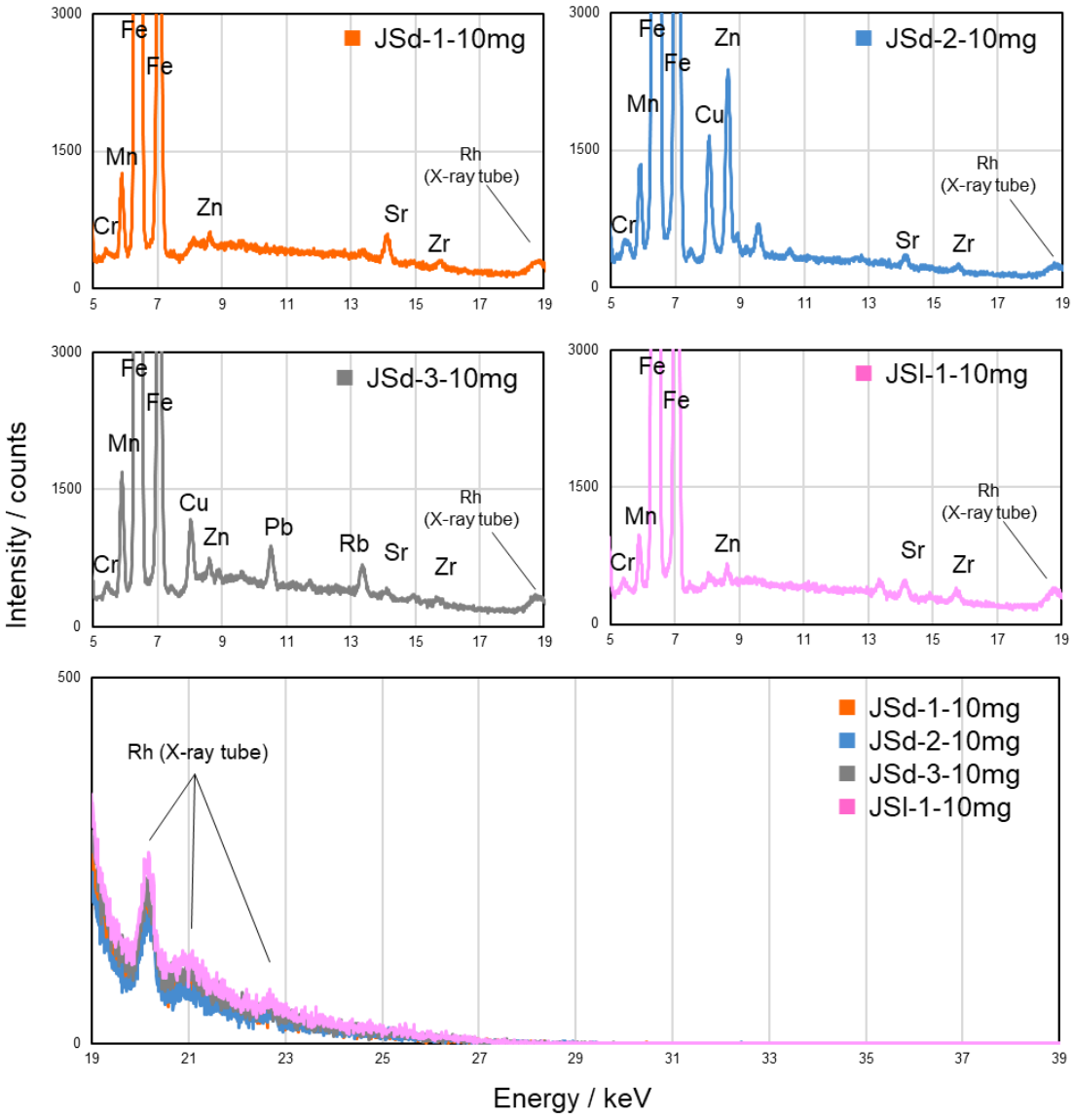

Figure B.2 XRF spectra of samples weighing 10 mg in higher energy regions. Each spectrum indicates a single measurement of the respective sample.

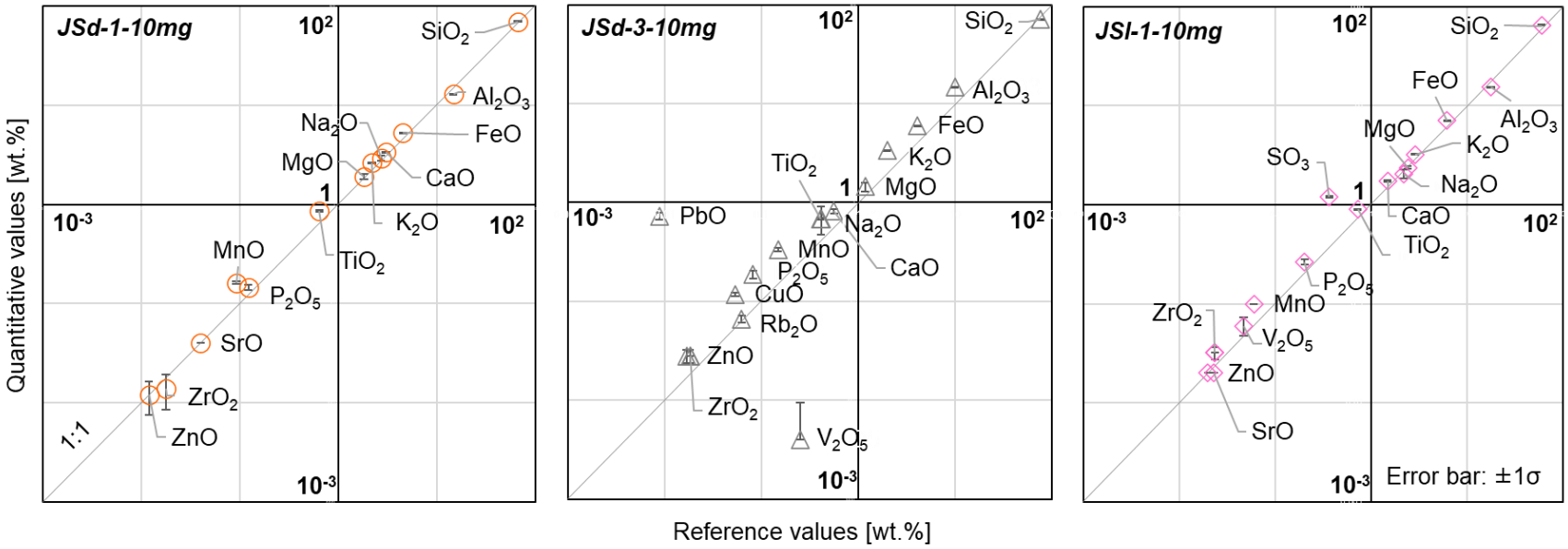

Figure B.3 The accuracy of quantitative analysis in comparison with reference values for 10 mg samples. The error bars indicate 1σ of 10 times repeated measurements.

B.2 XRF spectra and quantitative results of 100 mg samples

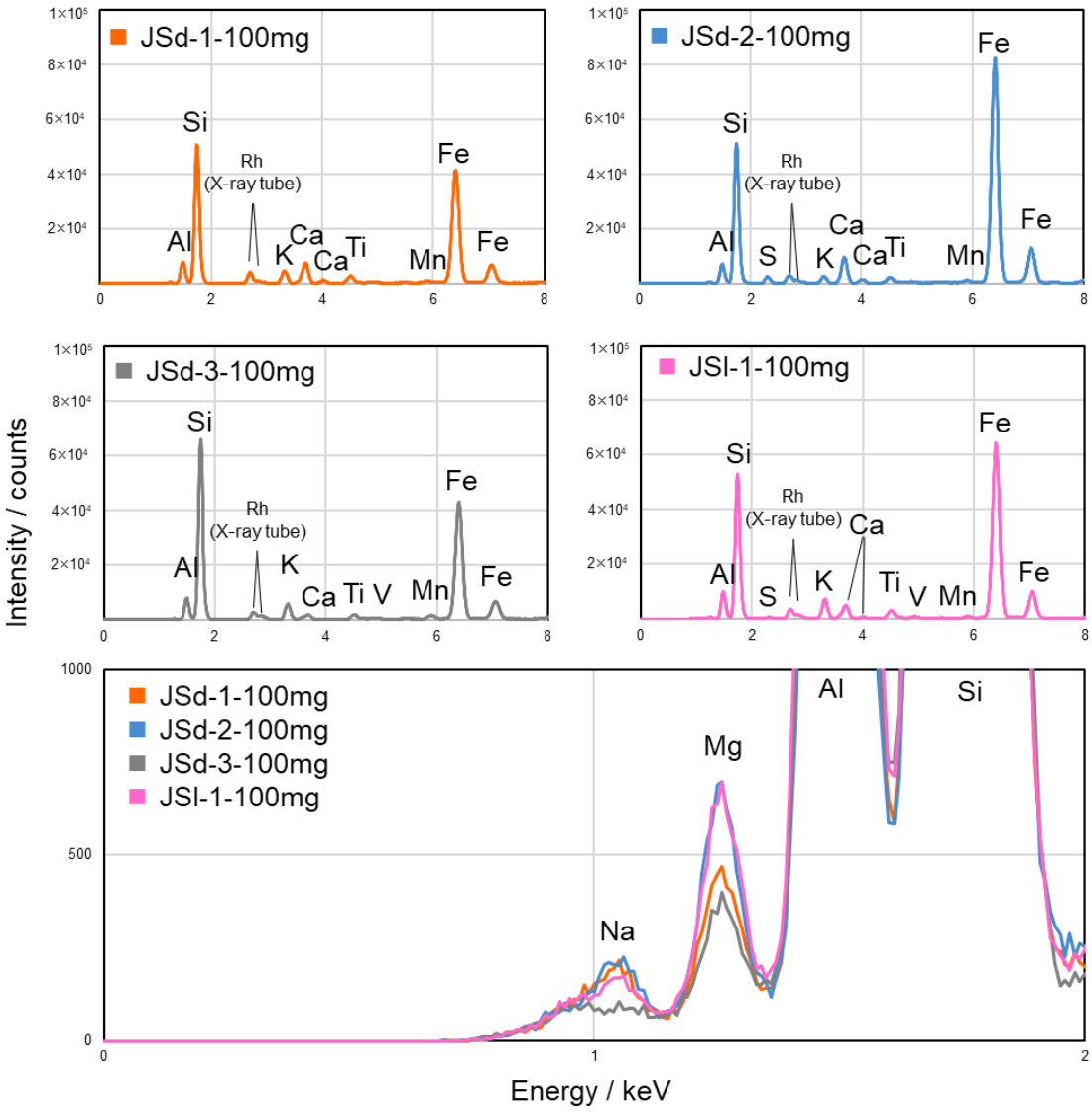

Figure B.4 XRF spectra of samples weighing 100 mg in lower energy regions. Each spectrum indicates a single measurement of the respective sample.

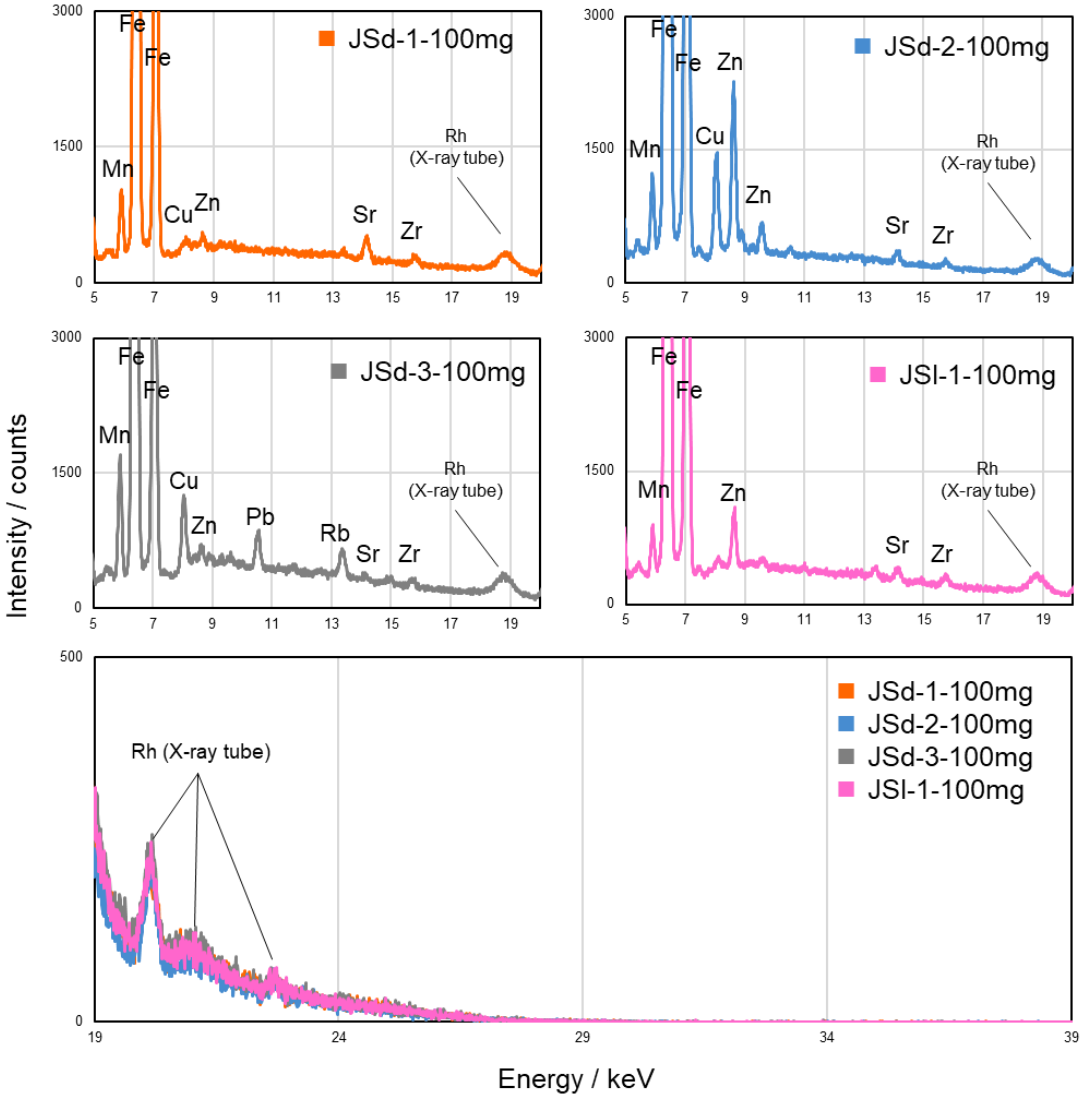

Figure B.5 XRF spectra of samples weighing 100 mg in higher energy regions. Each spectrum indicates a single measurement of the respective sample.

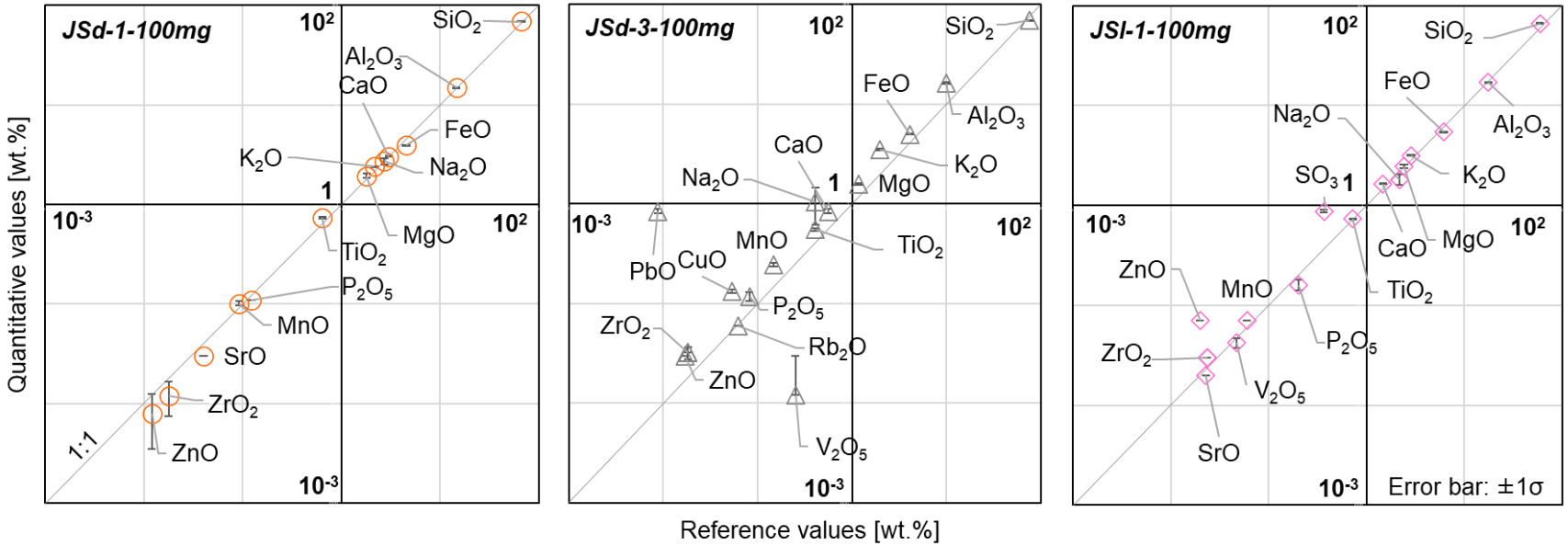

Figure B.6 The accuracy in quantitative analysis in comparison with reference values for 100 mg samples. The error bars indicate 1σ of 10 times repeated measurements.

B.3 Comparison of the quantitative results in different sample weights

To test the quantitative accuracy of the proposed method, we analyzed the JSd series and JSl-1. Assuming all elements were in oxide form, we quantified elements by the standard fundamental parameter method. The quantitative values were the averaged ones of the 10 times repeated measurements, and the standard deviations indicate 1σ.

Table B.1 The results of JSd-1 in different sample weights (unit: wt. %)

	reference values	1 mg quantitative values	SD (σ)	10 mg quantitative values	SD (σ)	100 mg quantitative values	SD (σ)
Na_2O	2.727	3.146	0.122	2.928	0.168	2.716	0.180
MgO	1.813	1.736	0.072	1.900	0.124	1.948	0.093
Al_2O_3	14.65	14.632	0.103	12.966	0.067	15.048	0.097
SiO_2	66.55	69.892	0.140	69.676	0.194	69.882	0.155
P_2O_5	0.122	0.074	0.019	0.146	0.009	0.110	0.000
K_2O	2.183	2.406	0.015	2.634	0.026	2.404	0.036
CaO	3.034	3.464	0.005	3.364	0.022	3.058	0.020
TiO_2	0.643	0.590	0.014	0.858	0.011	0.742	0.013
MnO	0.0924	0.084	0.005	0.162	0.004	0.102	0.004
FeO	4.535	3.920	0.012	5.302	0.026	3.928	0.022
ZnO	0.012	0.010	0.000	0.012	0.004	0.008	0.004
SrO	0.04	0.030	0.000	0.040	0.000	0.030	0.000
ZrO_2	0.0178	0.018	0.004	0.014	0.005	0.012	0.004

Table B.2 The results of JSd-1 in different sample weights (unit: wt. %, N.D.: not detected.)

	reference values	1 mg quantitative values	SD (σ)	10 mg quantitative values	SD (σ)	100 mg quantitative values	SD (σ)
Na_2O	0.411	0.748	0.421	0.690	0.220	1.040	0.419
MgO	1.17	1.348	0.053	1.450	0.148	1.586	0.038
Al_2O_3	9.908	16.368	0.287	14.620	0.112	16.372	0.221
SiO_2	76	71.232	0.459	70.866	0.211	69.650	0.536
P_2O_5	0.0817	0.122	0.013	0.188	0.018	0.118	0.013
K_2O	1.971	3.484	0.040	3.366	0.032	3.488	0.074
CaO	0.56	0.928	0.016	0.818	0.041	0.842	0.041
TiO_2	0.403	0.454	0.011	0.684	0.013	0.552	0.018
V_2O_5	0.25136	0.014	0.026	0.004	0.005	0.012	0.018
MnO	0.148	0.180	0.010	0.336	0.015	0.244	0.009
FeO	4.092	4.382	0.071	6.000	0.039	5.000	0.032
CuO	0.0533	0.104	0.005	0.118	0.004	0.134	0.005
ZnO	0.0169	0.016	0.005	0.028	0.004	0.030	0.000
Rb_2O	0.0623	0.040	0.000	0.066	0.005	0.060	0.000
ZrO_2	0.0183	0.012	0.004	0.028	0.004	0.032	0.004
BaO	0.0518	*N.D.*	*N.D.*	*N.D.*	*N.D.*	*N.D.*	*N.D.*
PbO	0.0088	0.564	0.031	0.732	0.057	0.842	0.043

Table B.3 The results of JSl-1 in different sample weights (unit: wt. %, N.D.: not detected.)

	reference values	1 mg quantitative values	SD (σ)	10 mg quantitative values	SD (σ)	100 mg quantitative values	SD (σ)
Na_2O	2.184	2.258	0.158	2.066	0.216	1.806	0.220
MgO	2.413	2.408	0.087	2.380	0.059	2.460	0.079
Al_2O_3	17.6	17.834	0.094	15.394	0.055	17.132	0.067
SiO_2	59.47	64.564	0.184	65.522	0.092	66.370	0.239
P_2O_5	0.202	0.176	0.021	0.266	0.017	0.160	0.020
SO_3	0.3667	0.596	0.015	1.198	0.018	0.876	0.025
K_2O	2.845	3.552	0.043	3.236	0.023	3.168	0.044
CaO	1.479	1.794	0.005	1.736	0.033	1.644	0.023
TiO_2	0.725	0.712	0.008	0.906	0.005	0.734	0.005
V_2O_5	0.0467	0.056	0.013	0.060	0.012	0.042	0.004
MnO	0.0599	0.060	0.000	0.100	0.000	0.070	0.000
FeO	6.18	5.934	0.005	7.066	0.023	5.416	0.022
ZnO	0.0198	0.010	0.000	0.020	0.000	0.070	0.000
SrO	0.0228	0.020	0.000	0.020	0.000	0.020	0.000
ZrO_2	0.0235	0.020	0.000	0.032	0.004	0.030	0.000
BaO	0.034	*N.D.*	*N.D.*	*N.D.*	*N.D.*	*N.D.*	*N.D.*

Appendix C Supporting Information for Chapter 4

C.1 The validation of the universal conversion matrix

To further examine the validity of this universal conversion matrix Eq. (4.2), we carried out a sort of "blind test" for each sample. Specifically, when making a conversion matrix for each mineral, we excluded the one of interest from the fitting and then calculated the cation compositions for the species excluded. The results in Figure C.1 agree with the experimental results, except for a slight deviation for calcite. This result implies that the conversion with Eq. (4.2) is sufficient to roughly estimate the compositions of unknown carbonates with a maximum error of 20%.

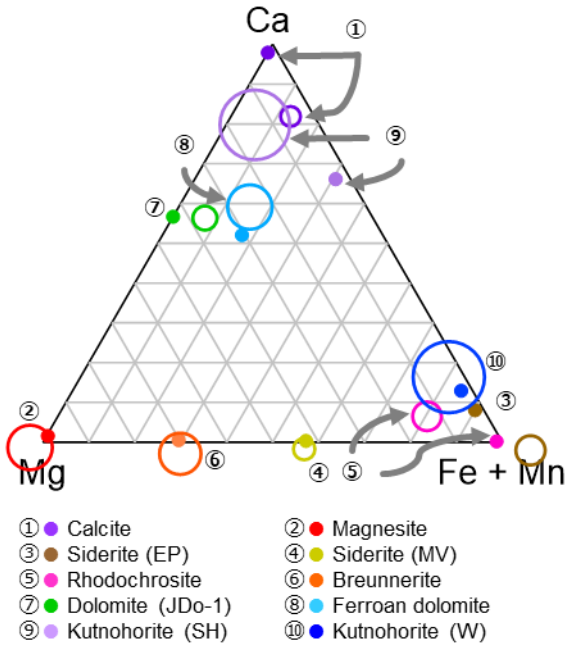

Figure C.1 Ternary diagram of experimented and calculated by the "blind test" in the main text for comparison.

C.2 Magnesite-breunnerite-siderite series

As for this solid solution series, the Ca content can be negligible. In the case of $x_{\mathrm{Fe}} +$

$x_{\mathrm{Mn}} \approx 1$, the difficulty is distinguishing Mg-bearing siderite from rhodochrosite from Raman spectra. Hence, only within the range $x_{\mathrm{Mg}}/(x_{\mathrm{Mg}} + x_{\mathrm{Fe}} + x_{\mathrm{Mn}})$ at x_{Mg}> ~0.4, the discussion is here to focus our attention on magnesite, breunnerite, and siderite (MV). As shown in Figure C.2, the ratio $x_{\mathrm{Mg}}/(x_{\mathrm{Mg}} + x_{\mathrm{Fe}} + x_{\mathrm{Mn}})$ linearly correlated with the T- and L- mode frequencies. Consequently, this ratio can be given from T or L mode frequency. We evaluated the compositions from the L mode frequency because it more broadly shifts along with the ratio $x_{\mathrm{Mg}}/(x_{\mathrm{Mg}} + x_{\mathrm{Fe}} + x_{\mathrm{Mn}})$ than the T mode frequency does. Being assumed $x_{\mathrm{Ca}} \approx 0$, x_{Mg}, and $x_{\mathrm{Fe}} + x_{\mathrm{Mn}}$ are obtained by:

$$\begin{pmatrix} x_{\mathrm{Mg}} \\ x_{\mathrm{Fe}} + x_{\mathrm{Mn}} \end{pmatrix} = \begin{pmatrix} 0.023067 & -6.5973 \\ -0.023067 & 7.5973 \end{pmatrix} \begin{pmatrix} \widetilde{\nu_{\mathrm{L}}} \\ 1 \end{pmatrix} \qquad (C.1)$$

The resulting values of x_{Mg} were 0.429, 0.702, and 0.999 for siderite (MV), breunnerite, and magnesite, respectively. Thus, the estimation error was less than 0.02 from the XRF results (Table 4.1). Again, it should be noted that the conversion matrix was built under the condition that the range is x_{Mg}> 0.4. We must remark that the conversion matrix will no longer be available when a sample is out of this range (*i.e.,* Fe and Mn richer).

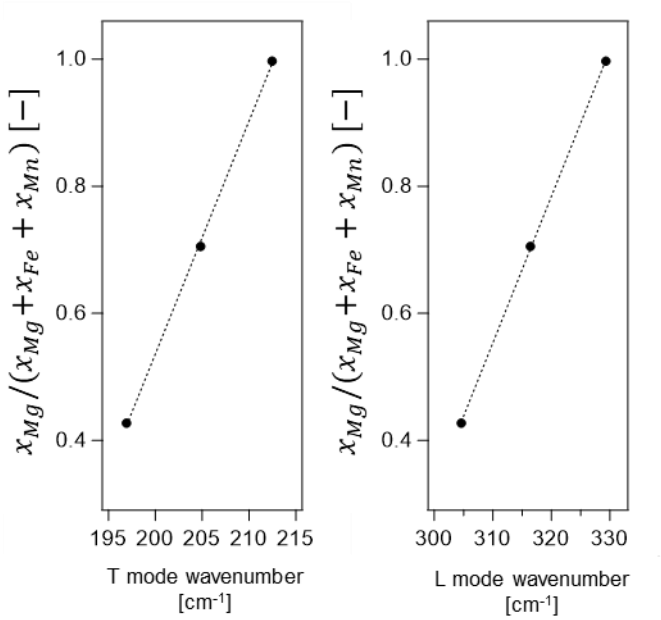

Figure C.2 $x_{\mathbf{Mg}}/(x_{\mathbf{Mg}}+x_{\mathbf{Fe}}+x_{\mathbf{Mn}})$ of siderite (MV), breunnerite, and magnesite against T (left) and L (right panel) mode wavenumbers. The dotted lines are of the linear fit.

C.3 Calcite-(pseudo) kutnohorite-rhodochrosite series

In Figure C.1, the estimated x_{Mg} is significantly deviated from the experimental value for carbonates containing negligible amount of Mg: calcite, kutnohorite (SH), kutnohorite (W), and rhodochrosite. Therefore, at least within our observation, if the estimated x_{Mg} from Eq. (C.1) is less than 0.15, it is desirable to assume that $x_{\mathrm{Mg}} \approx 0$. If a larger amount of Mg is estimated by the universal conversion, Eq. (5.1) should be chosen. This section presents the special matrix, given the assumption that $x_{\mathrm{Mg}} \approx 0$.

Since these four carbonates are also free from Fe, $x_{\mathrm{Mn}}/(x_{\mathrm{Ca}} + x_{\mathrm{Mn}})$ is discussed. Because the T mode wavenumber was more sensitive to the Ca/Mn substitution (Figure 4.3(b)), the plots of $x_{\mathrm{Mn}}/(x_{\mathrm{Ca}} + x_{\mathrm{Mn}})$ against the wavenumbers of T mode are shown in Figure C.3. In the figure, the linear fitting of $x_{\mathrm{Mn}}/(x_{\mathrm{Ca}} + x_{\mathrm{Mn}})$ against the T mode wavenumber was similar to the experimental plots. This is consistent with the other results previously described. Because $x_{\mathrm{Mn}}/(x_{\mathrm{Ca}} + x_{\mathrm{Mn}})$ is plotted in the wide range of $0 < x_{\mathrm{Mn}}/(x_{\mathrm{Ca}} + x_{\mathrm{Mn}}) < 1$, however, the non-linearity in the figure is more evident than in the others. To optimize the conversion matrix as much as possible, the fitting was conducted with a second-order polynomial function. Accordingly, the conversion matrix is derived as:

$$\begin{pmatrix} x_{\mathrm{Ca}} \\ x_{\mathrm{Mn}} \end{pmatrix} = \begin{pmatrix} 5.5778 \times 10^{-4} & -0.22436 & 22.425 \\ -5.5778 \times 10^{-4} & 0.22436 & -21.425 \end{pmatrix} \begin{pmatrix} \widetilde{\nu_{\mathrm{T}}}^2 \\ \widetilde{\nu_{\mathrm{T}}} \\ 1 \end{pmatrix} \quad (C.2)$$

The values of x_{Mn} for calcite, kutnohorite (SH), kutnohorite (W) and rhodochrosite resulted in 0.01, 0.30, 0.88, and 0.99, respectively. Similarly, the deviation given was within 0.05. However, as described in the former subsection (magnesite-breunnerite-siderite series), it is still challenging to discriminate rhodochrosite from Mg-bearing siderite; hence, the conversion with Eq. (C.2) should be applied only in the case of $\widetilde{\nu_{\mathrm{T}}} <$

180 cm^{-1}. This is because $\widetilde{\nu_{\mathrm{T}}}$ was not less than 180 cm^{-1} for any carbonates of magnesite-breunnerite-siderite series (Figure 4.5(b)). Under this restriction, X_{Mn} can be estimated within wide region of $0 < X_{\mathrm{Mn}} < 0.8$ with Eq. (C.2).

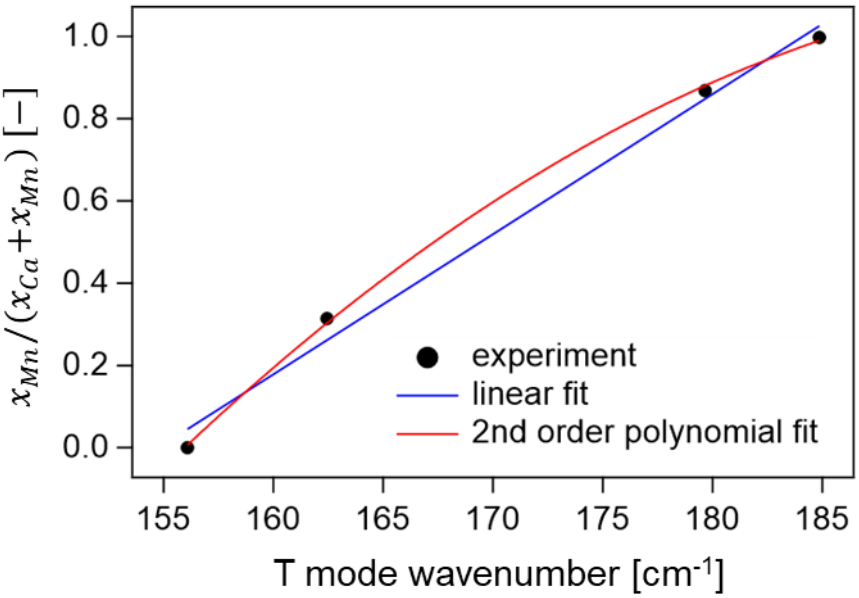

Figure C.3 $x_{\mathrm{Mn}}/(x_{\mathrm{Ca}} + x_{\mathrm{Mn}})$ of calcite, kutnohorite (SH), kutnohorite (W) and rhodochrosite plotted against the T mode wave numbers.

Appendix D Supporting Information for Chapter 5

D.1 Finer conversion for the dolomite group

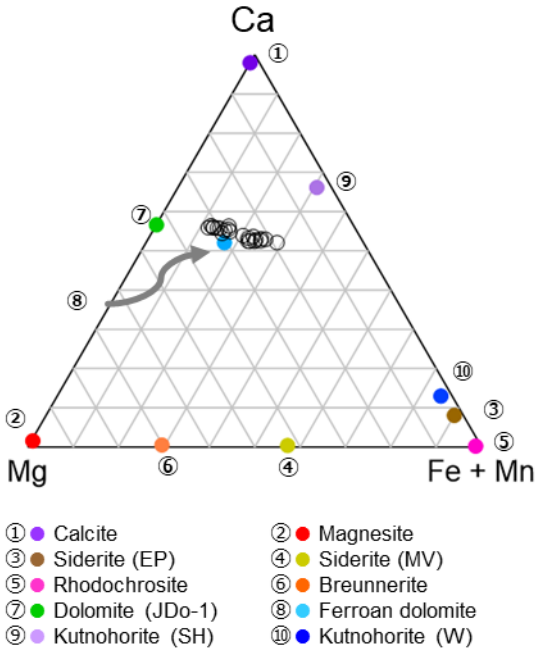

Figure D.1 Cation compositions of ferroan dolomites in ternary diagram with different spots (black circles).

Figure 5.4 demonstrates that T and L mode wavenumbers of ferroan dolomite obtained at a single Raman measurement are widely spread. The cation compositions calculated by Eq. (5.1) are summarized in Figure D.1. Here, even though the Ca contents were marginally overestimated, it turned out that the deviation from the experimental values was <0.04 on average. Notably, the cation compositions by Eq. (5.1) had a both linear and wide distribution, whereas the standard deviation of the cation compositions evaluated by XRF was as small as 0.003 (See Table 4.1). This can be explained by the difference in the spatial resolution between Raman spectroscopy and XRF. For example, the spatial resolution for Raman spectroscopy is approximately 1 μm, thus realizing to probe micrometer-scaled inhomogeneity spot-by-spot, while XRF measurements are averaged due to an even larger spatial resolution of approximately 100 μm.

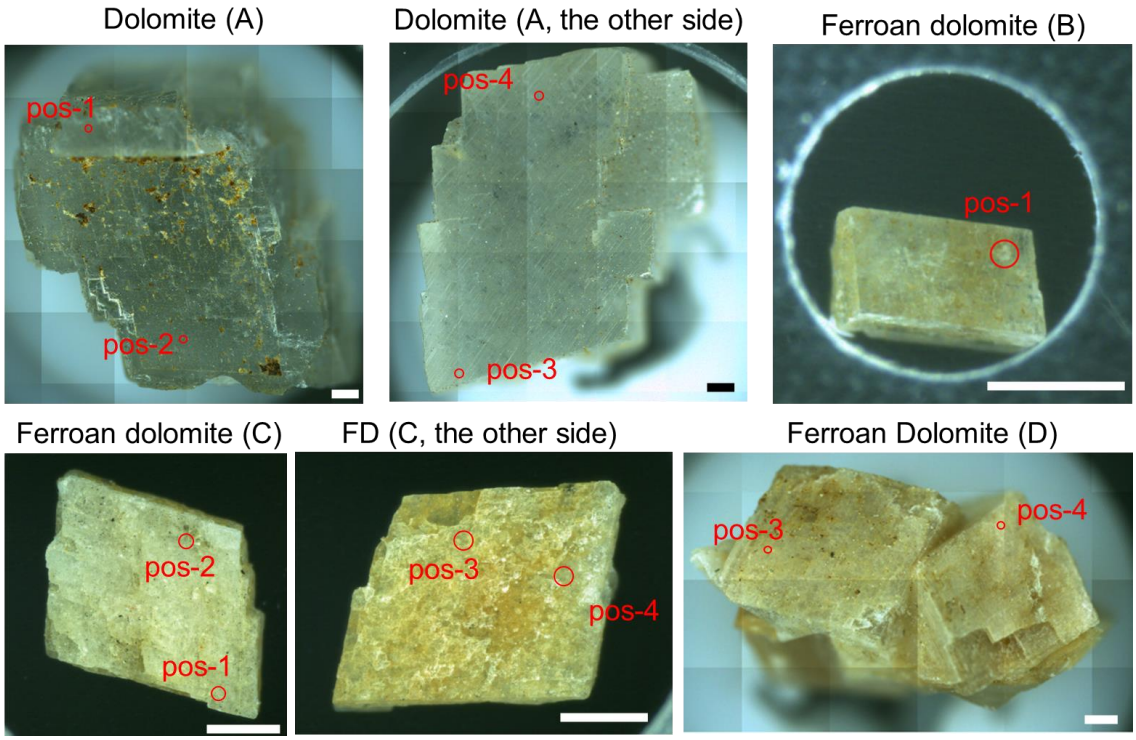

Figure D.2 Optical images of the dolomites prepared. Scale bars are 0.5 mm. FD: ferroan dolomite.

D.2 Construction of the Fe+Mn scale

D.2.1 Experiments

Natural dolomites

Prepared were dolomite mined at Azcárate Quarry, Navarre, Spain. As for ferroan dolomite, a chip from the larger one mined at Eagle Mine, Colorado, USA, used in the study of the carbonate conversion was hammered and then prepared. They originate in not igneous rocks but sedimentary rocks, according to the quarries' information. Because the cation compositions significantly differed spot-by-spot, three more small chips named (B), (C) and (D) were prepared. Figure D.2 shows the optical images of the dolomites and measurement spots. It should be noted that the shape of each chip was all rhombohedral, but its color was not uniform. For the calibration of XRF spectra, geo-standards JLk-1

and JDo-1 (The National Institute of Advanced Industrial Science and Technology, Japan) were also measured (Imai et al., 1996). The lake sediment reference JLk-1 consists of SiO_2 (57.16 wt.%), Al_2O_3 (16.73 wt.%), Fe_2O_3 (6.929 wt.%), MgO (1.736 wt.%), CaO (0.6686 wt.%) and MnO (0.266 wt.%). The dolomite reference JDo-1 consists of CaO (33.96 wt.%), MgO (18.47 wt.%), Fe_2O_3 (0.0208 wt.%), MnO (0.000657 wt.%) and CO_2 (46.5 wt.%). The full information is available in the reference (Imai et al., 1996).

Micro-XRF

Micro-XRF analysis was carried out with a HORIBA XGT-9000 X-ray Analytical Microscope (Morita et al., 2022). The primary X-ray focused on the sample was a diameter of approximately 100 μm. The Rh-target X-ray tube voltage was 30 kV, the tube current was 1000 μA. To examine the heterogeneity of Fe+Mn abundance within one chip, we probed a couple of positions in each chip, and the measurement time for each was set to be relatively more prolonged, 100 s. For quantifying cations, standard FPM (Sherman, 1955; Shiraiwa & Fujino, 1966) was applied. As previously described, JLk-1 and JDo-1 were used for ferroan dolomites and dolomites, respectively.

Raman micro-spectroscopy

The Raman spectra were acquired with a lab-built spectrometer. The details of the optical setup have been described elsewhere (Urashima et al., 2022). Briefly, a 532-nm laser (cobolt samba) was divided by a 10:90 (transmission: refection) beam splitter. The transmitted light was introduced to a microscope BX51 (Olympus) and focused on the sample by an objective lens (Olympus; LMPlan FL N; ×100, NA 0.80, WD 3.4 mm). The scattered light was collected by the same objective lens and separated from the incident beam by the 10:90 beamsplitter. The Rayleigh scattering was filtered by BragGrate Notch filters (Optigrate), and the filtered light was introduced to a polychromator (HORIBA;

iHR-320) with a CCD (HORIBA; Syncerity). A grating with 2400 grooves/mm was used in the polychromator for precisely determining the peak wavenumbers. The excitation power was approximately 1.5–1.7 mW and 2.6–2.8 mW at the sample face for dolomite and ferroan dolomite, respectively. The exposure time was 30 s and 45 s for dolomite and ferroan dolomite, respectively, and the spectra obtained by two consecutive measurements were averaged. The measurement conditions were different for dolomite and ferroan dolomite because Raman spectra of ferroan dolomite were weaker than those of dolomite. Because the cation composition was heterogeneous even in one chip, Raman spectra were obtained from the same areas as the XRF measurements. However, the spatial resolution of Raman spectra was as high as or better than 1 μm, whereas that of the micro-XRF was about 100 μm. Thus, Raman spectra were obtained at 25 grid points in an approximately 50×50 μm region to acquire an averaged value for comparison with the XRF data.

D.2.2 Results and discussions

The images of the sample chips and their measurement positions are shown in Figure D.2, whose XRF spectra are presented in Figure D.3. Here are two notes: X-ray fluorescence yield varies depending on elements. Second, more simply, heavier elements emanate stronger fluorescence. Hence, the Mg signal can be weaker than the other three elements, whereas the amount of Mg surpasses the others. Each element abundance in our analysis was determined through standard FPM. In comparison, the peak intensity for a specific element is proportional to its concentration and can be compared among the samples if their matrix compositions are similar. In this regard, matrix effects from the samples studied can be nearly canceled out because the matrix compositions are predominantly Ca, Mg, and carbonate CO_3^{2-}. In the XRF spectra of dolomite (A), the peaks for Ca were

remarkable, and those for Mg were small but noticeable. On the other hand, the peaks for Mn and Fe were outstanding in the spectra of ferroan dolomites (B-D), and those for Mg were almost absent at some positions, such as position-1 of ferroan dolomite (D). Notably, even within a single chip of ferroan dolomite, the peak intensities of Fe and Mn dramatically varied depending on the positions analyzed. Specifically, the Mn peak was higher at position-3 than at position-4 in ferroan dolomite (C). The cation compositions determined from these XRF spectra are summarized in Table D.1.

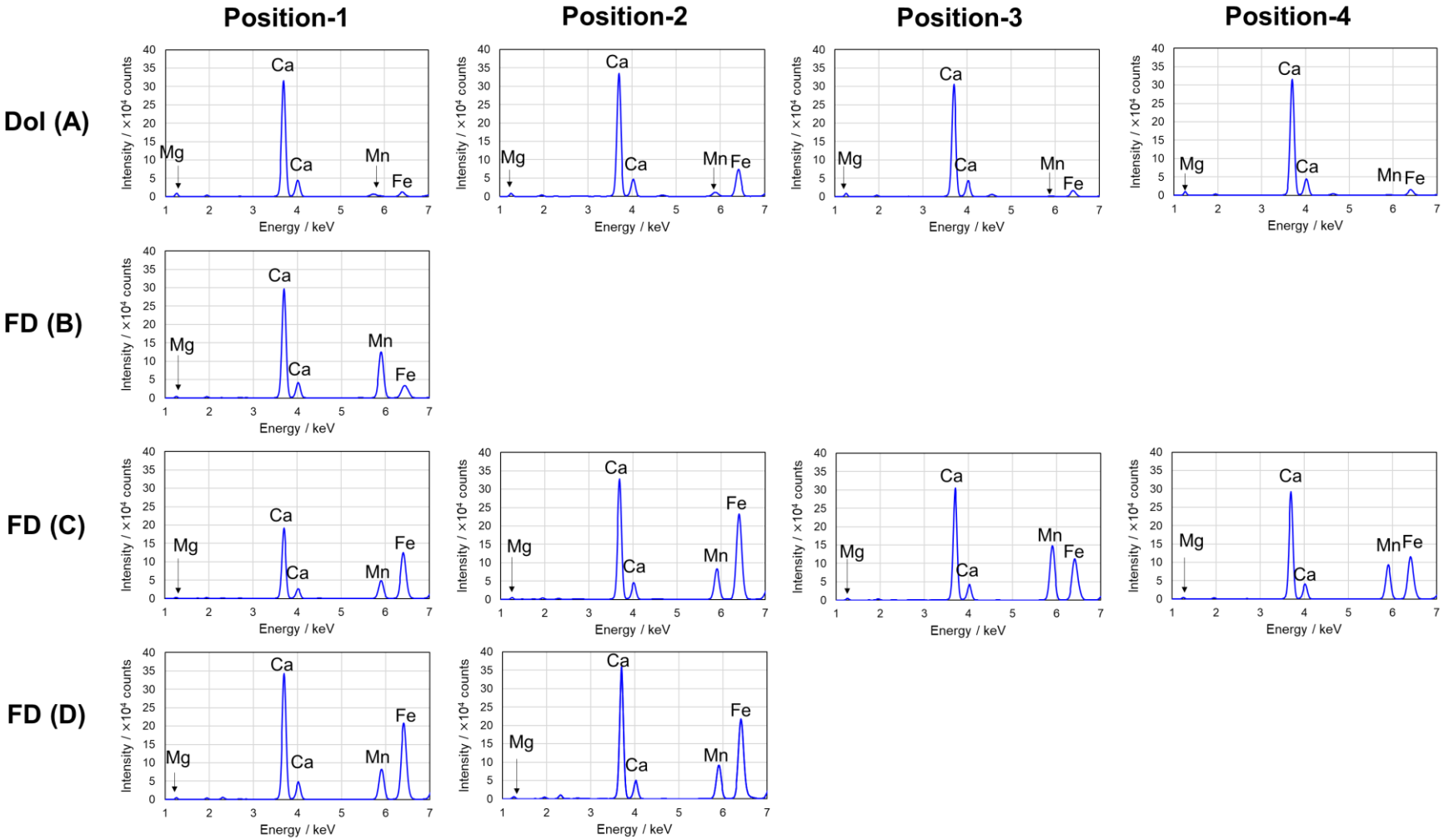

Figure D.3 XRF spectra obtained at each measurement position. Dol: dolomite, FD: ferroan dolomite.

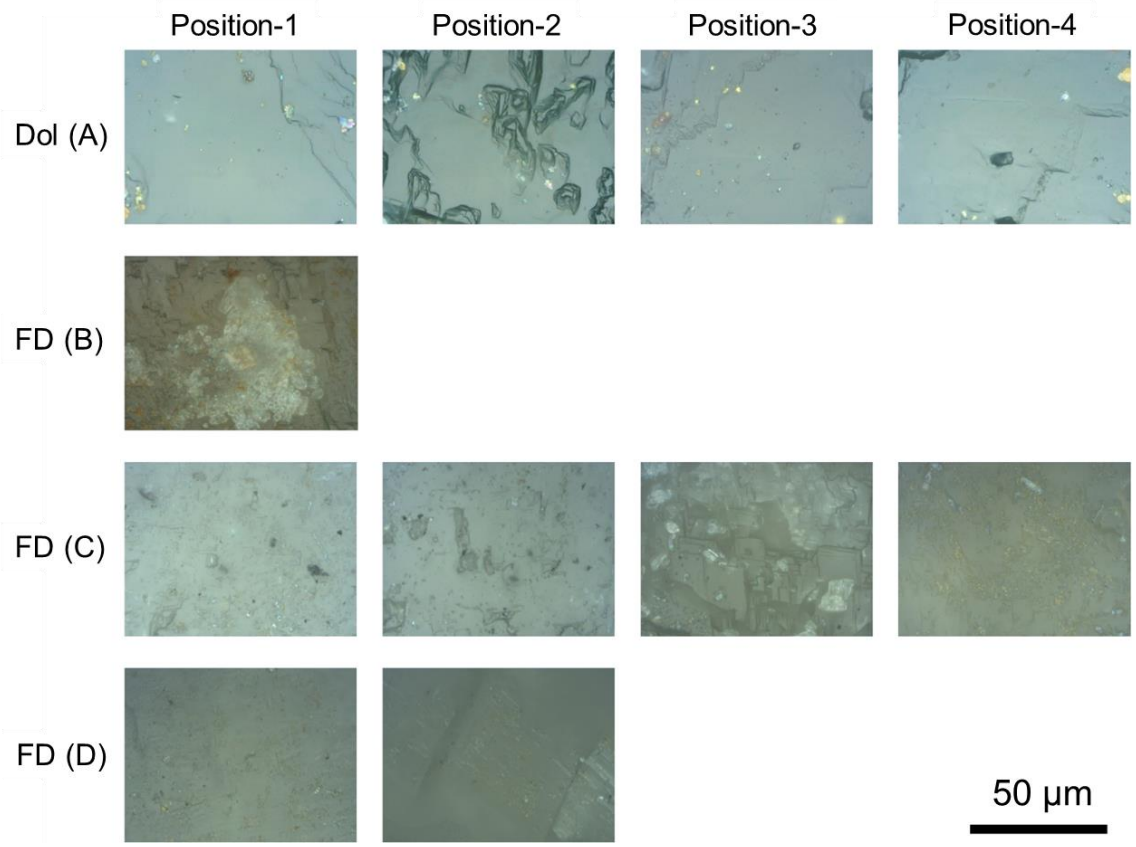

Figure D.4 Magnified optical images of each measurement position obtained by Raman microscope.

Subsequently, we carried out Raman measurements on the identical 11 positions as XRF measurements. Notably, 25 grid points in each of the XRF measurement spots were probed to make up the difference in spatial resolution of the two techniques. The grid points in each XRF measurement spot span approximately 50 μm square within an optical microscopic image shown in Figure D.4. Figure D.5 shows a typical Raman spectrum for each chip. Two characteristic T and L mode peaks are present in each chip, and both are assigned to carbonates. Both bands were clearly observed for all chips and at all positions. However, more precisely, their peak wavenumber was distinct at each position. One consistent trend between the two studies is that as the Fe+Mn is richer (ferroan dolomite), the T or L mode wavenumber becomes lower. Interestingly, it also turned out that Raman

bands of the ferroan dolomites (B-D) were broader than those of dolomite (A). A possible reason for this band broadening is that incorporating Fe or Mn will reduce crystallinity or induce growth defects, and it may lead to greater bandwidths (Reeder & Prosky, 1986).

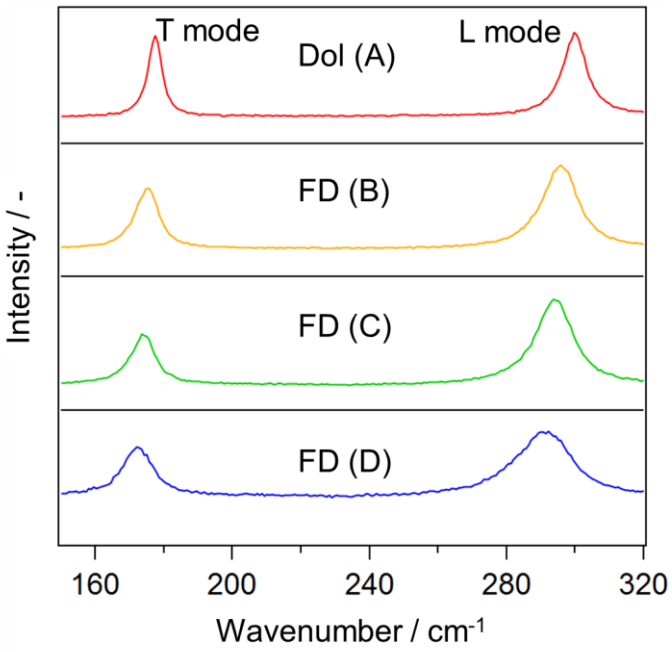

Figure D.5 Typical Raman spectra for each sample. The intensities for each spectrum are normalized at the peak top of L mode. Dol: dolomite, FD: ferroan dolomite.

Again, we biaxially plotted T and L mode wavenumbers. In Figure D.6(a), the datapoints represent averaged peak wavenumbers for the 25 grid points, and the lines represent their standard deviation. As Figure D.6(b) demonstrated, the plots were linearly distributed in the biaxial map. For this reason, standard deviations for T and L modes are depicted as a line. This figure strongly implies the peak wavenumbers for these modes differed position-by-position. As further discussions are described below, peak wavenumbers of L mode with significant variations will be one-to-one corresponding to Fe+Mn content at each measurement position. For details, the values of peak wavenumbers observed at each measurement position are present in Table D.1.

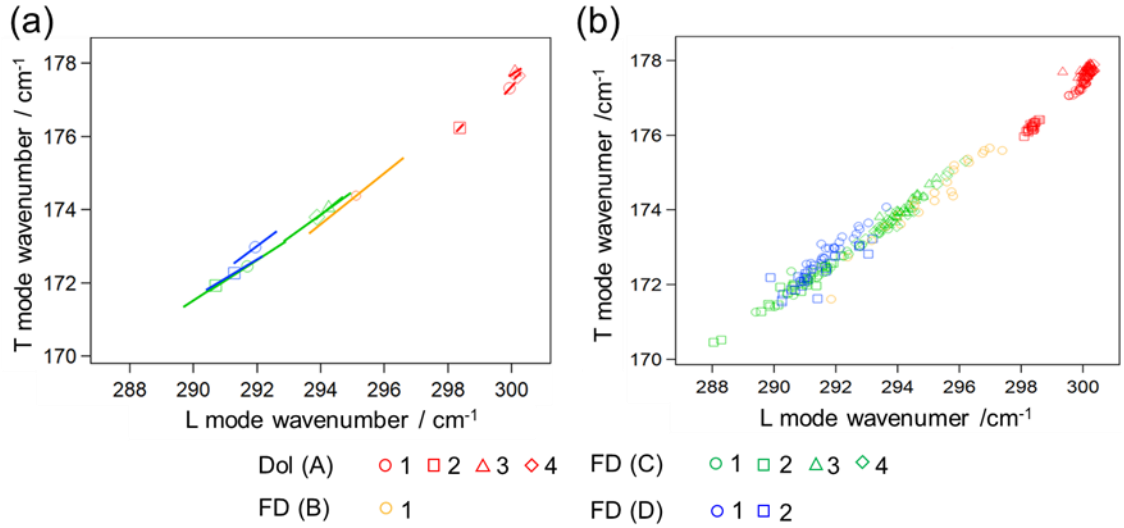

Figure D.6 Biaxial maps of T and L mode wavenumbers with the average and standard deviations of datapoints depicted by lines and markers (a), respectively, all datapoints depected by only markers (b). Dol: dolomite, FD; ferroan dolomite.

Figure D.7 shows the relation between the Fe+Mn contents and the T mode wavenumbers. Here, one can easily see that these peak wavenumbers and the cation contents were correlated in a linear manner. In fact, the coefficients of determination (R^2) indicating linearity were 0.956 for the T mode.

Table D.1 Summary of the cation composition estimated by XRF and Raman wavenumbers. [a]Given in the atomic ratio to the total cation contents.

The chip and the measured position	Cation composition[a]					Raman wavenumber [cm^{-1}]	
	Ca	Mg	Fe	Mn	Fe + Mn	T	L
A1	0.545	0.445	0.007	0.002	0.009	177.3 ± 0.2	299.9 ± 0.2
A2	0.550	0.402	0.040	0.008	0.048	176.2 ± 0.1	298.4 ± 0.1
A3	0.532	0.454	0.008	0.001	0.009	177.8 ± 0.1	300.1 ± 0.2
A4	0.537	0.453	0.008	0.001	0.009	177.7 ± 0.1	300.2 ± 0.1
B1	0.593	0.273	0.018	0.115	0.133	174.4 ± 1.0	295.1 ± 1.5
C1	0.546	0.248	0.133	0.068	0.202	172.5 ± 0.7	291.7 ± 1.2
C2	0.538	0.239	0.149	0.070	0.219	171.9 ± 0.6	290.7 ± 1.0
C3	0.532	0.272	0.067	0.126	0.193	174.0 ± 0.3	294.3 ± 0.4
C4	0.561	0.281	0.074	0.082	0.156	173.8 ± 0.7	293.9 ± 1.1
D1	0.553	0.245	0.132	0.069	0.201	173.0 ± 0.4	291.9 ± 0.7
D2	0.546	0.262	0.133	0.058	0.191	172.3 ± 0.5	291.3 ± 0.9

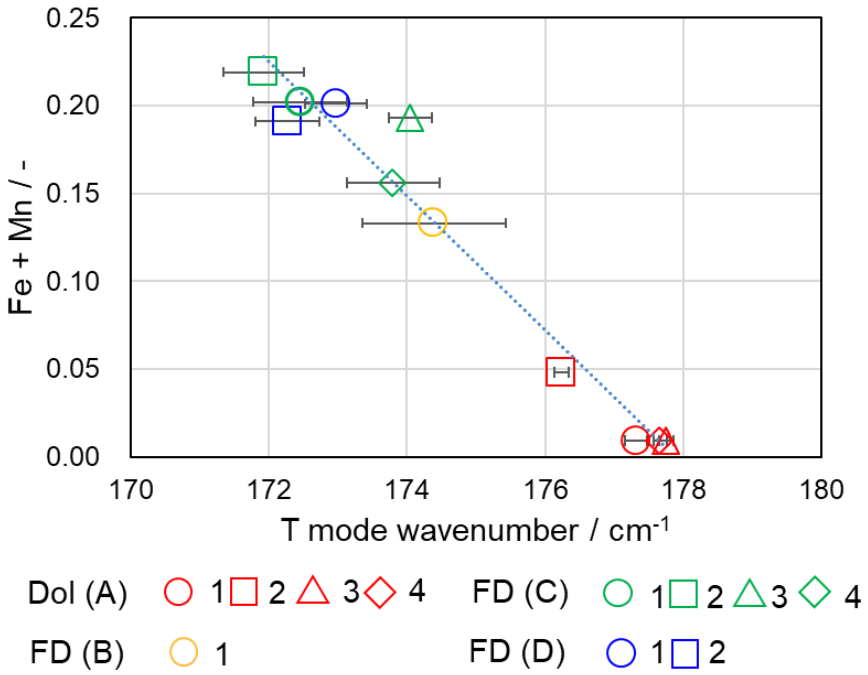

Figure D.7 Fe+Mn content plotted against the Raman wavenubmers of the T mode.
Dol: dolomite, FD: ferroan dolomite.

D.3 Experimental details and supportive information for the sample analysis of Asteroid Ryugu

D.3.1 Elemental abundances of the Ryugu samples

As elemental abundances of the Ryugu samples resemble the ones of other carbonaceous chondrites shown in Figure 5.2, detailed results by different analytical methods are provided in Table D.2.

Table D.2 Elemental abundances of the Ryugu samples (unit: ppm). The table is modified by (Yokoyama et al., 2023). Rigaku: WDXRF, Horiba: LE-M-XRF(EDXRF), TG EMIA: H and O analysis, TD#1: touchdown site 1, TD#2 touchdown site 2.

		CI		CM					Ryugu				
								TD#2				TD#1	
Atomic Number	Element	Lodders21*	2SD	Lodders21*	Rigaku	SD	Horiba	SD	TG EMIA	ICPMS	SD	ICPMS	SD
1	H	18600	3440	11500					9400				
2	He	0.00917											
3	Li	1.51	0.12	1.63						1.34	0.11	1.32	0.14
4	Be	0.022	0.0016	0.032						0.0144	0.0030	0.0210	0.0067

5	B	0.744	0.172	0.46									
6	C	41300	8400	23200	46000	743	53687	6991	46300				
7	N	2500	660	1120									
8	O	453840	20000	424100	395000	2844							
9	F	92	40	52									
10	Ne	0.00018											
11	Na	5100	500	4000	7919	148	8171	262	5900	125	5155	109	
12	Mg	95170	4000	119000	127950	655	102193	850	104222	1153	106866	1250	
13	Al	8370	600	11400	10330	122	8037	95	8959	153	8636	150	
14	Si	107740	7200	132000	130030	696	118545	1028					
15	P	978	120	980	1051	14	1027	22	1586	73	1273	52	
16	S	53600	4400	30000	49860	320	62606	522					
17	Cl	717	270	470	776	21							

18	Ar	0.00133										
19	K	539	48	410	579	22	360	7	604	30	520	21
20	Ca	8840	700	12000	14480	186	12144	124	13743	432	16315	386
21	Sc	5.83	0.4	8.2					6	0	6	0
22	Ti	450	30	610	497	34	425	5	466	6	479	5
23	V	53.6	4	72	64	13	72*	2	57.3	1.9	57.1	2.4
24	Cr	2610	200	3090	3447	70	2259	21	2792	39	2695	48
25	Mn	1896	160	1700	2570	51	2174	19	2490	29	3000	38
26	Fe	185620	13000	211000	187710	1375	180308	1415	202217	2242	194925	2130
27	Co	508	30	560	599	17			587	9	549	8
28	Ni	10950	700	12500	11459	57	10245	83	12229	153	11789	142
29	Cu	130	20	129	111	5	166	5	156	4	133	5
30	Zn	311	20	177	343	6	312	3	352	9	338	10

D.3.2 Terrestrial references

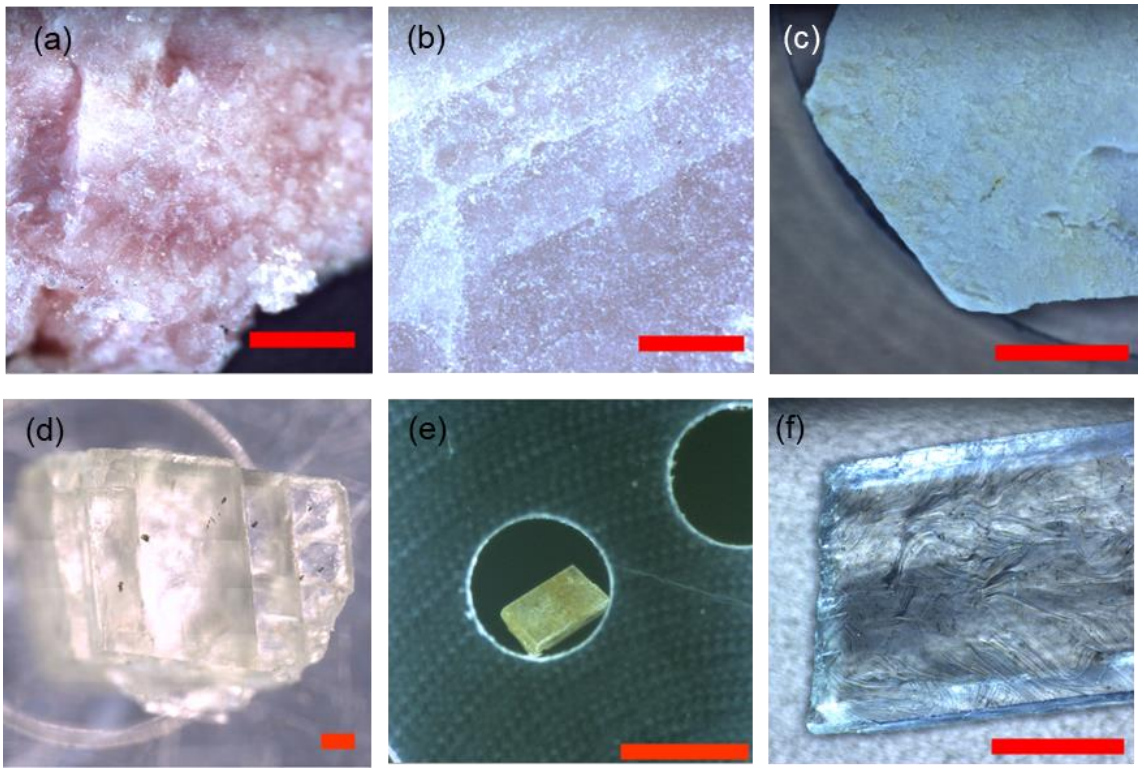

Figure D.8 Optical images of the terrestrial carbonates. (a) kutnohorite (W), (b) kutnohorite (SH), (c) calcite, (d) dolomite (MV), (e) ferroan dolomite (EM), (f) magnesite. Mined locations are available from Table 4.1 and section D.2.1. Scale bars correspond to 1 mm.

D.3.3 Inductively coupled plasma atomic emission spectroscopy for terrestrial carbonates

The dolomite (MV) particle was dissolved in 10 mL of royal water and then filled to 100 mL. The solution was measured to quantify the four cations Mg, Ca, Mn, and Fe after further dilution. The ICP-AES measurements were performed with OPTIMA 8300 (PerkinElmer, Inc). The calibration curves were made by using JCSS reference materials (available from Kanto Chemical Co., Inc. Soka factory). The cation composition was obtained in wt.% by averaging values of three repeated measurements.

D.3.4 Cation composition by micro-XRF

Micro-XRF studied 16 points for the dolomite (MV) particle. The measurement conditions of the X-ray tube voltage, the X-ray tube current, X-ray working distance were 30 kV, 500 μA, 1.0 mm, respectively. The measurement time for each point was 100 s. The mean value of the 16 datapoints for cation contents based on the standard FP method was used to revise the Eqs. (5.2), (5.3).

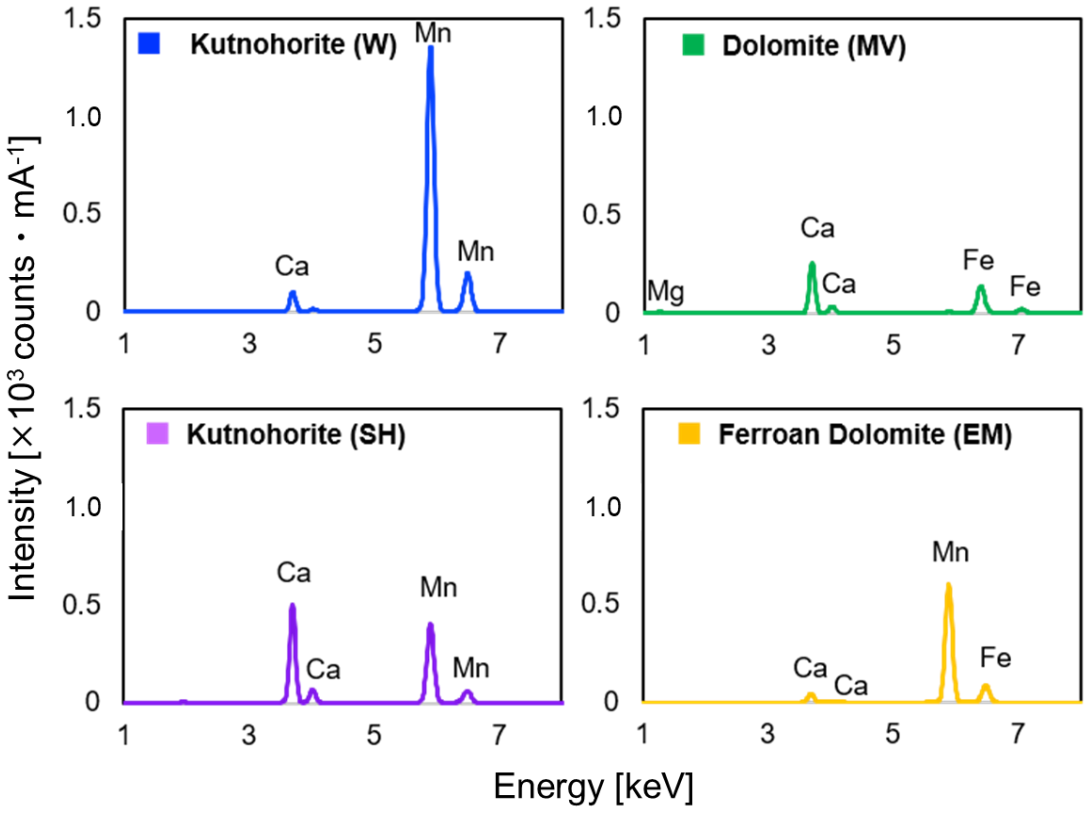

Figure D.9 XRF spectra of terrestrial carbonates.

Table D.3 Cation compositions of terrestrial carbonates. The values for kutnohorite (W) and (SH) are cited from (Urashima et al., 2023) and the one for ferroan dolomite are from (Morita et al., 2023). The values in parentheses are calculated from the quantitative results by ICP-AES.

	mined location	cation composition			
		Ca	Mg	Fe	Mn
kutnohorite (W)	Wissels mine, Northern Cape, South Africa	0.126 ± 0.007	0.038 ± 0.007	0.004 ± 0.001	0.832 ± 0.010
kutnohorite (SH)	Sterling Mine, New Jersey, USA	0.661 ± 0.024	0.032 ± 0.023	0.004 ± 0.000	0.303 ± 0.011
dolomite (MV)	Morro Velho Mine, Minas Gerais, Brazil	0.399 ± 0.002 (0.398)	0.494 ± 0.003 (0.496)	0.102 ± 0.003 (0.101)	0.005 ± 0.000 (0.006)
ferroan dolomite (EM)	Eagle Mine, Colorado, USA	0.593	0.273	0.018	0.133

D.3.5 Derivation of Eq. (5.4) in the main text

According to our previous work (Morita et al., 2023), Ca content (C_{Ca}) is linearly related with the T and L mode wavenumbers ($\widetilde{\nu_{\mathrm{T}}}$ and $\widetilde{\nu_{\mathrm{L}}}$). Note that $\widetilde{\nu_{\mathrm{T}}}$ and $\widetilde{\nu_{\mathrm{L}}}$ are determined in cm^{-1} unit here. Suppose we have 3 standard carbonates, whose C_{Ca}, $\widetilde{\nu_{\mathrm{T}}}$, and $\widetilde{\nu_{\mathrm{L}}}$ are known as $(C_{\mathrm{Ca},1}, \widetilde{\nu_{\mathrm{T},1}}, \widetilde{\nu_{\mathrm{L},1}})$, $(C_{\mathrm{Ca},2}, \widetilde{\nu_{\mathrm{T},2}}, \widetilde{\nu_{\mathrm{L},2}})$, and $(C_{\mathrm{Ca},3}, \widetilde{\nu_{\mathrm{T},3}}, \widetilde{\nu_{\mathrm{L},3}})$ for the standards 1, 2, and 3, respectively. Because C_{Ca} and the wavenumbers $\widetilde{\nu_{\mathrm{T}}}$ and $\widetilde{\nu_{\mathrm{L}}}$ are linearly related, the following equations

$$\widetilde{\nu_{\mathrm{T},1}}x + \widetilde{\nu_{\mathrm{L},1}}y + z = C_{\mathrm{Ca},1}$$

$$\widetilde{\nu_{\mathrm{T},2}}x + \widetilde{\nu_{\mathrm{L},2}}y + z = C_{\mathrm{Ca},2}$$

$$\widetilde{\nu_{\mathrm{T},3}}x + \widetilde{\nu_{\mathrm{L},3}}y + z = C_{\mathrm{Ca},3}$$

are satisfied. The unknown coefficients x, y, and z are thus

$$\begin{pmatrix} x \\ y \\ x \end{pmatrix} = \begin{pmatrix} \widetilde{\nu_{\mathrm{T},1}} & \widetilde{\nu_{\mathrm{L},1}} & 1 \\ \widetilde{\nu_{\mathrm{T},2}} & \widetilde{\nu_{\mathrm{L},2}} & 1 \\ \widetilde{\nu_{\mathrm{T},3}} & \widetilde{\nu_{\mathrm{L},3}} & 1 \end{pmatrix}^{-1} \begin{pmatrix} C_{\mathrm{Ca},1} \\ C_{\mathrm{Ca},2} \\ C_{\mathrm{Ca},3} \end{pmatrix} \quad (\mathrm{D.1}).$$

In the previous and present study, kutnohorite (SH) and kutnohorite (W) were used for the standards 2 and 3. For the standard 1, a geo-standard sample named JDo-1 was used in the previous study. JDo-1 is a dolostone mined at Kuzuu, Tochigi, Japan, and it is a commercially available geo-standard provided by The National Institute of Advanced Industrial Science and Technology (AIST), Japan. In the previous study, we used the JDo-1, because its composition is accurately determined and provided by AIST. However, we later found out that the JDo-1 is a mixture of calcite [$CaCO_3$] and dolomite [$CaMg(CO_3)_2$]. In fact, we sometimes found Raman bands assignable to calcite from JDo-1 powder, as shown in Figure 4.2. Hence, the C_{Ca} of JDo-1 determined as 0.567 is partially derived from calcite, so the cation content of 0.567 cannot be related to $\widetilde{\nu_{\mathrm{T}}}$ and $\widetilde{\nu_{\mathrm{L}}}$ of dolomite in JDo-1. Accordingly, in the present study, we used dolomite (MV) as the standard 1 instead of JDo-1. Dolomite (MV) was chosen because it was relatively homogeneous, as shown in Figure 5.10. We substituted the parameters in Eq. (D.1) with experimentally determined values. We then obtained:

$$\begin{pmatrix} x \\ y \\ x \end{pmatrix} = \begin{pmatrix} 174.103 & 296.731 & 1 \\ 162.444 & 286.094 & 1 \\ 179.662 & 286.386 & 1 \end{pmatrix}^{-1} \begin{pmatrix} 0.494 \\ 0.661 \\ 0.126 \end{pmatrix}$$

$$= \begin{pmatrix} -0.00162371 & -0.0575557 & 0.0591794 \\ 0.0957912 & -0.0309258 & -0.0648654 \\ -27.1415 & 19.1973 & 8.94425 \end{pmatrix} \begin{pmatrix} 0.494 \\ 0.661 \\ 0.126 \end{pmatrix}$$

$$= \begin{pmatrix} -0.03139 \\ 0.01867 \\ 0.419 \end{pmatrix}.$$

Namely,

$$C_{\mathrm{Ca}} = -0.03139\widetilde{v_{\mathrm{T}}} + 0.01867\widetilde{v_{\mathrm{L}}} + 0.419 \qquad (5.4)$$

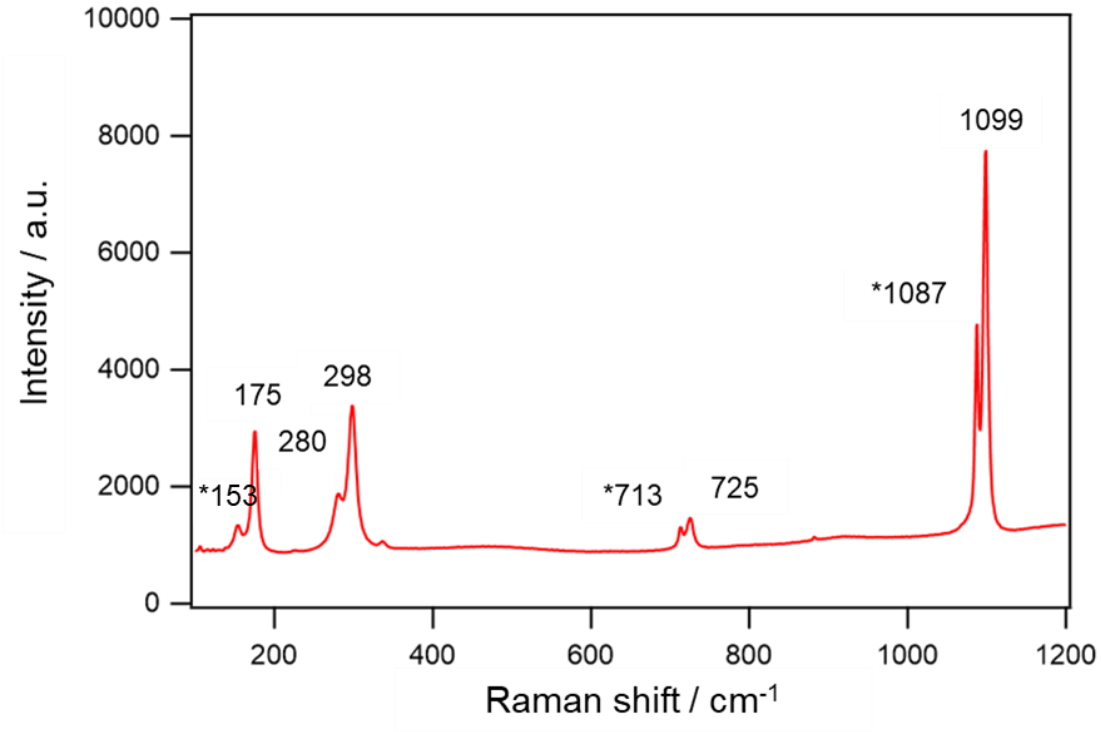

Figure D.10 A Raman spectrum of JDo-1. The peaks with asterisk(*) are assigned to calcite.

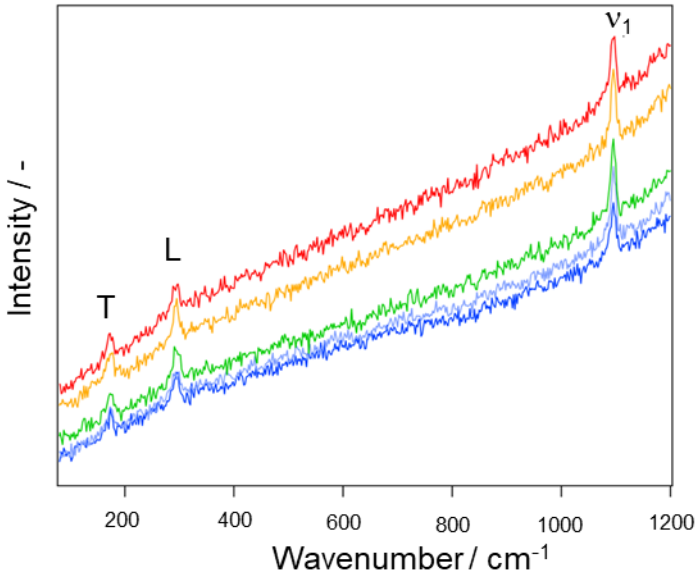

Figure D.11 Raman spectra obtained at different spots in grain B.

D.3.6 An irregularly rich Fe+Mn content

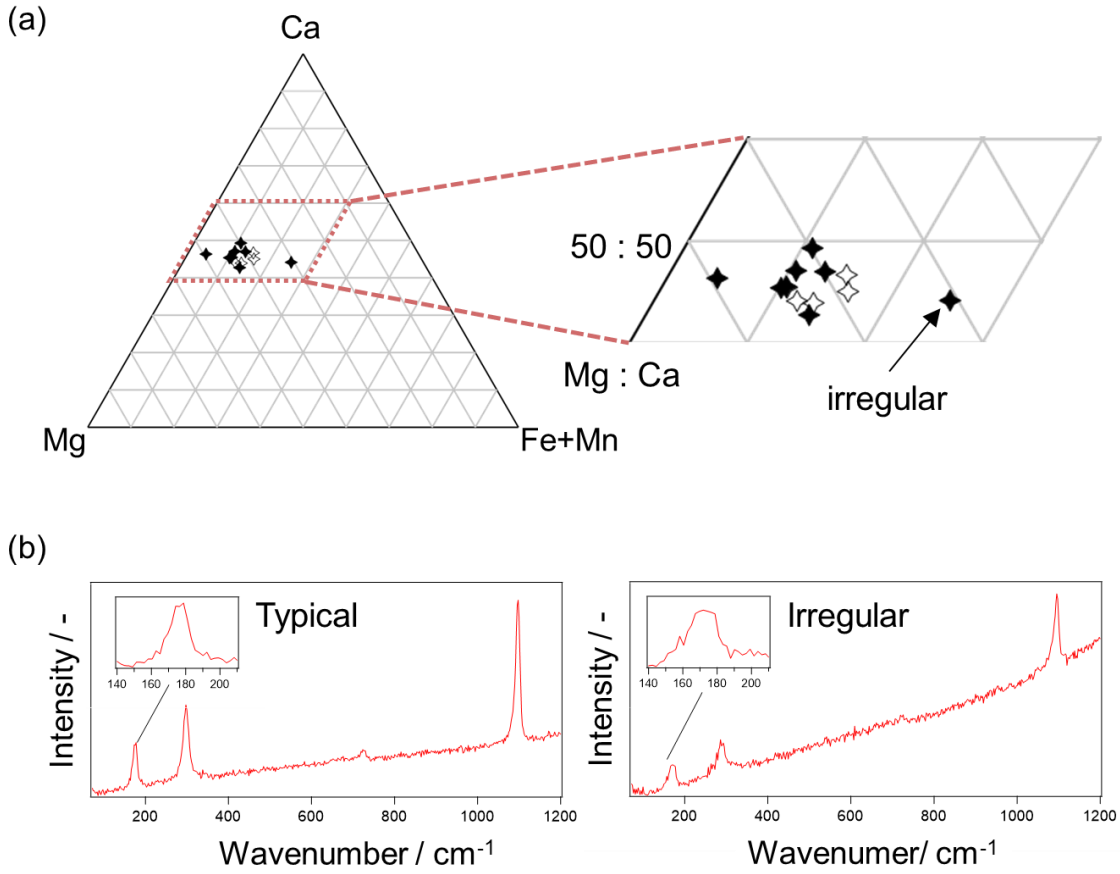

Figure D.12 (a) Cation compositions for Ryugu dolomites and (b) Raman spectra for different grains of Spot A. Raman spectra measured at spots showing typical and irregular compositions for comparison. "Typical" spectrum is for the Spot A(a), whereas "Irregular" is for the Spot A(c) The figure is cited and modified from (Morita et al., 2024).

In Figure D.12(a), we denoted a label "irregular" with around 25% of Fe+Mn. The grain corresponds to the spot A(c), and notably, it turned out that the Raman peaks obtained were rather broader than those typically obtained, as shown in Figure D.12(b). The reason for the band broadening is yet to be understood. However, a plausible explanation is low crystallinity of the dolomite grain at the spot A(c). The difficulty is determining the peak position for these broad bands. Therefore, we cannot conclude whether the irregularly high concentration (~25%) of Fe+Mn was true or only an artifact due to the broadened

Raman band. We must remark that the adequate quality of spectra, *i.e.*, sufficient peak intensity or fair sharpness of a peak without irregular broadening, is imperative for accurate estimation. In this regard, the proposed technique can only sometimes be applied to other data, *e.g.*, Raman mapping data. Occasionally, peak frequencies will be automatically provided even if the spectral quality is not satisfactory. In these cases, its reliability should be confirmed in terms of the signal-to-noise ratio, signal-to-background ratio, and sharpness of the bands. Unfortunately, this analysis cannot discriminate Fe and Mn due to the close similarity within their ionic radii and masses (Urashima et al., 2023; Morita et al., 2023). However, it is crucial to note that quantitative analysis in the present study has been achieved but by the Raman shifts of the signals, not by signal intensity. Using Raman shifts independently from the matrix effects enables us to estimate cation compositions accurately.

D.4 Bibliography

Imai, N., Terashima, S., Itoh, S., & Ando, A. (1996). 1996 COMPILATION OF ANALYTICAL DATA ON NINE GSJ GEOCHEMICAL REFERENCE SAMPLES, "SEDIMENTARY ROCK SERIES". *Geostandards Newsletter*, 20(2), 165–216. https://doi.org/10.1111/j.1751-908X.1996.tb00184.x

Morita, M., Aoyama, T., Nakano, H., & Komatani, S. (2022). Practical Application of Elemental Imaging for Light Elements, Including Oxygen and Fluorine in Industrial Materials by Micro-EDXRF. *Advances in X-ray Chemical Analysis, Japan.*, 53, 139–149.

Morita, M., Urashima, S.-H., Tsuchiya, H., Komatani, S., & Yui, H. (2023). New analytical method for the evaluation of heterogeneity in cation compositions of

dolomites by micro-XRF and Raman spectroscopies. *Analytical Sciences*, 39, 1279-1295. https://doi.org/10.1007/s44211-023-00333-5

Morita, M., Yui, H., Urashima, S.-H., Onose, M., Komatani, S., Nakai, I., Abe, Y., Terada, Y., Homma, H., Motomura, K., Ichida, K., Yokoyama, T., Nagashima, K., Aléon, J., Alexander, C. M. O'D., Amari, S., Amelin, Y., Bajo, K.-I., Bizzarro, M., …Yurimoto, H. (2024). Analysis of Cation Composition in Dolomites on the Intact Particles Sampled from Asteroid Ryugu. *Analytical Chemistry*, 96(1), 170–178. https://doi.org/10.1021/acs.analchem.3c03463

Sherman, J. (1955). The theoretical derivation of fluorescent X-ray intensities from mixtures. *Spectrochimica Acta*, 7, 283–306. https://doi.org/10.1016/0371-1951(55)80041-0

Shiraiwa, T. & Fujino, N. (1966). Theoretical Calculation of Fluorescent X-ray Intensities in Fluorescent X-ray spectrochemical Analysis. *Japanese Journal of Applied Physics*, 5, 886. https://doi.org/10.1002/xrs.1300130203

Urashima, S. -H., Nishioka, T., & Yui, H. (2022). Micro-Raman spectroscopic analysis on natural carbonates: linear relations found via biaxial plotting of peak frequencies for cation substituted species. *Analytical Sciences*., 38, 921–929. https://doi.org/10.1007/s44211-022-00119-1

Reeder, R. J. & Prosky, J. L. (1986). Compositional sector zoning in dolomite. *Journal of Sedimentary Research*, 56(2), 237–247. https://doi.org/10.1306/212F88CD-2B24-11D7-8648000102C1865D

Yokoyama, T., Nagashima, K., Nakai, I., Young, E. D., Abe, Y., Aléon, J., Alexander, C. M. O'D., Amari, S., Amelin, Y., Bajo, K.-I., Bizzarro, M., Bouvier, A., Carlson, R. W., … Yurimoto, H. (2023). Samples returned from the asteroid Ryugu are similar to

Ivuna-type carbonaceous meteorites. *Science*, 379(6634), eabn7850. https://doi.org/10.1126/science.abn7850

Acknowledgements

While this thesis is written in English, I would want to use my native language, Japanese, to express deep gratitude to people who helped me work on the studies and others during my life.

本文は英語で書かれていますが，本研究およびその他の諸事について尽力いただきましたすべての方々に母語で謝意を述べたく，この謝辞のみは日本語にいたします．

始めに，本博士論文の指導教員である由井宏治教授に深謝の意を表します．由井先生とは，はやぶさ 2 プロジェクトのご縁で研究をご一緒いたしました．この度，論文博士の機会をいただき，実験の計画から論文執筆まで細やかなご指導を賜りました．研究に対し真摯でレベルの高い質と量を追求する一流の研究者でありながら，筆者を一人の研究者としても対等な立場で接してくださる由井先生の魅力的なお人柄に惹かれ，研究生活中は精神的にも支えられました．

次に，同教授主宰の研究室の浦島周平講師からも多大なご支援をいただきました．データの見せ方や文章の展開の仕方に至るまで幅広い点でお世話になり，学術的な活動が不慣れで未熟な筆者を厳しく鍛えてくださいました．深く感謝申し上げます．また多忙な学生生活のなか，本博士論文の一部となる貴重なデータをご提供くださいました同研究室の土屋勇人さん，およびその他の皆様にも心よりお礼申し上げます．

学位論文作成，審査におきましては，東京理科大学・工藤昭彦先生，駒場慎一先生，根岸雄一先生，湯浅順平先生に厚く感謝申し上げます． 研究室・大学の卒業生でない筆者の学位（論文博士）取得に，ご厚意でご協力くださり，有益なアドバイスをいただきました．深く感謝申し上げますとともに，このご縁を大切にしたく存じます．

加えて，はやぶさ 2 プロジェクトでは北海道大学・圦本尚義先生や東京大学・橘省吾先生をはじめとする化学分析チーム，東京理科大学名誉教授・中井泉先生をはじめとする XRF チームの方々にも大変お世話になりました．プロジェクトを通して研究をご一緒いたしました多くの研究者ならびに技術者の方々に，特別な謝意を示します．

また，HORIBA の若手技術者として研究をスタートしてから多くの技術者に出会い，支えられました．最初に，室賀裕一氏に御礼を申し上げます．当時，株式会社堀場テクノサービス代表取締役社長であった室賀氏は，特に功績もなかった筆者に「ぜひうちで一緒に働いて，国際的に活躍してほしい．将来に期待します．」と，温かい言葉をかけてくださいまし

た．さらに同社の山田雄大氏，大澤澄人氏（株式会社堀場製作所）には，なかなか思う通りに実験が進まずくじけそうになったときに，親身にご相談にのっていただきました．駒谷慎太郎氏，田中悟氏，中野ひとみ氏，山﨑宏志氏，青山朋樹氏（株式会社堀場製作所）には，本研究にご協力いただきました．上司でもあり社会人博士の先輩でもある駒谷氏は，研究で悩んだり業務と研究の両立に苦労したりする筆者を見守ってくださいました．彼らをはじめとする職場の皆様ならびに HORIBA グループ社員の方々のご支援，応援がなければ，本研究を遂行できませんでした．そのすべての代表として，同社の現代表取締役社長・千原啓生氏に厚く感謝申し上げます．一連の研究に惜しみなくご協力くださった元同僚の小野瀬森彦氏にも感謝の意を表します．

最後に，私生活面で筆者を支えてくださった方々に感謝いたします．多くの不運に見舞われ，特に博士課程（前期）では，満足のいく研究生活を得ることができませんでした．後期課程への進学を諦め失意の中にあった筆者に，「むしろ，入社後すぐに，会社が支援するから博士号を取って来てほしいと言われるほどの人材になる」と激励の言葉をかけてくださった友人たちに，深く感謝申し上げます．リュウグウ試料分析直前に天国へ旅立っていった愛犬・クーに謝意を表し，ご冥福をお祈りいたします．そして，学部生時代から常に献身的に筆者を支え，愛情を表現してくれた夫・森田尭氏に最大の感謝を示します．